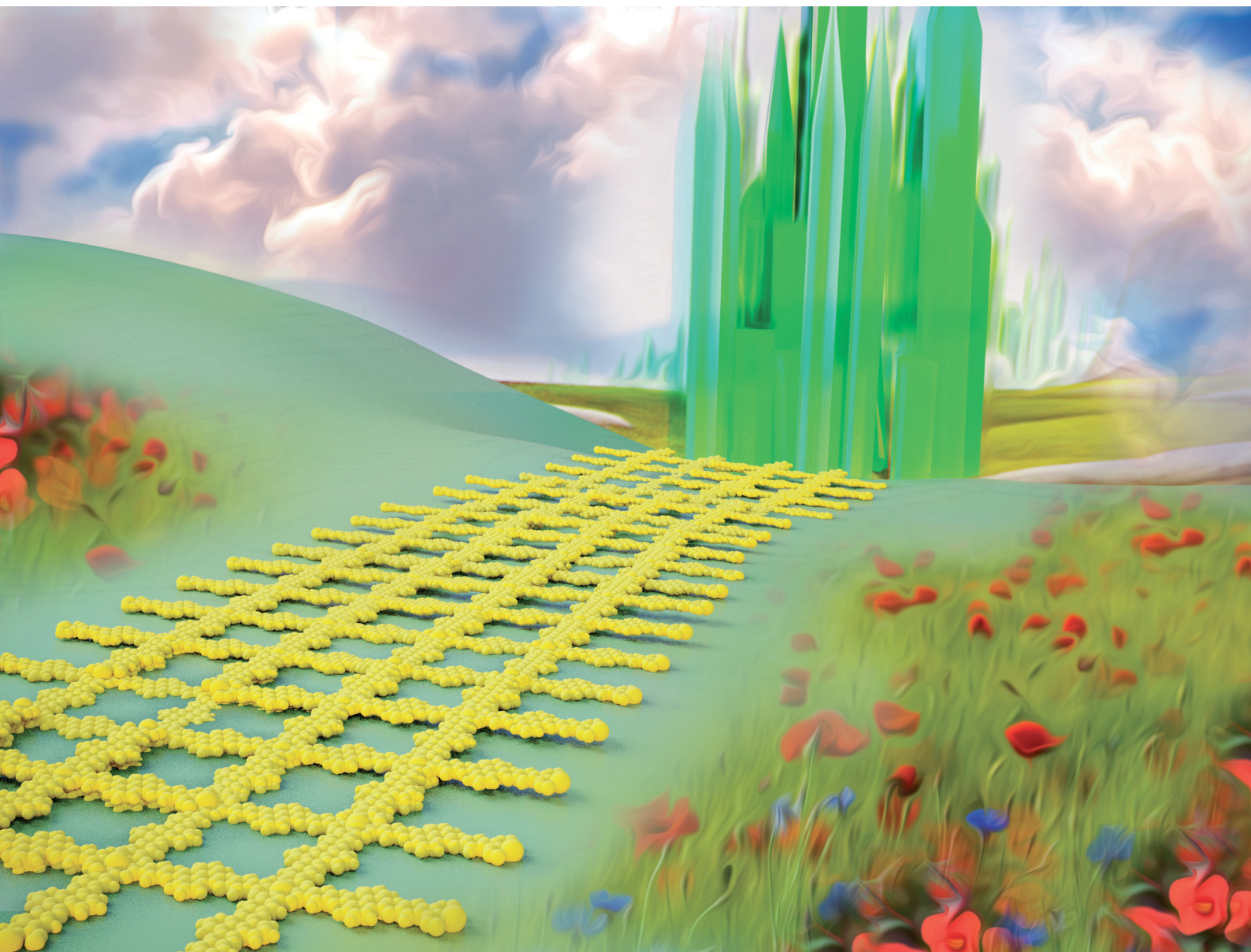


# Chem Soc Rev

Chemical Society Reviews

[rsc.li/chem-soc-rev](https://rsc.li/chem-soc-rev)



ISSN 0306-0012

**REVIEW ARTICLE**

Zheng Meng and Katherine A. Mirica  
Covalent organic frameworks as multifunctional materials  
for chemical detection



Cite this: *Chem. Soc. Rev.*, 2021,  
50, 13498

# Covalent organic frameworks as multifunctional materials for chemical detection

Zheng Meng and Katherine A. Mirica \*

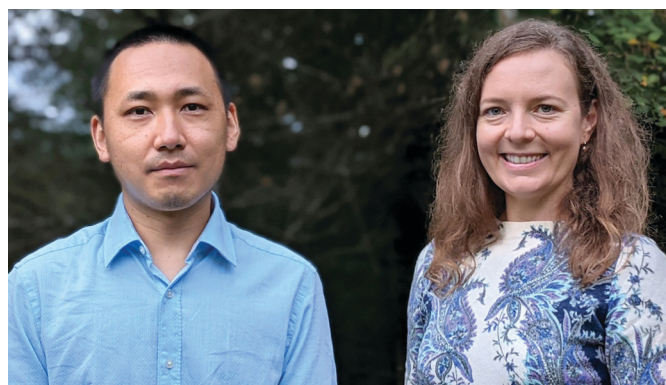
Sensitive and selective detection of chemical and biological analytes is critical in various scientific and technological fields. As an emerging class of multifunctional materials, covalent organic frameworks (COFs) with their unique properties of chemical modularity, large surface area, high stability, low density, and tunable pore sizes and functionalities, which together define their programmable properties, show promise in advancing chemical detection. This review demonstrates the recent progress in chemical detection where COFs constitute an integral component of the achieved function. This review highlights how the unique properties of COFs can be harnessed to develop different types of chemical detection systems based on the principles of chromism, luminescence, electrical transduction, chromatography, spectrometry, and others to achieve highly sensitive and selective detection of various analytes, ranging from gases, volatiles, ions, to biomolecules. The key parameters of detection performance for target analytes are summarized, compared, and analyzed from the perspective of the detection mechanism and structure–property–performance correlations of COFs. Conclusions summarize the current accomplishments and analyze the challenges and limitations that exist for chemical detection under different mechanisms. Perspectives on how future directions of research can advance the COF-based chemical detection through innovation in novel COF design and synthesis, progress in device fabrication, and exploration of novel modes of detection are also discussed.

Received 24th June 2021

DOI: 10.1039/d1cs00600b

[rsc.li/chem-soc-rev](http://rsc.li/chem-soc-rev)

Department of Chemistry, Burke Laboratory, 41 College Street, Dartmouth College, Hanover, NH 03755, USA. E-mail: [Katherine.A.Mirica@dartmouth.edu](mailto:Katherine.A.Mirica@dartmouth.edu)



From left to right: Zheng Meng and Katherine A. Mirica

*Massachusetts Institute of Technology. Dr Mirica began her independent career at Dartmouth College in 2015 and was promoted to Associate Professor in 2021. Her current research program aims to design, synthesize, and gain fundamental insight into structure–function relationships of molecularly precise multifunctional materials with potential applicability for deployment as portable chemical sensors, personal protective equipment, and energy-efficient devices.*

*Zheng Meng obtained his BS from the University of Science and Technology Beijing in 2011. He received his PhD from the Institute of Chemistry, Chinese Academy of Sciences, under the supervision of Prof. Chuan-Feng Chen in 2016. He then moved to Dartmouth College to work as a postdoctoral researcher with Prof. Mirica. His current interests focus on the development of new two-dimensional conductive framework materials and their applications in electronics, sensing, and catalysis. Dr. Katherine Mirica is an Associate Professor of Chemistry at Dartmouth College. She received her BS in Chemistry from Boston College, where she worked in the laboratory of Prof. Lawrence T. Scott. Katherine earned her PhD in Chemistry from Harvard University under the supervision of Prof. George M. Whitesides and completed her postdoctoral training with Prof. Timothy Swager at the*





# 1. Introduction

## 1.1 Development of materials for the advancement of chemical detection

Sensitive and selective detection of chemical and biological analytes is an important branch of analytical science for identifying targets and determining their concentrations. Sensing has been widely applied in various scientific and technological fields ranging from analytical chemistry, life science, materials science, biomedical diagnostics to drug discovery, food security, personal care, environmental monitoring, and the Internet of Things.<sup>1–4</sup> Traditionally, advances in chemical detection have largely benefited from the development of various instrumental methods, such as spectroscopic techniques,<sup>5,6</sup> detectors coupled to chromatography,<sup>7,8</sup> mass spectrometry,<sup>9</sup> electrochemical methods,<sup>10</sup> and others,<sup>11</sup> that have achieved ultrasensitive detection of chemical and biological analytes. Although instrumental analytical approaches continue to evolve and yield capacities on breathtaking scales of complexity and sensitivity, with the increasingly diversified purposes of chemical detection associated with urgent concerns over health and environment, the development of low-cost, convenient, real-time, and highly efficient methods based on portable, wearable, and miniaturized devices for chemical analysis is greatly demanded.<sup>12–17</sup>

Materials chemistry has historically played an indispensable role in analytical chemistry.<sup>18–20</sup> The discovery of new materials has triggered the development of new analytical methods and instrumentation capable of detecting analytes at the single-molecule level.<sup>21</sup> The ability to measure subtle chemical and physical changes in a material has led to the development of materials that can induce sensing responses and transduction of electrical or spectroscopic signals by changing their optical or electronic properties, such as changes in impedance, color, fluorescence, Raman scattering, and surface plasmon resonance.<sup>22</sup> Stimuli-responsive materials have been demonstrated to be useful for detecting a diverse set of analytes, including gases, pH, ATP, microRNA, pesticides, proteins, and bacteria. In addition to serving as analyte-responsive and signal transduction components,<sup>17,22,23</sup> materials can also serve as key components that aid chemical detection, such as an auxiliary selective layer, adsorption module, or scaffold, to couple with classical instrumental techniques for the improvement of the detection performance. For example, materials have been used as conventional sorbents in the solid-phase extraction technique for the pretreatment of the samples or as stationary phases in gas and liquid chromatography or electrochromatography for highly efficient target separations.<sup>24–26</sup>

Progress in chemistry and materials science over the past century has given rise to several distinct classes of materials, such as zeolites,<sup>27</sup> conjugated polymers,<sup>28</sup> graphene,<sup>29</sup> carbon nanotubes,<sup>30</sup> and metal–organic frameworks (MOFs),<sup>31–33</sup> that have significantly propelled the advancement of chemical detection. The unique optical, electronic, and catalytic properties of these materials have been harnessed to create new detection platforms for extensive and successful applications in chemical detection. For example, graphene has been applied

for the fabrication of highly sensitive, wearable, self-powered sensors for the detection of various ions and biological molecules, owing to its extraordinary electrical, chemical, optical, and mechanical properties.<sup>34–36</sup> Conjugated polymers have been developed as reliable materials for the detection of explosives.<sup>37–40</sup> The utilization of carbon nanotubes has enabled their integration into smart and mobile devices toward portable, wireless, non-line-of-sight gas sensing.<sup>41–44</sup> The development of new chemically precise materials that can retain the useful attributes of these established materials while integrating new features, such as porous scaffolds that provide high surface area for analyte uptake and modular accessibility through bottom-up self-assembly, is poised to provide new opportunities for advancing the field of chemical and biological detection.

## 1.2 COFs as emergent multifunctional materials for chemical detection

COFs constitute a class of extended and crystalline porous materials comprising lightweight elements linked together by covalent bonds, and feature precise periodicity in the skeleton with pre-designable pore parameters. Since the landmark synthesis of COFs by Yaghi and coworkers in 2005,<sup>45</sup> the field of COFs has grown tremendously and has attracted intense attention from researchers with diverse expertise.<sup>46–48</sup> As a new generation of porous materials, COFs possess several unique features of chemical modularity, accessibility through bottom-up synthesis from earth-abundant elements, large surface area, high chemical stability with robust chemical linkages, low density, tunable pore sizes, and other modular optical and electronic features. These desirable properties provide new opportunities for a wide range of potential applications in gas adsorption and storage,<sup>49–53</sup> separation,<sup>54–59</sup> catalysis,<sup>60–65</sup> sensing,<sup>66–69</sup> drug delivery,<sup>70</sup> optoelectronics,<sup>71–73</sup> and energy storage.<sup>46,74–79</sup> With the progress in the design and synthesis of COFs and the discovery of their physical and properties, COF-based materials exhibit great potential in analytical chemistry.

COFs have several distinct features and advantages that make them an intriguing group of materials for a new approach to chemical detection. First, COFs have great tunability that allows atomically precise integration of functional organic units into extended and ordered frameworks in a modular and bottom-up manner. The installation of functional and chemically responsive units, such as optically active fragments, Lewis acidic or basic sites, redox-active centers, and catalytic units, can proceed by the judicious selection of building units with control over the linkage of those building blocks to the desired properties of the target material in the context of chemical detection. The incorporation of specific recognition sites into building blocks is an effective way of generating COFs with selective detection capabilities. The functional groups that are introduced into COFs during their synthesis can be further utilized for post-synthetic modification to render different capabilities, such as improved sensitive and selective recognition of analytes.<sup>80</sup> Fine-tuning of the optical and electronic properties for modulating the resulting detection performance can be achieved by a systematic change of the constituent



building blocks among a series of structurally related COFs. This modular control, together with the crystalline nature of COFs, makes them perfect systems for investigating structure–property–performance correlations, assisting in the evolution of the analytical performance.

Second, the intrinsic porosity of COFs with large surface-to-volume ratios is also advantageous in chemical detection. The Brunauer–Emmett–Teller (BET) surface areas of two-dimensional (2D) and three-dimensional (3D) COFs have exceeded 3000<sup>81</sup> and 5000 m<sup>2</sup> g<sup>−1</sup>,<sup>82</sup> respectively. These large surface-to-volume ratios of COFs ensure a tremendous accessible surface area for material–analyte interactions, which are beneficial for realizing high sensitivity, even at extremely low concentrations of the analyte. The porous molecular scaffold with the functional sites can provide a platform for the immobilization of additional recognition components and other supplementary attachments (*e.g.*, metallic nanoparticles, metal oxides, and enzymes), which can further improve the sensing performance. Additionally, the intrinsic porous structure allows efficient uptake of analyte molecules, which is beneficial for the preconcentration of the analyte to enhance the detection sensitivity. Selectivity for the uptake of guest molecules can also be further optimized through the engineering of pore parameters.<sup>55</sup>

Third, certain classes of COFs can be constructed using robust covalent bonds and thereby can show enhanced chemical and thermal stability when compared with their counterparts, MOFs, which are usually connected by relatively weak coordination bonds.<sup>83,84</sup> The reinforced stability of COFs can be obtained by providing hydrogen bonding interactions,<sup>85</sup> weakening the polarity of the amine bond,<sup>86,87</sup> introducing enol–keto tautomerizations,<sup>88</sup> utilizing a Michael addition–elimination/benzoxazole pathway,<sup>89</sup> and constructing polyarylether<sup>90</sup> and pyrazine linkages.<sup>91–93</sup> The state-of-the-art approaches to stabilize COFs have resulted in materials that are highly stable to hydrolysis, a wide range of pH, and reductive and oxidative environments.<sup>79,94,95</sup> These advances can ensure the applicability of COFs for chemical detection in harsh chemical or physical conditions, such as high ionic strength, high acidity, high basicity, or high operating temperatures.

Overall, chemical detection can take full advantage of the crystalline nature, diverse tunable structure, porous and stable skeleton, and a wide range of other properties of COFs to develop detection platforms. Because of these diversified structural features and properties, COFs have been utilized as multifunctional materials for chemical detection. Different types of chemical detection modes using COFs have been established, including chromism, luminescence, electrical transduction (including electrochemical and chemiresistive detection), chromatographic and spectrometric detection, surface-enhanced Raman spectroscopy (SERS), and quartz crystal microbalance (QCM) (Section 2). Among these methods, detection based on chromism, luminescence, electrochemistry, chromatography, and spectrometry has now been well established. Examples based on SERS, QCM, and chemiresistive detection, although still limited at this time, constitute emerging areas with room for future development.

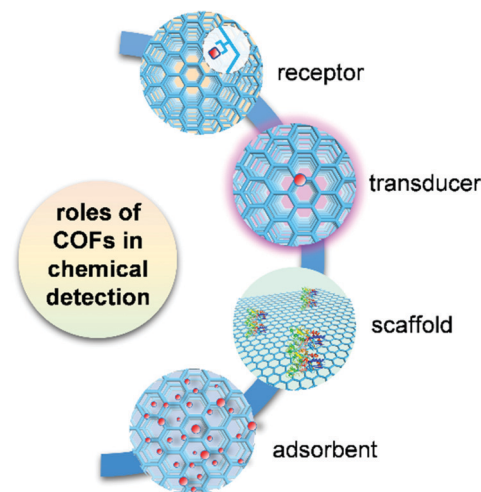


Fig. 1 Multiple roles of COFs in the application of chemical detection.

COFs play multiple roles in analytical detection mechanisms (Fig. 1). In the detection using chromism, luminescence, and electrical transduction, COFs can serve as both receptor and transducer, where they recognize analytes and produce a readable signal attributed to the changes in their photophysical and electronic properties. In some of the electrochemistry-based, SERS, and QCM detection modes, COF-based materials only function as receptors for selective binding of analytes. In chromatographic and spectrometric detection, COFs play an important role as an adsorbent in the selective extraction of an analyte from a complex sample containing trace amounts of the target. COFs also provide porous scaffolds for loading other active materials in building electrochemical detection platforms or serve as an ionization matrix in MS for small molecule detection. By reviewing these detection schemes, we summarize key accomplishments for COF-based chemical detection, and numerous opportunities that exist for both fundamental and applied research in this growing field.

### 1.3 Scope of the review

In this review, we focus on the recent progress in chemical detection that uses COFs as an integral part of the analytical system. We demonstrate in detail the application of COFs in chemical detection based on different mechanisms categorized into four groups: (1) chromism, (2) luminescence, (3) electrical transduction, and (4) chromatographic and spectrometric detection. We also include the discussion of detection mechanisms that are relatively less established, but different from those mentioned above, including SERS, laser desorption/ionization time-of-flight mass spectrometry, and QCM. We provide a brief tutorial on the basic operation principles of each detection mode to establish a clear connection between the detection mechanism and the unique structural characteristics and properties of COFs. In the discussion of each detection mode, the advances in chemical detection using COFs are highlighted chronologically and by dividing analytes into three major groups: gases and volatiles, ions, and biomolecules,





whenever possible. The key parameters of detection performance for target analytes are summarized, compared, and analyzed in the context of the structure–property–performance correlations of COFs. We conclude by summarizing the current accomplishments and analyzing the challenges and limitations that exist for chemical detection under each mechanism. We give perspectives on the future trends that will drive COF-based chemical detection to a new stage through innovation in novel COF design and synthesis, advances in device fabrication, and exploration of novel modes for detection.

With the rapid development in the synthesis and discovery of the properties of COFs, as well as the advances in the fabrication techniques of COFs, their applications in chemical detection have burgeoned into a new research field. Only a few reviews have focused on the summary of the potential of COFs in chemical sensing,<sup>68,69</sup> and the systematic discussion of the progress and challenges of COFs in the broader context of chemical detection and from the perspective of different detection mechanisms is still lacking. One of the important aims in the organization of this review is to help the readers appreciate how the unique and diversified properties of COFs can be harnessed in multiple ways to develop chemical detection systems based on different detection principles within a field that is in a period of rapid growth.

The synthesis of COFs can be achieved through bottom-up connections of organic building units with well-defined geometry by various covalent linkages, such as boronic ester, imines, hydrazones, azines, C=C coupling, and dioxines, yielding extended, crystalline, porous, solid-state materials.<sup>46,47,79,96–100</sup> The applications of COFs often depend on the embedded chemical functionality. Functionality that cannot be introduced into COFs during direct synthesis can be accessed through post-synthetic modification using metal complexation, covalent attachment with existing pendant groups, and chemical conversion of linkages.<sup>80</sup> The synthesis, modification, and fabrication strategies of COFs have already been well documented,<sup>46–48,79,80,96–100</sup> and, therefore, are omitted in this review, though chemical detection methods using COFs build upon on this groundwork. Fundamental understanding of the structure–property relationships of COFs can guide the design of new COFs for different purposes, such as gas capture, catalysis, and energy storage, to name just a few. For the discussions of structure–property relationships in a general sense, the readers are encouraged to refer to existing information on this topic.<sup>46,47,96</sup> Chemical detection using amorphous porous covalent organic polymers<sup>40,101–106</sup> is not discussed in this review due to the amorphous nature and lack of an atomically precise structure of these materials.

MOFs have been historically recognized as a group of structurally related materials of COFs, which share several key features with COFs, including high surface area, permanent porosity, extended crystalline structure, and modular and tunable accessibility. The applications of MOFs in chemical sensing have already been well summarized in multiple reviews.<sup>107–114</sup> These reviews are helpful for the understanding of the unique role of COFs in chemical detection, in contrast to their MOF counterparts. Compared with MOFs, COFs possess

several distinct features that make them unique in the context of chemical detection. Different from the relatively labile coordination linkages in MOFs, several types of strong covalent linkages have been exploited to obtain COFs with extraordinary thermal and chemical stability.<sup>46,96</sup> This feature is essential for chemical detection under harsh conditions. Metal ions incorporated in MOFs usually have nontrivial effects on the optical, electrical, and electrochemical properties of the frameworks resulting from the intrinsic properties of metal ions or complex metal-to-metal and/or metal-to-ligand interactions. Since there are usually no metals embedded in COF structures, the engineering of targeted properties of COFs for chemical detection can be more straightforward, as compared to MOFs.<sup>108,115</sup> The relatively low-density feature of COFs ascribed to their composition of light elements may also be beneficial for the development of wearable and large-area chemical sensing devices. Finally, reliance primarily on earth-abundant elements of C, H, O, and N for COF construction can be beneficial from the perspective of sustainability and cost. While the use COFs as functional materials in chemical detection is still relatively understudied compared with MOFs, Table 1 summarizes the unique features of COFs as an important candidate for chemical detection, in comparison with other relatively established materials, including carbon nanotubes,<sup>41,116</sup> graphene,<sup>34,117</sup> metal oxides,<sup>118,119</sup> conjugated polymers,<sup>120</sup> and MOFs.<sup>107–113</sup>

## 2. COFs for different types of chemical detection

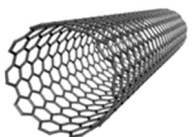
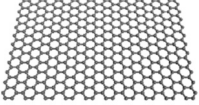
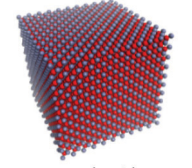
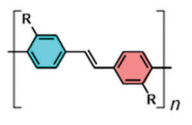
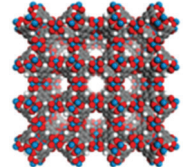
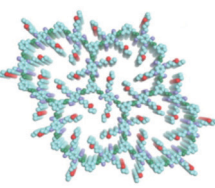
### 2.1 Detection based on chromism

**2.1.1 Basics of chromism-based detection.** Chromism is a process that involves a reversible or irreversible change of the color of a material.<sup>121</sup> Color changes can be caused by multiple reasons, such as photoirradiation, heat, compression, or solvent effects, corresponding to photochromism, thermochromism, piezochromism, and solvatochromism, respectively. Chromism must be characterized by a change in the absorption and/or the emission spectrum of a chromic material, the latter of which is termed luminescence. Chromism-based sensing is one of the most powerful and straightforward means to transduce a signal. This subsection focuses on detection based on chromism arising from the change in the absorption properties of a material. Detection based on the change of fluorescence and/or phosphorescence—two of the important photoluminescence phenomena—is discussed in the following subsection.

COFs have been used in two different modes for chromism-based detection: (1) the chromism phenomenon directly arising from the changes in the absorption properties of COFs; (2) the chromism phenomenon not arising directly from COFs, and instead arising from changes in the color of external dye molecules. The first chromism mode can be further detailed by two situations. First, the material–analyte interaction perturbs the electronic transition responsible for the coloration and results in a change in the absorption of the chromophoric component of the COF.<sup>122</sup> For example, in solvatochromism, one type of



**Table 1** General comparison of representative materials in the context of their use in chemical detection

Example	Advantages	Disadvantages	Detection modes
 carbon nanotube	<ul style="list-style-type: none"> <li>• High surface-to-volume ratio</li> <li>• High aspect ratio</li> <li>• Excellent stability</li> <li>• High density of reactive sites</li> <li>• Good thermal stability</li> <li>• Compatible with device miniaturization</li> </ul>	<ul style="list-style-type: none"> <li>• Requirement of chemical modification to enhance selectivity</li> <li>• Difficulty in establishing reliable electrical contacts</li> <li>• Difficulty in purification</li> <li>• Limited structure and precision control</li> </ul>	<ul style="list-style-type: none"> <li>• Electrochemical</li> <li>• Chemiresistive</li> <li>• Optical detection</li> </ul>
 graphene	<ul style="list-style-type: none"> <li>• Large surface-to-volume ratio</li> <li>• Good optical transparency</li> <li>• Excellent mechanical flexibility</li> <li>• Good functionalization ability</li> <li>• Potential for good processability</li> <li>• Compatible with ultra-thin silicon channel technology</li> </ul>	<ul style="list-style-type: none"> <li>• Zero bandgap</li> <li>• Lack of effective analyte binding sites in its pure form</li> </ul>	<ul style="list-style-type: none"> <li>• Electrochemical</li> <li>• Chemiresistive</li> </ul>
 metal oxide	<ul style="list-style-type: none"> <li>• Strong analyte binding</li> <li>• Good mechanical strength</li> <li>• Good thermal stability</li> <li>• Easy to interface with solid-state devices</li> <li>• Good designability to improve selectivity</li> </ul>	<ul style="list-style-type: none"> <li>• Low surface area</li> <li>• Difficulty with miniaturization</li> <li>• Slow dynamics of analyte transport</li> </ul>	<ul style="list-style-type: none"> <li>• Chemiresistive</li> <li>• Electrochemical</li> </ul>
 conjugated polymer	<ul style="list-style-type: none"> <li>• Feasibility of introducing an analyte receptor</li> <li>• Collective (molecular wire) effect for amplified sensitivity</li> <li>• Wide tunability of conductivity</li> <li>• Good processability</li> </ul>	<ul style="list-style-type: none"> <li>• Possibility of swelling during measurement</li> <li>• Limited solubility in aqueous solution</li> <li>• Dependence on molecular design for high selectivity</li> </ul>	<ul style="list-style-type: none"> <li>• Fluorescence</li> <li>• Conductometric</li> <li>• Potentiometric</li> <li>• Colorimetric</li> </ul>
 MOF	<ul style="list-style-type: none"> <li>• Large surface area and porous structure</li> <li>• Atomically precise structure</li> <li>• Abundant active sites</li> <li>• Tunable pore geometry, surface chemistry, and physical properties</li> </ul>	<ul style="list-style-type: none"> <li>• Stability in harsh environment</li> <li>• Challenge in the fabrication of materials into devices</li> <li>• High cost of large-scale production</li> </ul>	<ul style="list-style-type: none"> <li>• Fluorescence</li> <li>• Electrochemical</li> <li>• Chemiresistive</li> <li>• Electromechanical</li> </ul>
 COF	<ul style="list-style-type: none"> <li>• Large surface area and porous structure</li> <li>• Potential for atomically precise structure</li> <li>• Abundant active sites</li> <li>• Tunable pore geometry, surface chemistry, and physical properties</li> <li>• Generally contains light and earth-abundant elements</li> <li>• Potential to be highly stable</li> </ul>	<ul style="list-style-type: none"> <li>• Limited processability</li> <li>• Challenge in the synthesis of material with high crystallinity and controlled morphology</li> <li>• High cost of large-scale production</li> </ul>	<ul style="list-style-type: none"> <li>• Fluorescence</li> <li>• Colorimetric</li> <li>• Electrochemical</li> <li>• Chemiresistive</li> </ul>

commonly seen chromism induced by solvent, solvent molecules with different polarities can stabilize the excited or ground state of a chromophoric component of the COFs by lowering the LUMO or HOMO level of the chromophore, and respectively causing a red or blue shift. Second, the material-analyte interaction triggers the isomerization of the chromophoric component of COFs, which subsequently changes the electronic transition responsible for the coloration.<sup>123,124</sup> For example, the H-bonding interaction between the analyte and COFs can result in iminol-to-ketoenamine tautomerism of the COF fragment, causing a change in the absorption spectrum.<sup>124</sup> In most COF structures, the extended conjugated skeleton or

aromatic units can serve as chromophores that show characteristic and intensive absorption covering ultraviolet to visible, or even extending to the near-infrared range.<sup>125</sup> The interactions between analyte molecules and COFs, including hydrogen bonding<sup>123,124,126,127</sup> and protonation,<sup>128,129</sup> can initiate an absorption change of these chromophores through either of the two situations described above, which has been utilized for the detection of volatile molecules, including humidity,<sup>123,126,127</sup> organic solvent molecules,<sup>126</sup> and acids.<sup>128,129</sup>

In the second mode, absorption-based detection using COFs is realized by the chromism of external dye molecules. Here, instead of exhibiting chromism, COFs serve as enzyme mimics





to catalyze/mediate redox reactions of dye molecules, leading to a color change of the dyes. When analytes function as oxidants or reductants, the concentration of analytes is proportional to the change of the intensity of the absorption spectrum of the dye.<sup>130,131</sup> When an analyte forms a COF-analyte conjugate or complex that has improved catalytic ability for the redox reaction, the concentration of the analyte can be related to the adsorption change of the dye under a given amount of time.<sup>132–135</sup> The ability of some COFs to mediate coloration reactions of external dyes has been mainly utilized for the detection of some metal ions<sup>132–135</sup> and several biomolecules.<sup>130,131,133</sup>

### 2.1.2 Detection of volatiles, ions, and biomolecules

**Volatiles.** A suitably designed COF treated as a periodic combination of molecular dyes can provide the advantages of insolubility and chemical and photochemical stability over small molecule dyes for detecting target molecules in a stream of gas or liquid.<sup>85</sup> Auras and coworkers developed the first solvatochromic Py-TT COF composed of pyrene (Py) and thieno-[3,2-*b*]thiophene (TT) units, which showed strong color shifts when exposed to water or solvent vapors (Fig. 2a).<sup>126</sup> Exposing the Py-TT COF film to a humidified N<sub>2</sub> stream produced a color change from orange to dark red. Transmission ultraviolet-visible (UV-vis) spectra recorded at different relative pressures of H<sub>2</sub>O revealed the appearance of an absorption band in the 520–640 nm region and a simultaneous

decrease in the 440–500 nm and 280–380 nm spectral regions (Fig. 2b). The COF film exhibited the highest sensitivity towards humidity changes between relative pressures of H<sub>2</sub>O in the range of 0.64–0.79 (Fig. 2c). The response to changes in the surrounding atmosphere occurred within milliseconds, outperforming commercially available humidity sensors by more than an order of magnitude (Fig. 2d). In addition to this rapid response, the COF film displayed excellent reversibility and stability over at least 4000 switching cycles of humidity and solvent vapor. The Py-TT COF showed positive solvatochromism, in which the absorption was red-shifted with increasing polarity (Fig. 2e); in this case, the increasing polarity of the surrounding medium provided preferential stabilization of the excited state over the ground state, thus lowering the energy required for photoexcitation. Experimental data and time-dependent density-functional theory (TD-DFT) calculations further suggested that the solvatochromism possessed a pronounced charge-transfer character, which involved a reduction of the electron density on the pyrene moieties and a gain in electron density of the thienothiophene bridges (Fig. 2f). The absence of structural or chemical changes of the COF during the solvatochromism may explain the rapid response to humidity. The observation that electronic transitions in this material can be manipulated reversibly and that intramolecular charge transfer can be facilitated *via* the inclusion of chemically inert guest

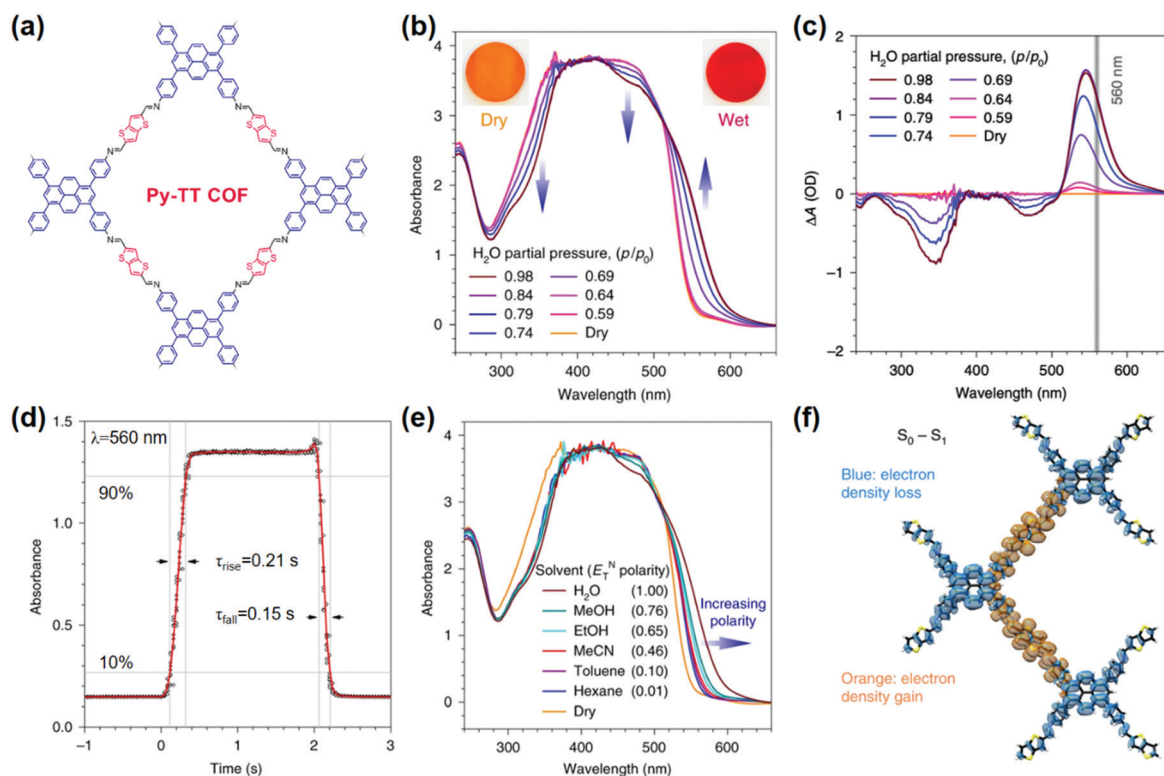


**Fig. 2** (a) Chemical structure of Py-TT COF. (b) UV-vis absorption spectra of the Py-TT COF film recorded at different relative pressures of H<sub>2</sub>O in N<sub>2</sub>. (c) Plots of the humidity-induced absorbance changes at different H<sub>2</sub>O relative pressures. The grey line indicates the wavelength used for the response time measurements. (d) The solvatochromic response of the Py-TT COF film towards step changes between dry and H<sub>2</sub>O-saturated N<sub>2</sub> streams. (e) UV-vis spectra of the same COF film in saturated atmospheres of various solvents. (f) TD-DFT calculated electron density difference upon one-electron excitation from the ground state (S<sub>0</sub>) to the first singlet excited state (S<sub>1</sub>).<sup>126</sup> Adapted with permission from ref. 126. Copyright 2018, Springer Nature.



molecules has the potential to impact the development of stimuli-responsive organic electronics.<sup>126</sup>

Liu and coworkers reported another crystalline DHNDA-TAPP COF made of 2,6-dihydroxynaphthalene-1,5-dicarbaldehyde (DHNDA) and 2,4,6-tris(4-aminophenyl)-pyridine (TAPP) for humidity detection. Nanofibers of COF DHNDA-TAPP were epitaxially grown on the aramid microfiber surface to form a functional nanocomposite,<sup>123</sup> which showed a reversible humidity response with increasing RH from 20% to 100% through a color change from light yellow to dark red detectable by an unaided eye.<sup>123</sup> The authors suggested that the water-promoted transformation of isomers between enol form and keto form was likely responsible for the color change.<sup>136</sup> The change in the absorption spectrum induced by water-triggered enol to keto tautomerism was further supported and systematically studied by Loh and coworkers.<sup>127</sup> This study found that the enol to keto tautomerism significantly affected the charge transfer between the electron donor and acceptor components within the COFs containing triphenylamine or salicylidene-aniline building units, and thus altered the optical bandgap.

Based on the iminol-to-ketoenamine tautomerism, in 2020 Dichtel and coworkers demonstrated the chromism of the TAPB-PDA-OH COF made of 1,3,5-tris(4-aminophenyl)benzene (TAPB) and terephthalaldehyde (PDA) for colorimetric humidity detection (Fig. 3a).<sup>124</sup> The TAPB-PDA-OH COF changed color upon solvation, with a preferred response to high-polarity solvents, such as ethylene glycol and water (Fig. 3b). The absorption of the device made of TAPB-PDA-OH film dramatically increased with the increase of humidity from 0% to 100% (Fig. 3c). The COF film showed a fast and highly reversible response and recovery when switching between humid and dry air within 1 s and 9 s, respectively (Fig. 3d). The response was indistinguishable from that of the first sensing even after more than a month of ambient storage, indicating good stability of this sensor (Fig. 3e). Spectroscopic studies indicated that the chromism responsible for the humidity sensing was attributed to the water-mediated tautomerism in the TAPB-PDA-OH COF. DFT calculations on a related model compound indicated that the diiminol tautomer was strongly preferred in the gas phase; however, in the presence of two water molecules, the diiminol and *cis*-iminol/ketoenamine were nearly isoenergetic, indicating that both tautomers can be present in significant quantities in a humid environment (Fig. 3f). The authors concluded that the stronger acceptor nature of the central ring of the iminol/ketoenamine tautomer compared to the diiminol resulted in a charge-transfer-type excited state, leading to a new absorption feature.<sup>124</sup>

The above examples indicated that water-promoted isomerization of COFs is the main mechanism used for the detection of humidity. In contrast, the detection of acids has been mainly based on Lewis acid–base reactions between the protons and the nitrogen-containing sites (*e.g.*, C=N) present in COFs. For example, Kulkarni *et al.* reported a COF PBHP-TAPT made of (1,4-phenylene)bis(3-hydroxyprop-2-en-1-one) (PBHP) and 1,3,5-tris(4-aminophenyl)triazine (TAPT), in which triazine was the Lewis-basic moiety for HCl detection.<sup>128</sup> The COF powder

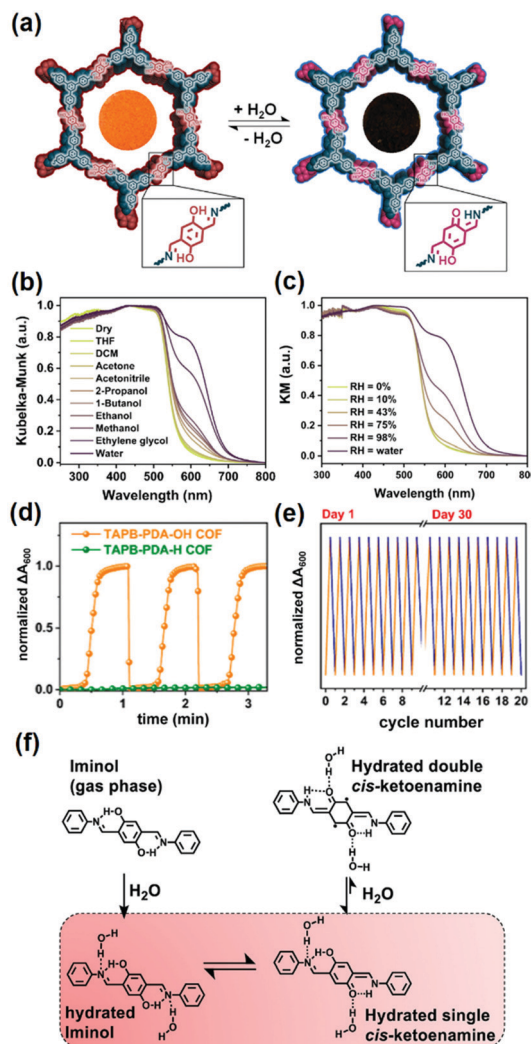


Fig. 3 (a) COF TAPB-PDA-OH as a colorimetric humidity sensing device based on the iminol-to-ketoenamine tautomerism. Diffuse reflectance spectroscopy plots for the TAPB-PDA-OH COF powder exposed to (b) different solvents and (c) different levels of humidity. (d) Humidity sensing using TAPB-PDA-OH COF films using the change in absorbance at 600 nm. (e) Humidity sensing using TAPB-PDA-OH films over multiple cycles. (f) Chemical structures of the different tautomers of the small-molecule model compound.<sup>124</sup> Reprinted with permission from ref. 124. Copyright 2020, American Chemical Society.

changed its color from orange to red (525 nm to 630 nm) within seconds after exposure to HCl vapor. This color change was fully reversible when the HCl-treated sample was exposed to NH<sub>3</sub> vapor under the same conditions. The PBHP-TAPT COF showed high sensitivity to low concentrations of HCl gas down to 20–50 ppm, with a high threshold at around 3000 ppm. The rapid color change offered an advantage over other optical sensors for corrosive gases, where good reversibility and real-time response can be challenging to achieve.<sup>137</sup>

In addition to the triazine group mentioned in the above example,<sup>137</sup> Auras and coworkers demonstrated the utilization of imine linkages as the functional moiety in COFs for acid vapor sensing.<sup>129</sup> A series of dual-pore perylene (Per)-based





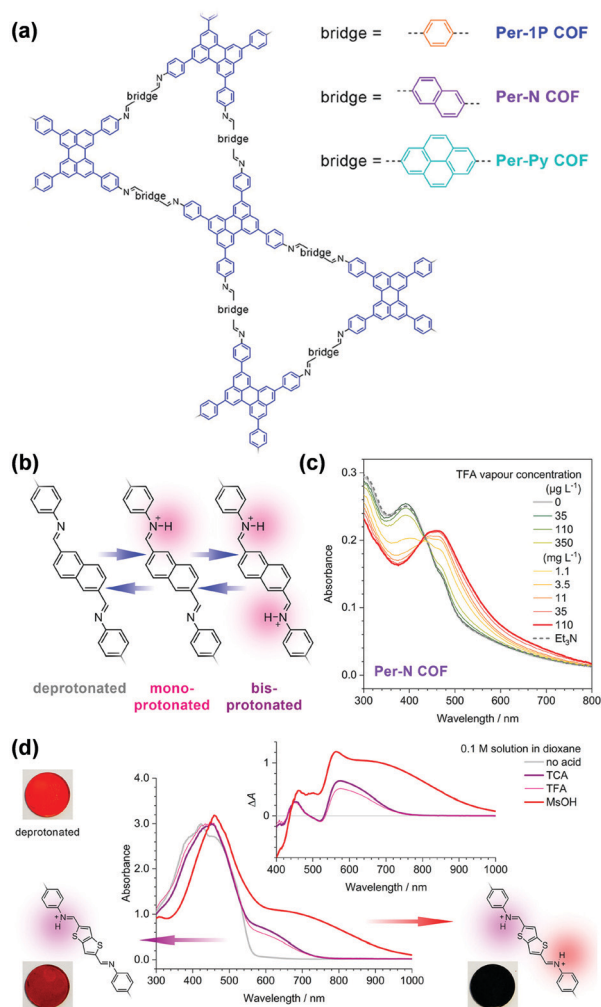


**Fig. 4** (a) Structure of the perylene-based COFs. (b) The imine-linked bridges of the Per-N COF can be protonated stepwise. (c) Absorption spectra of the Per-N COF film upon protonation in TFA vapor of increasing concentration (green to red lines). (d) Protonation of the Py-TT COF with different acid solutions. TFA and TCA solutions produced selectively the monoprotonated bridge unit with a characteristic absorption band between 550 and 750 nm. The considerably stronger MsOH generated a much stronger absorption band which extends further into the IR. TCA, trichloroacetic acid; TFA, trifluoroacetic acid; MsOH, methanesulfonic acid.<sup>129</sup> Reprinted with permission from ref. 129. Copyright 2019, American Chemical Society.

COFs, including Per-1P, Per-N, and Per-Py, featuring phenylene-N=CH-bridge-HC=N-phenylene units were investigated (Fig. 4a). The protonation of the nitrogen lone pair of imines typically leads to their decomposition if small amounts of water are present;<sup>138</sup> however, the authors found that the close-packed structures of 2D COFs provided sufficient stabilization against hydrolysis and enable fully reversible protonation and deprotonation (Fig. 4b).<sup>129</sup> The lowest-energy optical transitions of these imine-linked COFs were characterized by charge-transfer with the first singlet excited state localized on the imines. Since the protonated imines are stronger electron acceptors than their free-base counterparts, the energies of these transitions are lowered, leading to red-shifted absorption

and emission spectra. Trifluoroacetic acid at a low concentration of  $35 \mu\text{g L}^{-1}$  led to a measurable change in the absorption spectrum with protonation-induced absorption and bleach bands extending from 440 to 800 nm, which became more prominent with increasing acid vapor concentration, without any saturation effects (Fig. 4c). Protonation of the phenylene-N=CH-bridge-HC=N-phenylene units proceeded in a two-step process, with the second protonation requiring significantly stronger acids, since the monoprotonation reduced the basicity of the neighboring imine. The mono- and the bisprotonated species featured distinct absorption features in the red and near-infrared spectral regions (Fig. 4d). These features may enable these COFs to act as colorimetric sensors for simultaneous determination of the acid strength and concentration in nonaqueous solutions, where traditional pH electrodes are not applicable.

The above examples demonstrate chromism-based detection of volatile analytes based on the intrinsic optical properties of COFs themselves. For chromism-based detection of ions and biomolecules, researchers have successfully harnessed the catalytic properties of COFs. The most exploited system so far has been based on mimicking peroxidases using COFs, in which COFs catalyze a redox reaction and change the adsorption of external dyes. The characteristic features of COFs, such as high porosity, high surface area, abundant active sites, and good thermal and chemical stability coupled with  $\pi$ -electronic structures that can provide excellent electron transfer properties, are highly desirable for designing mimics of peroxidases to mediate the redox reaction for chromism-based detection.

**Ions.** Xiong and coworkers developed a  $\text{Cu}^{2+}$  detection method by mimicking the peroxidase with a covalent triazine framework (CTF).<sup>132</sup> The peroxidase-like catalytic activity of the CTF can be modulated by  $\text{Cu}^{2+}$  ions. In the presence of  $\text{Cu}^{2+}$  ions, the catalytic activity of the CTF was significantly enhanced, which enabled oxidation of the colorless substrate 3,3',5,5'-tetramethylbenzidine (TMB) to bright blue oxidized TMB (oxTMB) in the presence of  $\text{H}_2\text{O}_2$ . Based on this colorimetric method, a good linear relationship between the adsorption of oxTMB and concentration of  $\text{Cu}^{2+}$  ions at  $1.0$  to  $80.0 \mu\text{g L}^{-1}$  could be obtained with a limit of detection (LOD) at  $0.05 \mu\text{g L}^{-1}$ . The high specificity of  $\text{Cu}^{2+}$ -N chelation resulted in good selectivity for  $\text{Cu}^{2+}$  over other competing ions, such as  $\text{Na}^+$ ,  $\text{K}^+$ ,  $\text{Ba}^{2+}$ ,  $\text{Zn}^{2+}$ ,  $\text{Al}^{3+}$ , and  $\text{Ce}^{3+}$ . This strategy was further applied for the detection of  $\text{Cu}^{2+}$  ions in real food samples with recoveries of 96–105%, constituting a promising approach for the rapid, selective, sensitive, and low-cost detection of  $\text{Cu}^{2+}$  ions.<sup>132</sup> Considering the slow analyte diffusion resulting from the 3D nature of the bulk CTF, this method was optimized by using an iron-modified two-dimensional covalent triazine framework (2D Fe-CTF) for  $\text{F}^-$  detection.<sup>133</sup> The 2D Fe-CTF sheets with favorable dispersibility, large surface areas, and abundant accessible active sites allowed fast analyte diffusion, enabling detection of  $\text{F}^-$  ions in the 50–700 nM range with a low limit of detection (signal/noise = 3) of 5 nM and good selectivity over various interfering ions, including  $\text{Cl}^-$ ,  $\text{Br}^-$ ,  $\text{SO}_4^{2-}$ ,  $\text{NO}_3^-$ ,  $\text{HCO}_3^-$ ,  $\text{HCOO}^-$ ,  $\text{CO}_3^{2-}$ ,  $\text{PO}_4^{3-}$ , and  $\text{CH}_3\text{COO}^-$ .<sup>133</sup>



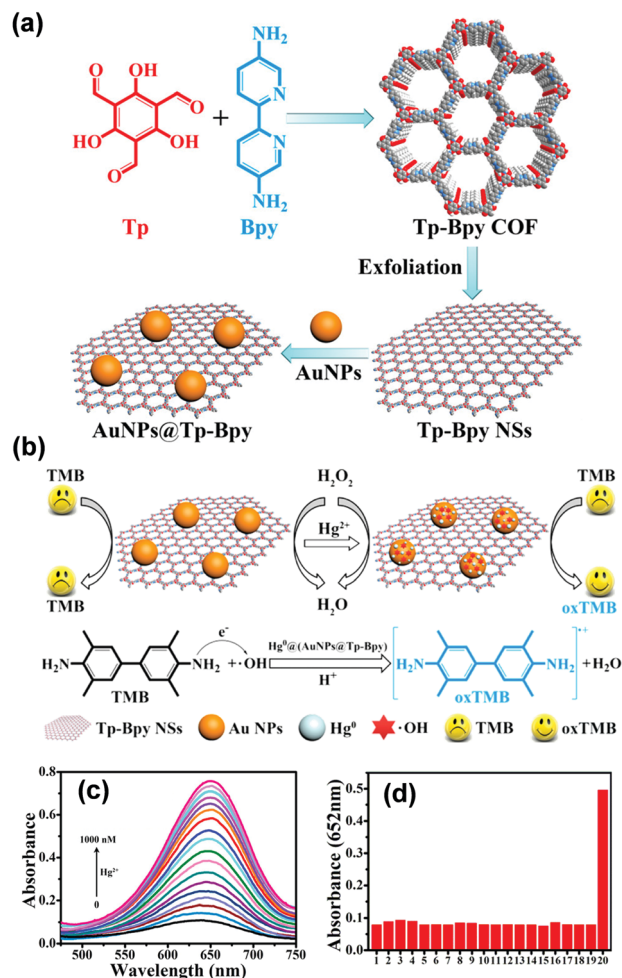


**Fig. 5** (a) The synthesis of the Au NPs@Tp-Bpy nanocomposite. (b) Mechanism of colorimetric detection of mercury ions using Au NPs@Tp-Bpy. (c) UV-vis spectra after addition of Hg<sup>2+</sup> to 1000 nM. (d) Catalytic activity of the Au NPs@Tp-Bpy nanocomposite stimulated by different metal ions (1, blank; 2, Cr<sup>3+</sup>; 3, Fe<sup>3+</sup>; 4, Cu<sup>2+</sup>; 5, Zn<sup>2+</sup>; 6, Mg<sup>2+</sup>; 7, Co<sup>2+</sup>; 8, Ag<sup>+</sup>; 9, Pb<sup>2+</sup>; 10, Ni<sup>2+</sup>; 11, Na<sup>+</sup>; 12, K<sup>+</sup>; 13, Ca<sup>2+</sup>; 14, Al<sup>3+</sup>; 15, Ba<sup>2+</sup>; 16, Mn<sup>2+</sup>; 17, NH<sub>4</sub><sup>+</sup>; 18, Cd<sup>2+</sup>; 19, Fe<sup>2+</sup>; and 20, Hg<sup>2+</sup>).<sup>134</sup> Adapted with permission from ref. 134. Copyright 2019, American Chemical Society.

Recently, Qiu and coworkers used bipyridine-containing COF (Tp-Bpy) nanosheets (NSs) for highly sensitive mercury sensing.<sup>134</sup> The COF synthesized from 2,4,6-triformylphloroglucinol (Tp) and 5,5'-diamino-2,2'-bipyridine (Bpy) had regular pore structures and abundant nitrogen-containing functional groups, which served as active sites for the *in situ* generation of gold nanoparticles (Au NPs) to create a functionalized composite (Fig. 5a). The presence of Hg<sup>2+</sup> significantly improved the catalytic activity of the Au NPs@Tp-Bpy nanocomposite in the oxidation of colorless TMB to bright blue oxTMB, accompanied by a significant colorimetric response (Fig. 5b). At the same time, the anchoring of Au NPs onto Tp-Bpy NSs through coordination bonds can enhance the dispersibility and stability of the Au NPs, which otherwise can easily aggregate, leading to an unexpected decrease of their catalytic activity. This synergistic effect of the increased mimetic activity of the Au amalgam

and the higher access probability of Hg<sup>2+</sup> provided by Tp-Bpy nanosheets rendered the Au NPs@Tp-Bpy nanocomposite with a high sensitivity for the detection of Hg<sup>2+</sup> with an ultralow detection limit of 0.33 nM (Fig. 5c). Other metal ions, including Cr<sup>3+</sup>, Fe<sup>3+</sup>, Cu<sup>2+</sup>, Zn<sup>2+</sup>, and Mg<sup>2+</sup>, had minimal effects on Hg<sup>2+</sup> detection (Fig. 5d).<sup>134</sup> The strategy based on the color change of TMB catalyzed by Au NPs@COF was also utilized by Yan and coworkers for mercury detection by using a novel COF employing tris-(4-formyl-phenyl)triazine and 4,4'-azodianiline as the monomers for the determination of the mercury content in water.<sup>135</sup>

**Biomolecules.** Hou and coworkers found that the triazine-based COF CTF-1 possessed both intrinsic peroxidase-like activity and oxidase-like activity because it was capable of catalyzing the oxidation of chromogenic substrates, such as TMB, with or without H<sub>2</sub>O<sub>2</sub> with high efficiency. The peroxidase-like activity of CTF-1 may be derived from the formation of hydroxyl radicals (<sup>•</sup>OH), while the oxidase-like activity of CTF-1 mostly stemmed from the generation of O<sub>2</sub><sup>•−</sup> and <sup>1</sup>O<sub>2</sub> derived from the dissolved O<sub>2</sub>. Utilizing this design, the authors developed a colorimetric detection platform composed of TMB and CTF-1 for the detection of biothiols.<sup>130</sup> The absorbance at 652 nm decreased linearly with the increasing concentration of biothiols. This platform was used to detect three biothiols, including glutathione (GSH), cysteine (Cys), and homocysteine (Hcy), with a limit of detection at 0.6 μM.<sup>130</sup> Compared with other sensing systems with similar dynamic ranges and LODs,<sup>139</sup> the method demonstrated simplicity, low cost, and did not require extra light sources and additional chemicals, especially H<sub>2</sub>O<sub>2</sub>, making it a promising enzyme-mimetic alternative for biosensing. Analogous strategies harnessing the catalytic performance of COFs as enzymatic mimics to mediate the coloration of chromogenic substrates have also been developed for the detection of sarcosine and ochratoxin A at sub-μM concentrations<sup>133</sup> and the detection of glucose with LOD at 1.0 μM.<sup>131</sup>

Chromism-based detection has been used to realize the analysis of volatiles, ions, and biomolecules (Table 2). Taking advantage of the solid-state nature, porous skeleton, chemically stable structure, pre-designable active sites, and tunable optical properties of COFs, this detection approach can generally provide the advantages of signal visibility, fast response, good sensitivity, and suitability for on-site detection.<sup>140</sup> Although in a few cases COFs can be used directly in colorimetric detection and their response can be qualitatively visualized by the unaided eyes, the accurate determination of the analyte concentration relies on the monitoring of the absorption spectrum of the chromic materials. Because of their polymeric nature, COFs cannot be directly dissolved in solvents for the absorption spectrum measurement; instead, suspensions of COFs have to be employed. For detection where COFs serve as catalysts to mediate the color change of external dyes, monitoring of the absorption spectrum can be routine and straightforward. However, for the detection based on chromism of COFs, the aggregation state needs to be controlled to ensure the reproducibility and long-term stability of COF suspensions, because





Table 2 Summary of examples relying on chromism-based detection using COFs

Analyte	COF	Detection architecture	LOD	Detection range	Other detection parameters	Ref.
H <sub>2</sub> O	DHND-APP	DHND-APP/aramid microfiber	N/A	20–100% RH	Reversible and repeatable	123
H <sub>2</sub> O	TAPB-PDA-OH	TAPB-PDA-OH film	N/A	10–100% RH	In gas phase, reversible, response time 9 s, recovery time 1 s	124
H <sub>2</sub> O	Py-TT	Py-TT film	N/A	0.59–0.98 ( <i>p/p</i> <sub>0</sub> )	In gas phase, reversible, response time 0.21 s, recovery time 0.15 s	126
HCl	PBHP-TAPT	PBHP-TAPT powder	< 20 ppm	20–3000 ppm	In gas phase, response time < 2 s	128
HCl	Per-N	Per-N film	35 µg L <sup>-1</sup>	35–110 µg L <sup>-1</sup>	In THF solution, reversible when treated with Et <sub>3</sub> N	129
HCl	COF-ETBA-DAB	COF-ETBA-DAB suspension	N/A	0.13–91 mM	In 1,4-dioxane suspension, reversible	141
Cu <sup>2+</sup>	CTF	CTF/TMB/H <sub>2</sub> O <sub>2</sub>	0.08 µg L <sup>-1</sup>	1.0–80 µg L <sup>-1</sup>	In water, pH = 4.0, selectivity over Na <sup>+</sup> , K <sup>+</sup> , Ba <sup>2+</sup> , Zn <sup>2+</sup> , Al <sup>3+</sup> , Ce <sup>3+</sup> , Co <sup>2+</sup> , Ni <sup>2+</sup> , Fe <sup>3+</sup> , Mn <sup>2+</sup> , and Cr <sup>3+</sup> ; vegetable and water sample	132
Hg <sup>2+</sup>	Tp-Bpy	Au NPs@Tp-Bpy/TMB/H <sub>2</sub> O <sub>2</sub>	0.33 nM	0–1000 nM	200 mM H <sub>2</sub> O <sub>2</sub> , pH = 4.0; selectivity over Cr <sup>3+</sup> , Fe <sup>3+</sup> , Cu <sup>2+</sup> , Zn <sup>2+</sup> , Mg <sup>2+</sup> , Co <sup>2+</sup> , Ag <sup>+</sup> , Pb <sup>2+</sup> , Ni <sup>2+</sup> , Na <sup>+</sup> , K <sup>+</sup> , Ca <sup>2+</sup> , Al <sup>3+</sup> , Ba <sup>2+</sup> , Mn <sup>2+</sup> , NH <sub>4</sub> <sup>+</sup> , Cd <sup>2+</sup> , and Fe <sup>2+</sup>	134
Hg <sup>2+</sup>	PTAzo	PTAzo/TMB/H <sub>2</sub> O <sub>2</sub>	0.75 nM	5–300 nM	In acetic acid, pH = 4.0; selectivity over Ca <sup>2+</sup> , Mn <sup>2+</sup> , Cr <sup>3+</sup> , Pb <sup>2+</sup> , Ba <sup>2+</sup> , K <sup>+</sup> , Na <sup>+</sup> , Fe <sup>3+</sup> , Mg <sup>2+</sup> and Cu <sup>2+</sup>	135
F <sup>-</sup>	Fe-CTF	Fe-CTF/TMB/H <sub>2</sub> O <sub>2</sub>	5 nM	50–700 nM	Selectivity over Cl <sup>-</sup> , Br <sup>-</sup> , SO <sub>4</sub> <sup>2-</sup> , NO <sub>3</sub> <sup>-</sup> , HCO <sub>3</sub> <sup>-</sup> , HCOO <sup>-</sup> , CO <sub>3</sub> <sup>2-</sup> , PO <sub>4</sub> <sup>3-</sup> , and CH <sub>3</sub> COO <sup>-</sup>	133
GSH	CTF-1	CTF-1/TMB/H <sub>2</sub> O <sub>2</sub>	0.65 µM	1–100 µM	In 0.1 M NaAc buffer, pH = 4.0	130
Cys	CTF-1	CTF-1/TMB/H <sub>2</sub> O <sub>2</sub>	0.62 µM	1–100 µM	In 0.1 M NaAc buffer, pH = 4.0	130
Hcy	CTF-1	CTF-1/TMB/H <sub>2</sub> O <sub>2</sub>	0.68 µM	1–140 µM	In 0.1 M NaAc buffer, pH = 4.0	130
Glucose	Fe-COF	Fe-COF + TMB + H <sub>2</sub> O <sub>2</sub>	1.1 µM	30–500 µM	In 0.2 M NaAc buffer, pH = 5, selectivity over sucrose, maltose, and lactose	131
Sarcosine	Fe-CTF	Fe-CTF/TMB/H <sub>2</sub> O <sub>2</sub>	0.56 µM	10–100 µM	In 0.2 M PBS buffer, pH = 8.0	133
Ochratoxin A	Fe-CTF	Fe-CTF/TMB/H <sub>2</sub> O <sub>2</sub>	N/A	0.2–0.8 µM	In 50 mM NaAc buffer, pH = 4.0	133
H <sub>2</sub> O <sub>2</sub>	Cu <sup>2+</sup> -CTF	Cu <sup>2+</sup> -CTF/TMB/H <sub>2</sub> O <sub>2</sub>	N/A	2.5–140 µM	In 0.1 M NaAc buffer, pH 4.0	142

both the intensity and the range of the absorption can be a function of the packing states of chromophores in COFs, especially for COFs that have a layered structure.

## 2.2 Detection based on luminescence

### 2.2.1 Basics of luminescence-based detection using COFs

*General principles of luminescence-based detection.* Luminescence is the emission of light upon absorption of energy from various sources, such as chemical energy, electromagnetic radiation, ionizing radiation, heat, pressure, and others.

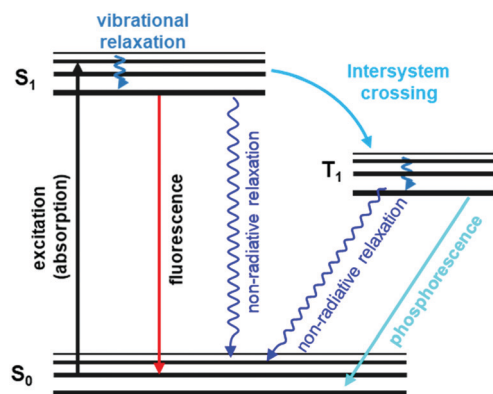


Fig. 6 A typical Jablonski diagram displaying schematically electronic states involved in luminescence phenomena.<sup>146</sup> Adapted with permission from ref. 146. Copyright 2020, Royal Society of Chemistry.

Fluorescence and phosphorescence are two important types of luminescence resulting from the absorption of photons.<sup>143</sup> Fluorescence is a spin-allowed radiative transition from the lowest singlet excited state *S*<sub>1</sub> of the fluorophore to its singlet ground state *S*<sub>0</sub>. Phosphorescence refers to the spin-forbidden radiative transition from the triplet state *T*<sub>1</sub> to ground state *S*<sub>0</sub> (Fig. 6).<sup>115,144</sup> So, fluorescence occurs immediately upon excitation with a short decay time (*t* < 10 ns). Phosphorescence, in contrast, emits continuously for a certain period after the excitation is switched off (*t* > 0.1 s).<sup>145</sup>

There are several parameters of fluorescence emission that can be used to characterize a fluorescent material. First, fluorescence intensity (*I*) can be measured at the given wavelength of excitation and emission (usually, band maxima), whose dependence on emission wavelength gives the fluorescence emission spectrum. Second, emission anisotropy is a function of the fluorescence intensities obtained at two different polarizations, vertical and horizontal. Third, emission can also be characterized by fluorescence lifetime (*τ*), which is the measurement of the time a fluorophore spends in the excited state before returning to the ground state by emitting a photon.

Changes in fluorescence emission properties, such as quenching and enhancement of the intensity, shifts of the fluorescence spectrum, and changes in fluorescence lifetime because of interactions of analytes with fluorophores, can be used to realize sensitive and cost-effective chemical detection.<sup>147–150</sup> Based on different photophysical processes, general fluorescence



detection mechanisms mainly include (1) various charge transfer (CT) processes, including photo-induced electron transfer (PET), intramolecular charge transfer (ICT), metal–ligand charge transfer (MLCT), and twisted intramolecular charge transfer (TICT), (2) energy transfer (ET) processes, including electronic energy transfer (EET) and fluorescence resonance energy transfer (FRET), (3) formation of an exciplex, (4) aggregation-induced emission, and (5) excited-state intramolecular proton transfer (ESIPT).<sup>151</sup>

CT is the most widely applied mechanism employed in fluorescence-based detection.<sup>152</sup> By interacting with analytes, fluorescence of a fluorophore can be quenched due to the PET process. The inhibition of the PET process can recover the fluorescence. For a fluorescent material based on intramolecular charge transfer, enhancement or suppression of the ICT process will lead to a red or blue shift in its emission spectrum. A ratiometric signal can be obtained, which can eliminate ambiguities by self-calibration of two emission bands and allow quantitative determination.<sup>153</sup> MLCT is the charge transfer taking place between a ligand and a transition metal cation and is commonly observed in processes involving transition metal binding.<sup>154</sup> TICT occurs upon photoexcitation in molecules that usually consist of a donor and acceptor linked by a single bond.<sup>155</sup> Following intramolecular twisting, the TICT state returns to the ground state either through a red-shifted emission or by nonradiative relaxation. Since intramolecular rotation is very sensitive to polarity and/or steric hindrance, TICT can be used for the detection of solvents, (micro)viscosity, and chemical species.

The mechanism of ET involves a donor fluorophore, which may transfer its excitation energy to a nearby acceptor chromophore in a non-radiative fashion through long-range dipole–dipole interactions.<sup>156</sup> Based on the distance of interaction between the energy states of donor and acceptor, ET can be classified as electronic energy transfer or fluorescence resonance energy transfer. EET requires a distance between donor and acceptor within 10 Å, while FRET requires a certain degree of spectral overlap between the emission spectrum of the donor and the absorption spectrum of the acceptor. The distance between the donor and acceptor should be from 10 to 100 Å for efficient FRET to occur.<sup>151</sup> For this reason, fluorescence detection based on the ET process is distance-dependent.

In addition to CT and ET processes, the formation of an exciplex is another important mechanism for fluorescence detection. An exciplex is a short-lived heterodimeric molecule formed by the interaction of a fluorophore in the excited state with an analyte molecule. The emission spectrum of an exciplex is red-shifted compared with that of the sole fluorophore, and a dual emission from the monomeric fluorophore and exciplex is often observed simultaneously.<sup>157</sup> Exciplex formation or deformation upon interaction with a guest species allows the detection by simply monitoring the exciplex band.<sup>158</sup>

The AIE phenomenon utilizes the restriction of intramolecular rotation in aggregates to enhance the fluorescence emission.<sup>71,159,160</sup> Unhindered intramolecular rotation in molecules in the free state can lead to nonradiative decay of the

corresponding excited states, making fluorophores nonemissive. Upon aggregation in a suitable environment, intramolecular rotation is restricted, and the emission is thus greatly enhanced. The AIE effect can be tuned by the analyte molecule through electrostatic interaction, coordination interaction, hydrophobic interaction, steric hindrance, or the influence of polarity and viscosity to result in the characteristic change of the fluorescence emission.<sup>151,161,162</sup>

In ESIPT systems, photoexcited molecules relax their energy through tautomerization by the transfer of protons.<sup>163,164</sup> ESIPT is generally a fast process with reported values ranging from fractions of picoseconds to tens of picoseconds. It is easy to recognize in steady-state spectra because the absorbance is generally similar to that of the parent fluorophore but the fluorescence is significantly different. Since ESIPT is much faster than the emission process (radiative decay), the fluorescence observed for ESIPT chromophores is often from the tautomer triggered by the proton dislocation. The accompanied geometry relaxation can result in a large Stokes shift where spectral overlap between absorption and emission is minimized.<sup>165</sup> The ESIPT process can be perturbed by many intermolecular interactions, such as removal of the proton involved in the ESIPT process, and thus can be used for detecting analytes.<sup>151</sup>

*Molecular design of fluorescent COFs.* The molecular design of fluorescent COFs has harnessed the fundamental principles of molecular engineering of other fluorescent materials, including the introduction of well-established fluorescent chromophores, the tuning of the fluorescence properties with modification groups, and the elimination of aggregation-induced fluorescence quenching. The utilization of aromatic and conjugated molecular entities with high probabilities for  $S_0 \rightarrow S_1$  transition and  $\pi^* \rightarrow \pi$  relaxation can give rise to optical emission or photoluminescence when subject to excitation.<sup>71,166–168</sup> Consequently, fluorescent COFs contain large  $\pi$ -conjugated building elements—phenyl, triazine, pyrene, triphenylene, and triphenylbenzene—many of which are well known fluorescent chromophores.<sup>68,169,170</sup> We will see quite a few examples in the following discussions in Sections 2.2.2–2.2.4, where fluorescent COFs used for detection are built upon by directly incorporating fluorescent chromophores. The emission property of these chromophores in COFs can be further modulated to different degrees based on the nature of the linkages. The boronate ester linkages have been popular for the construction of COFs for their reversible feature; however, this type of linkages typically doesn't allow for efficient  $\pi$ -delocalization with the constituent building blocks.<sup>47,125</sup> Thus, for many of the COFs created using boronate ester linkages, the fluorescence properties of the COF mainly originate from the building units. For COFs linked by conjugated linkages, such as imine, triazine, phenazine, or olefins, their optical properties including the fluorescence emissions, can be significantly different from that of the constituent building blocks. The position of the emission peak, luminescence quantum yield, and fluorescence intensity of chromophores in COFs can be modulated by the electronic effects from other components.





The utilization of fluorescent chromophores is a straightforward approach for attaining fluorescence property; this approach also offers unique properties in COFs that are desirable for optoelectronic and photovoltaic device applications.<sup>125</sup> However, the presence of large conjugated fragments can lead to the packing of periodic columnar  $\pi$ -arrays in COFs, which can trigger the thermal decay of photoexcited states and result in reduced or nonemissive characteristics.<sup>71,159,160</sup> This aggregation-caused quenching (ACQ) mechanism is ubiquitous for COFs and is, perhaps, the reason why highly luminescent COFs are rarely achieved even though various luminescent  $\pi$ -units have been employed for the synthesis of COFs.<sup>171–173</sup> To overcome the ACQ effect, two effective strategies have been employed. The first strategy relies on the spatial separation and spacing of the  $\pi$ -conjugated fluorescent chromophores. This concept had previously been utilized for the development of highly fluorescent conjugated polymers through the introduction of structurally rigid and bulky units into chains of polymers to minimize polymer aggregation and self-quenching.<sup>120,174</sup> As for the design of fluorescent COFs with this strategy, both the incorporation of bulky groups<sup>175,176</sup> and the construction of a 3D topology<sup>177</sup> have been demonstrated, in which the fluorescent chromophores are spatially separated to avoid aggregation. In the second strategy, the concept of aggregation-induced emission (AIE)<sup>178,179</sup> is utilized to obtain highly luminescent COFs, which is in sharp contrast with the first strategy where the aggregation is designed to be minimized. This strategy is implemented by introducing AIE active chromophores, which usually have freely rotating groups that enable the energy of the excited state to be released in the form of thermal decay by molecular rotations rather than in the form of fluorescence emission. When these AIE chromophores aggregate, restrictions of molecular rotations restore the release of energy during electron transition in the way of fluorescence emission. In the construction of COFs using the AIE concept, the intralayer covalent bonding and interlayer noncovalent  $\pi$ -interactions can work synergistically to reduce the rotation-induced thermal decay of the photoexcited state to afford high fluorescence emission.<sup>173</sup>

In short, the direct incorporation of well-established fluorescent chromophores is a straightforward way to construct fluorescent COFs. The fluorescence emissions will be mainly determined by the choice of the chromophores, but will also be affected by the type of linkage. However, the aggregation-induced quenching mechanism can make this method ineffective in getting highly emissive COFs. Subsequently, spatial separation of the  $\pi$ -conjugated fluorescent chromophores to avoid aggregation and the use of the AIE concept have become new strategies for achieving highly emissive properties. Taken together, these strategies also illustrate that the fluorescence properties of COFs are dominated by the choice of organic building units. In comparison, in MOFs, luminescence can arise from a few comparable contributors, including direct excitation of organic ligands (particularly from the highly conjugated ligands), metal-centered emission, and charge transfer (such as ligand-to-metal charge transfer and metal-to-ligand

charge transfer).<sup>115</sup> Therefore, the mechanism of luminescence of COFs has the potential to be more straightforward and relatively easy to engineer and exploit compared to MOFs.

#### *Advantages of COFs for fluorescence-based chemical detection.*

Fluorescence-based chemical detection can rely on the analyte–COF interaction that triggers changes in emission property, including wavelength and intensity of emission, or the rise of a new emission band, through multiple feasible mechanisms.<sup>180–182</sup> Fluorescence detection of most of the volatiles, gases, and ions discussed in the following subsections is based on CT between COFs and analytes which usually results in quenching of the luminescence of COFs. These analytes usually possess appropriate receptor energy levels, for example, the LUMO of electron-deficient nitroaromatics<sup>183</sup> and unoccupied d-orbitals of transition metal ions.<sup>176</sup> The quenching can thus be ascribed to nonradiative charge transfer from COF donors to analyte receptors. When the emission band of COFs overlaps with the absorption band of receptor analytes to some degree, the interaction of an excited state fluorophore in COFs with analytes results in radiationless deactivation of the fluorophore to the ground state through the ET process.<sup>184</sup> Interactions between the fluorophore of COFs and the analyte species, such as hydrogen bonding<sup>160,185–187</sup> and coordination bonding, can also reduce  $\pi$ -electron delocalization or structural coplanarity, which may also quench the fluorescence of the system. Moreover, the solvent polarity and the local environment also have profound effects on the emission spectral properties through the aggregation-caused quenching or aggregation-induced emission enhancement effect.<sup>178</sup>

In addition to the feasibility of changing the fluorescence properties *via* the diverse mechanisms mentioned above, three features make COFs excellent candidates for fluorescence-based detection. First, COFs have large surface-to-volume ratios, which can provide abundant active sites for effective material–analyte interaction to enhance sensitivity. Their intrinsic nanoporous structure is beneficial for the preconcentration of analytes to strengthen the sensing response. Second, the conjugated structure of many COFs is capable of amplifying the fluorescence response from an individual COF–analyte interaction to create a bulk response of the entire COF scaffold through electron delocalization.<sup>188</sup> This effect resembles the “molecular wire effect” coined by Swager<sup>39,120,148</sup> for the sensing using conjugated organic polymers (COPs), in which the donor ability of COPs is enhanced in the excited state due to the delocalized  $\pi^*$  state, offering a platform for the easy migration of excitons to interact with analytes (acceptor). Critical to the implementation of this effect is the good dispersion of chromophores within bulk materials to avoid self-quenching.<sup>148</sup> While this design criterion has been achieved by using bulky groups in COPs, COFs can potentially offer a unique opportunity for strategic positioning of fluorescent subunits with atomic precision within porous scaffolds through reticular molecular engineering. Third, both the “bottom-up” and “post-synthetic” strategies can be applied to achieve specific and effective material–analyte interactions to enhance the selectivity and sensitivity of COF-based sensors.



So far, efforts in the use of COFs for chemical detection have been centered on the fluorescence quenching or enhancement triggered by analyte molecules. These investigations have revealed the potential of COFs in the quantitative detection of explosives based on nitroaromatics, heavy metal ions, small molecular compounds, and biologically relevant analytes. This section provides a detailed account of COFs in fluorescence detection of analytes by dividing the analytes into three groups: volatiles and gases, ions, and biology-related molecules.

### 2.2.2 Detection of volatiles and gases

**Nitroaromatics and other explosives.** Nitroaromatics, including 2,4,6-trinitrotoluene (TNT), dinitrotoluene (DNT), and 2,4,6-trinitrophenol (TNP), constitute an important group of explosives that possess high explosive efficacy. Some nitroaromatics, like TNP, also have mutagenic activities to cause acute health problems, such as headache, liver injury, and diarrhea. Nitroaromatics are also a major source of environmental pollution. Hence, the highly selective and sensitive detection of nitroaromatics has attracted research concern.

Zhu and coworkers synthesized a 3D crystalline porous aromatic framework (PAF-15) with high fluorescence quantum yield by assembling luminescent building blocks of tetra(4-dihydroxyborylphenyl)germanium (TBPGe) and 2,3,6,7,10,11-hexahydroxytriphenylene (HHTP).<sup>188</sup> PAF-15 exhibited a strong fluorescence with an absolute quantum yield of 14% as a suspension in  $\text{CHCl}_3$ . A distinct quenching effect was observed upon the addition of nitroaromatics such as nitrobenzene, 2,4-DNT, and TNT, which could result from the electrostatic interaction between PAF-15 and electron-deficient compounds.<sup>189</sup> The addition of other common aromatic compounds such as benzene, toluene, chlorobenzene, bromobenzene, phenol, and aniline did not affect the fluorescence intensity of PAF-15. Zhang *et al.* prepared nanoparticles of a new type of melamine-based Schiff base network SNW-1 by microwave-assisted synthesis for the detection of nitroaromatic explosives.<sup>183</sup> The as-synthesized SNW-1 nanoparticles exhibited high sensitivity and selectivity, as well as fast response to TNT, 2,4,6-trinitrophenylmethyl nitramine, and TNP without interference by common organic solvents (Fig. 7). Time-dependent fluorescence quenching by DNT vapor showed a sharp increase in only 10 s. The detection limit for DNT vapor was 9.8 ppb, comparable with porous silicon films. The authors ascribed the observed sensing performance for these nitroaromatic explosives to the nanoscale size and unique hierarchical porosity of such fluorescence-based sensing material.<sup>183</sup>

Although these earlier studies demonstrate promising application of COFs for the detection of electron-deficient nitroaromatics over other chemical species,<sup>183,188</sup> selective detection of certain nitroaromatics is still challenging because of the limited selectivity of the interaction between the analyte and COFs. To improve the sensitivity and selectivity for nitroaromatics, two main approaches have been adopted to engineer the chemical structures of COFs: (1) the introduction of active binding sites<sup>160,190–192</sup> and (2) the adjustment of the electronic feature of the fragments in COFs through the choice of building blocks.<sup>193,194</sup> Both these methods can tune the material-analyte interactions electronically.

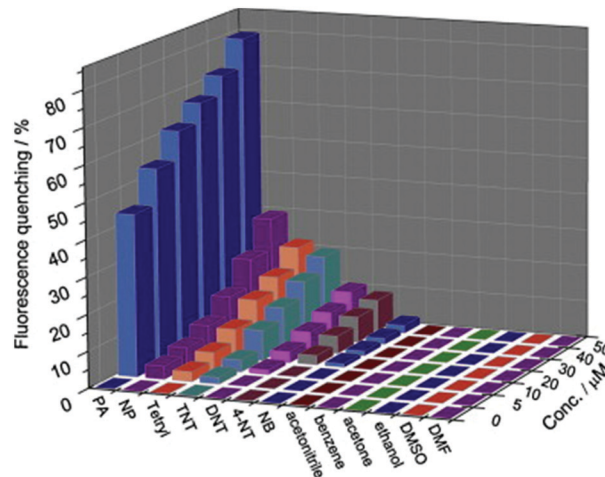


Fig. 7 Fluorescence quenching results of nitroaromatic explosives and interferents to the emission of the SNW-1 nanoparticles at various concentrations in a THF/H<sub>2</sub>O (1:9, v/v) mixture.<sup>183</sup> Adapted with permission from ref. 183. Copyright 2012, Elsevier.

For example, Jiang and coworkers reported the development of an azine-linked COF Py-Azine with high crystallinity, porosity, and robust chemical stability for the selective detection of TNP.<sup>160</sup> In the Py-Azine COF, the pyrene units at the vertices and the azine linkers on the edges of 2D polygon sheets stack to form periodic pyrene columns and one-dimensional channels with exposed azine units on the pore walls (Fig. 8a). The authors found that these azine units can provide open docking sites for forming hydrogen-bonding interactions with guest molecules,<sup>195</sup> resulting in fluorescence quenching and achieving selective detection of guests. When the suspension of the Py-Azine COF was exposed to the TNP vapor, the COF fluorescence was quickly quenched.

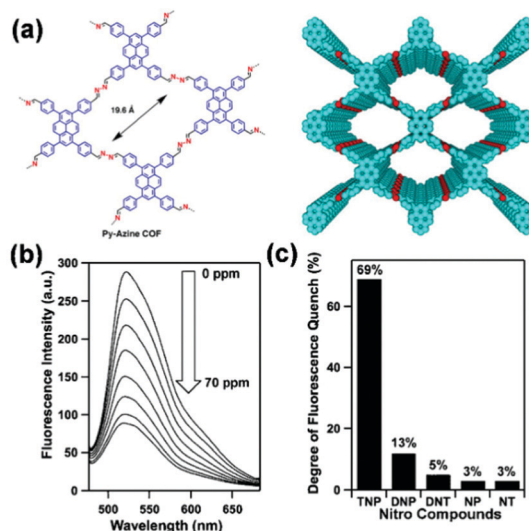


Fig. 8 (a) Chemical structure and model of COF Py-Azine. (b) Fluorescence quenching of the Py-Azine COF upon the addition of TNP in acetonitrile. (c) Degree of fluorescence quenching upon addition of the nitro compounds (70 ppm).<sup>160</sup> Adapted with permission from ref. 160. Copyright 2013, American Chemical Society.



The fluorescence quenching reached 69% in response to a concentration of TNP in acetonitrile that was as low as 70 ppm (Fig. 8b). When other nitrobenzene compounds were tested under the same condition, fluorescence quenching of the COF was only 13%, 5%, 3%, and 3% for DNP, DNT, NP, and NT, respectively (Fig. 8c). The authors proposed that the selective detection of TNP among other nitrobenzene compounds may result from the hydroxy unit and the three nitro groups of TNP that form hydrogen-bonding interactions with the open nitrogen atoms in the azine units on the pore walls and provides the most deficient  $\pi$ -system for driving the fluorescence quenching.<sup>160</sup>

Since the aggregated layers in the bulk form may mask active sites, bulk COFs can exhibit ineffective interaction with analytes, leading to moderate chemical sensing ability. To address this shortcoming, Banerjee and coworkers exfoliated the aggregated  $\pi$ -stacked COF layers using the liquid phase exfoliation

method to produce covalent organic nanosheets (CONs) from imide-based COFs (TpBDH and TfpBDH, Tp, 1,3,5-triformylphloroglucinol, Tfp, 1,3,5-tris(4-formylphenyl)benzene, BDH, pyromellitic-*N,N'*-bisaminoimide, Fig. 9a).<sup>190</sup> TfpBDH-CONs showed up to 10 times increased luminescence intensity in both isopropyl alcohol solution and in solid-state (deposited on paper strips) compared to their bulk counterparts. TfpBDH-CONs exhibited maximum *ca.* 63% quenching efficiency towards TNP at  $5.4 \times 10^{-5}$  M concentration in IPA over other nitroaromatic explosives (TNT: 31%, DNT: 3%, DNP: 23%, and NP: 4%), which can be attributed to the electronic charge transfer from the HOMO of the picrate anion ( $\text{TNP}^-$ ) to the LOMO of the protonated TfpBDH-CONs (Fig. 9b and c). The fluorescence lifetime reduced sharply with the increase of TNP concentration, suggesting that the quenching was dynamic. On the other hand, in the solid state, a “turn-on” type detection capability for TNP was

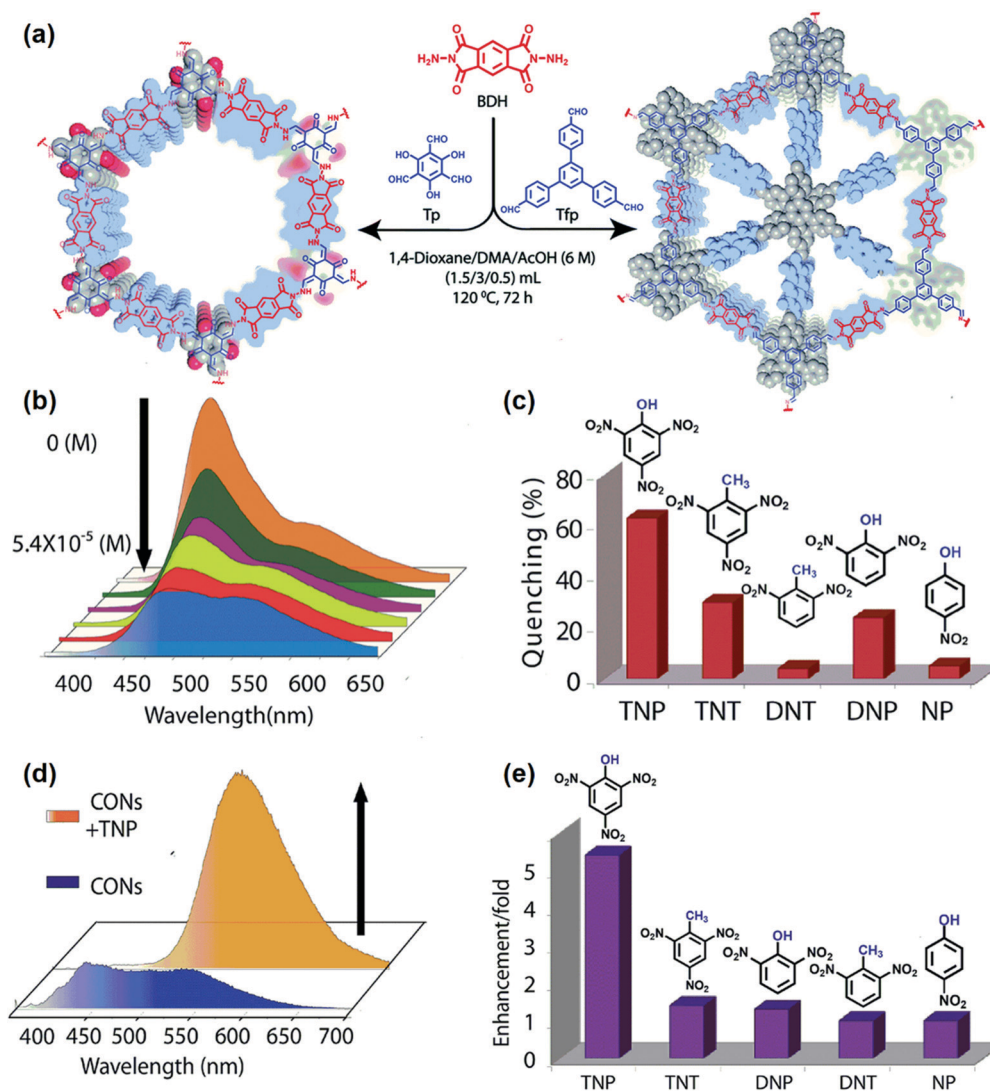


**Fig. 9** (a) Schematic of the synthesis of TpBDH-CONs and TfpBDH-CONs. (b) Fluorescence “turn-off” sensing using TfpBDH-CONs in an isopropyl alcohol solution. (c) The selectivity of TfpBDH-CONs towards TNP based on fluorescence quenching. (d) Fluorescence enhancement of “turn-on” sensing in the solid phase. (e) The selectivity of TfpBDH-CONs towards TNP based on fluorescence enhancement.<sup>190</sup> Adapted with permission from ref. 190. Copyright 2015, Royal Society of Chemistry.





observed. This “turn-on” sensing behavior in the solid state could be due to the proton transfer from TNP to the basic nitrogen atom of the imine ( $-C=N-$ ) bond. The PL emission maxima in the solid state were red-shifted and enhanced by 10 times under  $10^{-3}$  M TNP (Fig. 9d). Other nitroaromatics did not show significant effects on TfPBDH-CONS in the solid state (Fig. 9e). These findings described a new approach towards developing efficient fluorescence chemosensor materials for both visual and spectroscopic detection of nitroaromatic compounds.

COFs in the form of nanosheets were also recently made by Xian and coworkers for sensitive detection of TNP.<sup>191</sup> Few-layered polyimide CONS (PI-CONS) were exfoliated from bulk PI-COF made of tetra(4-aminophenyl) porphyrin and perylene-tetracarboxylic dianhydride, which showed enhanced activity relative to that of PI-COF. The fluorescence intensity of PI-CONS gradually reduced with the increasing concentration of TNP. This fluorescence quenching can be attributed to a combination of ground-state electron transfer from  $TNP^-$  to PI-CONS and the inner filter effect (IFE) in which the excitation and/or emission light of PI-CONS was partly absorbed by TNP. This approach provided a detection limit of 0.25  $\mu$ M. Other interferents, including nitrobenzene (NB), nitrotoluene (NT), DNT, TNT, 4-chlorophenol (MCP), and hydroquinone (HQ), had negligible impacts on the detection of TNP because of the less efficient charge transfer and IFE between these interferents and PI-CONS. More recently, Zamora and coworkers reported the application of exfoliated nanosheets of pyrene-IMDEA-COF for the sensing of aromatic pollutants in water.<sup>196</sup> The colloidal IMDEA-COF-1 nano-layers showed remarkable fluorescence towards a variety of organic pollutants and dyes, including NB, dinitrobenzene (DNB), and methylene blue (MB).

Although being widely used,<sup>190,191</sup> COFs with conventional Schiff base structures can have limited hydrolytic stability in acid and base, or even in the presence of water, which is a concern for their long-term stability in detection under harsh conditions. H-bonded keto-enamine type COFs, instead, can give highly stable and crystalline structures compared with conventional Schiff base structures, thus providing an effective solution for the stability issues.<sup>85,88</sup> Toward this end, Bhaumik and coworkers reported a new triazine functionalized keto-enamine based COF TRIPTA that introduced high thermal and chemical stability.<sup>192</sup> TRIPTA was found to be highly luminescent when suspended in polar solvents upon irradiation and was able to detect various nitroaromatic compounds with good sensitivity by fluorescence quenching at concentrations as low as  $10^{-8}$  M. The maximum fluorescence quenching was observed for TNP (61.7% at  $5.46 \times 10^{-7}$  M) with a Stern-Volmer constant of  $2.7 \times 10^6$  M<sup>-1</sup>.

Since nitroaromatics possess electron-deficient rings, embedding fragments with strategically chosen electronic features into COFs represents another effective way to facilitate charge transfer interaction for the improvement of sensitivity, as well as selectivity over other non-aromatic interferents. Murugavel and coworkers found that electron-rich amine substituted triphenylbenzenes (TAPB) can interact with nitroaromatics in the solid-state and can serve as effective fluorescence

sensors for nitroaromatic analytes.<sup>197–199</sup> Inspired by those studies, the authors integrated the TAPB fluorophore into imine and  $\beta$ -ketoenamine based COFs for the detection of nitroaromatics.<sup>193</sup> The fluorescence of those COFs was effectively quenched in the presence of different nitroaromatic compounds, such as TNP, DNT, *p*-DNB, and *m*DNB, among which TNP was the most efficient quencher, probably because of the proton transfer from TNP to the nitrogen atoms of the COFs. The aromatic electron-rich triphenylamine group was also incorporated into COF-BABD-BZ (BABD, 1,4'-bis(4-formylphenyl)amino)-[1,10-biphenyl]-3,5-dicarbaldehyde, BZ, benzidine) by Dai and coworkers for the detection of TNP.<sup>200</sup> The COF showed a quick color change in its fluorescence from golden yellow to dark brown upon the addition of TNP and exhibited good selectivity towards TNP compared to other nitroaromatics.

Incorporating both  $\pi$ -electron rich and  $\pi$ -electron deficient cores into COFs can lead to an enhancement in the strength and selectivity of material-analyte interactions, thus enabling the recognition of aromatics from other volatiles. Das and Mandal reported the differentiation of  $\pi$ -electron rich and  $\pi$ -electron deficient aromatics with similar structures and physical properties using COF **1**. This COF bears a  $\pi$ -electron deficient triazine core and a  $\pi$ -electron rich naphthalene core connected with  $-O-$  and  $=N-$  donor Lewis basic sites (Fig. 10a).<sup>194</sup> The recognition was based on a dual readout constructed from the lifetime or emission intensity and quantum yield of COF **1**, which was highly dependent on the interaction with aromatics.<sup>194</sup> The electron-deficient triazine core in COF **1** allowed the selective uptake of a  $\pi$ -electron rich unsaturated moiety (benzene) over its saturated congener (cyclohexane); in turn, the electron-rich core was very efficient for the selective and ultra-low detection of highly explosive TNP in water down to 68 ppb (Fig. 10b). The rapid real-time detection of nitroaromatic compounds can be realized through both contact mode and instant spot measurement mode by immobilizing COF **1** on paper strips (Fig. 10c).

Incorporating aromatic units is a straightforward way to construct fluorescent COFs; however, the majority of 2D COFs, which have large periodic  $\pi$ - $\pi$  stacked structures, exhibit limited emissive characteristics due to aggregation-caused quenching (ACQ). Highly fluorescent COFs are still in great demand for chemical detection. To circumvent the ACQ effect, the introduction of an AIE moiety has been proven to be an effective strategy to afford highly emissive 2D COFs, because the intralayer covalent linkages and interlayer  $\pi$ -interaction can work synergistically to impede the rotation-induced energy dissipation (see also Section 2.2.1 discussed earlier).<sup>173</sup> Recently, Loh and coworkers developed highly luminescent (quantum yield up to 21.1%) imine-based Py-TPE-COF by the integration of a non-planar tetraphenylethene (TPE) building unit with a pyrene unit.<sup>201</sup> The photoluminescence intensity decreased monotonically with the addition of TNP, and the quenching percentage increased to 95.5% at 10 ppm TNP. Upon exposure to other non-explosive molecular analogs with similar structures, including DNP, DNT, NT, and 2-nitrophenol (NP), Py-TPE-COF showed only a small to marginal decrease (<15.6%) in the PL intensity.



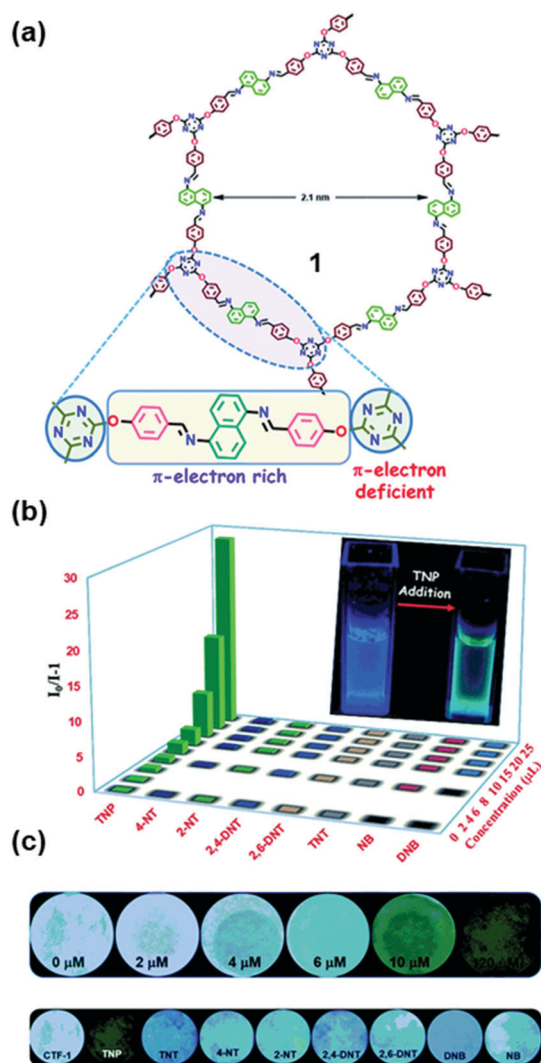


Fig. 10 (a) Chemical structure of COF **1** containing both electron rich and electron deficient units. (b) Stern–Volmer plot of all of the analytes in water showing high selectivity for TNP. (c) Photograph of Whatman filter paper strips coated with **1** and different concentrations of TNP (upper row) and paper strips coated with **1** and 20  $\mu\text{M}$  concentration of different nitroaromatics (lower row).<sup>194</sup> Adapted with permission from ref. 194. Copyright 2018, Royal Society of Chemistry.

In most of the examples demonstrated above, one of the important features of COFs being utilized is the face-to-face stacking modes of their 2D sheets. Unlike the layered structures in 2D COFs, 3D COFs can possess more open sites that can be beneficial for the material–analyte interaction. In addition, as the building blocks are isolated in the 3D network, the incorporation of fluorescent units into 3D COF can result in materials with interesting emissive properties that may be different from those of 2D analogs. Through the selective choice of the geometry of the precursors and the connection patterns, Wang and coworkers demonstrated the synthesis of a novel 3D pyrene-based COF 3D-Py-COF (Fig. 11a and b) and its potential in explosive detection.<sup>177</sup> 3D-Py-COF adopted a two-fold interpenetrated pts topology and showed an intense yellow-green luminescence with a band centered at 484 nm (Fig. 11c).

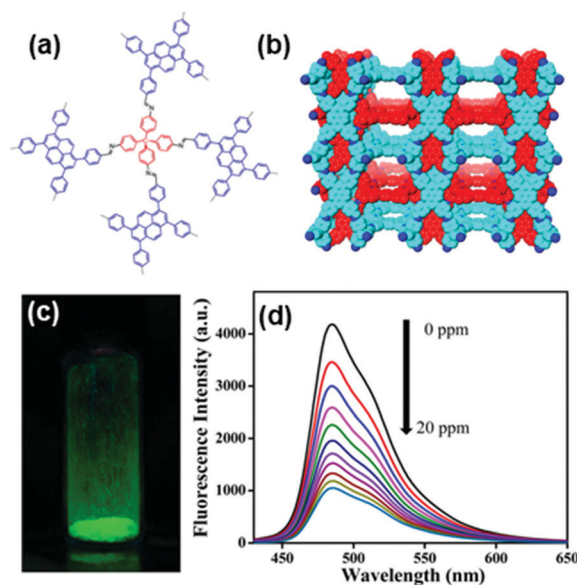


Fig. 11 (a) Chemical structure and (b) the space-filling model of 3D-Py-COF with a two-fold interpenetrated pts network. (c) Photography of the 3D-Py-COF powders under UV light irradiation. (d) Fluorescence quenching upon addition of PA in DMF.<sup>177</sup> Adapted with permission from ref. 177. Copyright 2016, American Chemical Society.

The gradual addition of TNP quenched the fluorescence of the 3D-Py-COF suspension (Fig. 11d). When the concentration of TNP was 20 ppm, a fluorescence quenching degree of 75% was reached with a Stern–Volmer curve quenching constant ( $K_{sv}$ ) of  $3.1 \times 10^4 \text{ M}^{-1}$ , indicating that 3D-Py-COF was sensitive to TNP.

*Acid/base and other vapors.* Jiang and coworkers developed a highly luminescent COF (Fig. 12a) TPE-Ph by introducing an AIE-active tetraphenylethene (TPE) unit which showed sensitive response to  $\text{NH}_3$  gas.<sup>173</sup> The TPE-Ph COF exhibited a high luminescence quantum yield of up to 32%, which was 2- to 3-fold that of the tetraphenylethene molecule. This enhancement suggested that the  $\pi$ – $\pi$  interactions between layers of COFs, which were absent in the molecular tetraphenylethene material, additionally contribute to the higher fluorescence quantum yield (Fig. 12b). Because the boronate linkages of the TPE-Ph COF can form a Lewis acid–base pair with ammonia, the TPE-Ph COF suspension exhibited rapid luminescence quenching upon ammonia exposure (Fig. 12c). Ammonia at the concentration of 1 ppm could lead to a 30% decrease of fluorescence intensity, demonstrating that the TPE-Ph COF was a highly sensitive ammonia detector at a sub-ppm level. The Stern–Volmer plot revealed an almost linear curve, whereas the fluorescence quenching rate constant was evaluated to be as high as  $4.1 \times 10^{14} \text{ M}^{-1} \text{ s}^{-1}$  (Fig. 12d). This work demonstrated that the utilization of the concept of AIE could lead to a new generation of highly luminescent COF materials that retain high quantum yields in both solid and solutions and function as highly sensitive sensors to detect specific chemicals.

Using the same type of fluorophore, Zhao and coworkers reported the detection of HCl gas with a TPE-based 2D COF



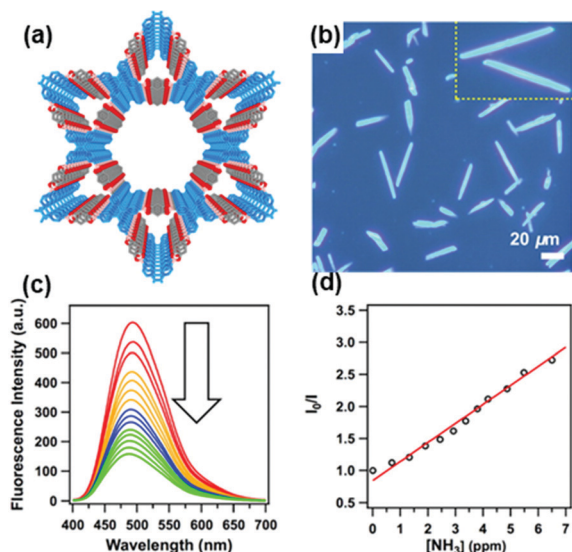


Fig. 12 (a) Structural representation of the TPE-Ph COF. (b) Fluorescence microscopy images of TPE-Ph COF samples. (c) Fluorescence spectral change of the TPE-Ph COF upon the addition of ammonia. (d) Stern-Volmer plot of fluorescence quenching by ammonia.<sup>173</sup> Adapted with permission from ref. 173. Copyright 2016, American Chemical Society.

COF-ETBA-DAB made of 4,4',4'',4'''-(ethane-1,1,2,2-tetrayl)tetra benzaldehyde (ETBA) and 1,4-diaminobenzene (DAB).<sup>141</sup> Upon exposure to HCl gas, COF-ETBA-DAB displayed a new emission band with a very strong intensity centered at 670 nm. Meanwhile, the color of the COF crystallites exhibited an obvious change from yellow to red upon less than 1 s HCl exposure, faster than most HCl gas sensors previously reported.<sup>202–204</sup> The addition of trace HCl with a concentration of 4.7 ppm could induce a significant change in the fluorescence emission of COF-ETBA-DAB, suggesting high sensitivity. The red color of the HCl-treated COF could be recovered to yellow upon exposure to ammonia vapor. Spectroscopic study indicated that the imine nitrogen atoms in COF-ETBA-DAB may undergo a quick protonation process in the atmosphere of HCl gas, which imparted an influence on the conjugated structure of the TPE skeleton, resulting in changes in the fluorescence emission as well as the color of the COF.<sup>141</sup>

From the perspective of their response mode, most fluorescent sensors rely on the measurement of a single intensity-varying fluorescence signal, which is prone to interference by the intensity of the excitation, collection efficiency of the emission signal, and inhomogeneous distribution of the probe. Instead, the ratiometric sensor has self-built-in corrections of two signal peaks and thus affords more accurate measurement over a single-output fluorescence sensor.<sup>205</sup> Yan and coworkers reported a rationally designed COF with dual fluorescence emissions for the ratiometric sensing of trace water in organic solvents.<sup>206</sup> 4,4',4''-(1,3,5-triazine-2,4,6-triyl)trianiline (Tz) and 2,5-dihydroxyterephthalaldehyde (Da) were chosen as the ligands to synthesize COF TzDa, where the Tz moiety can offer the docking sites and the Da moiety can provide the hydrogen bonds (Fig. 13a). The Tz moiety endowed the TzDa COF with an

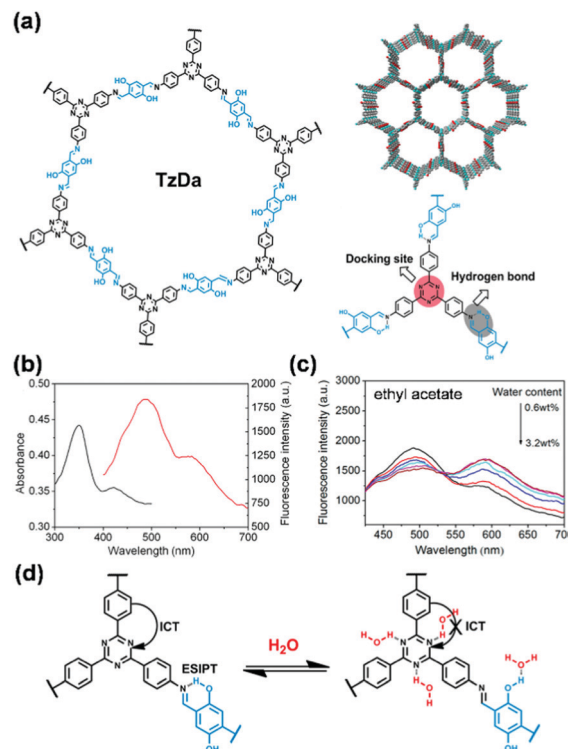


Fig. 13 (a) Chemical structure and model of TzDa and the illustration of the docking sites and hydrogen bond in TzDa. (b) UV-vis absorption (black) and fluorescence (red) spectra of TzDa in pure ethyl acetate. (c) Fluorescence spectra of TzDa in ethyl acetate with different water content. (d) H<sub>2</sub>O-sensing mechanism of TzDa.<sup>206</sup> Adapted with permission from ref. 206. Copyright 2017, American Chemical Society.

ICT effect, while the hydrogen-bonding interactions between Da and imine resulted in an excited-state intramolecular proton transfer effect. As a result, TzDa gave two main fluorescence emissions around 500 and 590 nm (Fig. 13b). The ratio of the two fluorescence emissions of TzDa linearly increased with the water content in organic solvents, such as ethyl acetate (Fig. 13c). Hydrogen bonding interactions between water and the Tz moiety blocked the ICT process from triazine to the phenyl group, increasing the possibility of nonradiative relaxation of TzDa, which consequently led to the decrease of fluorescence emission intensity at 500 nm (Fig. 13d). The TzDa COF can be used to detect trace amounts of water (0.006–0.085%) in various organic solvents, including isopropyl alcohol, acetone, tetrahydrofuran, ethyl acetate, and ethanol. Comparison experiments showed that the results obtained by using TzDa showed comparable accuracy with those obtained by gas chromatography in determining the water content in six commercial organic solvents.<sup>206</sup>

**Others.** Qin and coworkers demonstrated the use of mechanochromic luminescent COF systems for highly selective detection of hydroxyl radicals ( $\bullet$ OH).<sup>207</sup> The fluorescence intensity of COF-TpMA exhibited linear fluorescence quenching with the  $\bullet$ OH concentration (0–10 μM), and was mostly unperturbed by the other reactive oxygen species. The mechanistic study





indicated that fluorescence quenching was likely a static quenching attributed to the electron transfer of hydroxyl radicals to the  $\pi$ -conjugated framework that induced aggregation.<sup>176</sup> COF-TpMA was also applied for the detection of exogenous  $\bullet\text{OH}$  in living cells.

**2.2.3 Detection of ions.** Ions represent a large group of analytes that are of increasing ecological and health concern associated with environmental contamination of global natural resources. In particular, metal ions released from industrial processes, most typically in the form of heavy metal ions, are non-biodegradable and ubiquitously distributed, which leads to considerable risk to human health and the environment.<sup>208</sup> Heavy metals, like lead, cadmium, arsenic, chromium, and mercury, can cause extensive contamination of drinking water and agricultural products and are considered as hazardous even at lower concentrations.<sup>209,210</sup> Some metal ions, like iron, copper, cobalt, zinc, manganese, *etc.*, are required by the living organisms in lower quantity, but when present at higher concentrations lead to toxic effects.<sup>211</sup> Moreover the imbalance of ionic electrolytes can result in several life-threatening conditions in biological systems, including cardiac arrest, neurological disorders, or kidney failure.<sup>212</sup> Therefore, there is a great demand to develop rapid, sensitive, and simple analytical platforms for the detection and monitoring of metallic contaminants in water, food, soil, and biological samples.

The use of fluorescent COFs has enabled the detection of various metal ions, including  $\text{Cr}^{3+}$ ,  $\text{Hg}^{2+}$ ,  $\text{Cu}^{2+}$ ,  $\text{Fe}^{3+}$ ,  $\text{Au}^{+}$  and  $\text{Al}^{3+}$ , protons (pH), as well as  $\text{F}^{-}$  anions. The detection of metal ions is mostly based on fluorescence switching due to the charge transfer between metal ions and excited states of COFs, whereas the detection of protons and  $\text{F}^{-}$  is based on fluorescence change resulting from the formation of the protonated and deprotonated complex of COFs in the presence of protons and  $\text{F}^{-}$ , respectively.

**Metal ions.** Oxygen-containing and nitrogen-containing groups, such as  $-\text{C}=\text{N}-$ ,  $-\text{NH}_2$ ,  $\text{C}=\text{O}$ , and  $-\text{OH}$ , are ubiquitous in a lot of COF structures. These groups can be formed during COF formation, embedded in the building blocks, or present at the edges and defect sites of COF crystallites. These groups generally have binding affinities to various metal ions because of the lone pair electrons in these moieties. This feature of COFs has been harnessed to achieve the detection of metal ions, though the design rules for selectivity have not always been deliberate.

For example, Qiu and coworkers prepared nanosheets of a luminescent crystalline polyimide (PI) for  $\text{Cr}^{3+}$  sensing.<sup>213</sup> The PI nanosheets were examined for luminescence detection toward a series of metal ions. It was found that PI nanosheets were highly sensitive and selective in the detection of  $\text{Cr}^{3+}$  over the interference of other metal ions, such as  $\text{K}^{+}$ ,  $\text{Ca}^{2+}$ ,  $\text{Cd}^{2+}$ ,  $\text{Pb}^{2+}$ ,  $\text{Mn}^{2+}$ ,  $\text{Hg}^{2+}$ ,  $\text{Mg}^{2+}$ ,  $\text{Co}^{2+}$ ,  $\text{Cu}^{2+}$ , and  $\text{Zn}^{2+}$ . The selectivity for  $\text{Cr}^{3+}$  was attributed to differences in coordination bonding (coordination mode or bonding strength) between various metal ions and nitrogen/oxygen atoms in the PI framework. The authors hypothesized that binding of the PI framework to

$\text{Cr}^{3+}$  may reduce the antenna efficiency of the PI frameworks, and result in quenching of the luminescence. In another example, Fan and coworkers utilized the triazine units and edge nitrogenous groups of quantum dots made from CTF-1 to detect  $\text{Hg}^{2+}$ .<sup>214</sup> The purpose of employment of quantum dots was the more abundant edge groups in the quantum dot form of COF CTF-1 than in the bulk form.

Strategic improvement of selectivity for specific ions can be achieved by introducing active sites that exhibit selective recognition ability for the analyte of interest. Examples can be seen in the selective detection of  $\text{Hg}^{2+}$ <sup>175</sup> and  $\text{Au}^{+}$ .<sup>215</sup> Generally, to achieve high sensitivity, unique selectivity, and simple handling, fluorescent organosulfur compounds are used as effective  $\text{Hg}^{2+}$  chemosensors.<sup>216–218</sup> Inspired by these precedents, Wang and coworkers reported the first application of fluorescent COFs for detecting and removing  $\text{Hg}^{2+}$  ions by introducing evenly and densely distributed thioether side chains into COF-LZU8.<sup>175</sup> This bottom-up construction of COF-LZU8 not only generated a rigid and extended  $\pi$ -conjugation framework as the signal transducer but also embedded the thioether side chains as the cation receptor for  $\text{Hg}^{2+}$  (Fig. 14a). The contorted structure of COF-LZU8 enabled efficient avoidance of the ACQ effect,<sup>178</sup> thereby, imparting this COF with high fluorescence both in the solid state and in the dispersion form, in contrast to its building blocks. Upon the addition of  $\text{Hg}^{2+}$ , COF-LZU8 showed efficient fluorescence quenching (Fig. 14b). Comparison experiments using a structurally related COF without thioether side chains suggested that the quenched fluorescence originated from the interaction between the thioether groups of the COF and  $\text{Hg}^{2+}$ , which resulted in electron transfer from the COF to the LUMO of  $\text{Hg}^{2+}$ . Among various metal ions examined, only  $\text{Hg}^{2+}$  caused a significant fluorescence quenching of COF-LZU8 (Fig. 14c and d).<sup>175</sup> The detection limit for  $\text{Hg}^{2+}$  was 25.0 ppb, superior to many thioether-functionalized chemosensors.<sup>219–221</sup> Besides the excellent selectivity and sensitivity for detecting  $\text{Hg}^{2+}$ , COF-LZU8 was also able to effectively remove >98%  $\text{Hg}^{2+}$  in water with residual  $\text{Hg}^{2+}$  less than 0.2 ppm. This COF material may serve as a new candidate with intrinsic multipurpose functionalities for simultaneous detection and removal of toxic metal ions.<sup>175</sup>

Although the fluorescence quenching effect can provide straightforward luminescence change that often can be directly visualized, the sensitivity of the detection depends on the magnitude of the fluorescence change. Therefore, the use of highly fluorescent COFs is one applicable way to enhance sensitivity. For example, Liu and coworkers introduced bulky *tert*-butyl groups into COF-JLU3 to adjust the  $\pi$ - $\pi$  interaction between the layers to increase the luminescence efficiency for the detection of  $\text{Cu}^{2+}$ .<sup>176</sup> COF-JLU3 exhibited high luminescence efficiency with an absolute fluorescence quantum yield of 9.91%. The fluorescence emission of COF-JLU3 showed a proportional decrease with the concentration of  $\text{Cu}^{2+}$  ions in the range from 0 to 0.4 mM with a LOD determined at 0.31 mM and good selectivity over other interfering ions, such as  $\text{Li}^{+}$ ,  $\text{Na}^{+}$ ,  $\text{K}^{+}$ ,  $\text{Mg}^{2+}$ ,  $\text{Ca}^{2+}$ ,  $\text{Ba}^{2+}$ ,  $\text{Zn}^{2+}$ ,  $\text{Cd}^{2+}$ ,  $\text{Ni}^{2+}$ ,  $\text{Pb}^{2+}$ , *etc.* Alternatively, using a strategy that resembles the AIE concept, Jiang



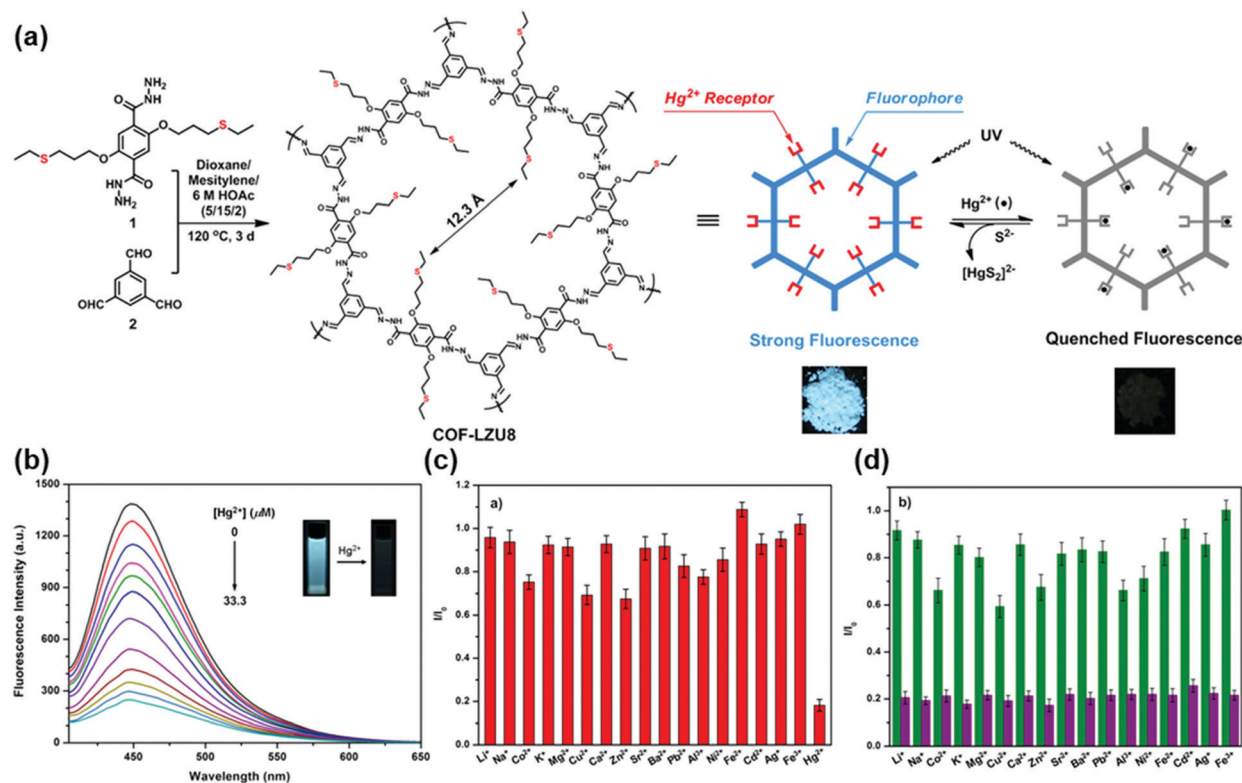


**Fig. 14** (a) Synthesis and structure of COF-LZU8. (b) Fluorescence titration of COF-LZU8 dispersed in acetonitrile upon the gradual addition of  $Hg^{2+}$  ( $\lambda_{ex} = 390$  nm). Inset: Fluorescence titration of COF-LZU8 dispersed in acetonitrile upon the gradual addition of  $Hg^{2+}$ . Selectivity of COF-LZU8 toward  $Hg^{2+}$  detection: (c) fluorescence response of COF-LZU8 in the presence of different metal ions (33.3  $\mu M$ ) in acetonitrile and (d) competition experiments. The green bars in (d) represent the emission intensity of COF-LZU8 in the presence of the competing ions (2.0 eq.), and the purple bars represent the emission intensity upon the addition of  $Hg^{2+}$  (1.0 eq.) to the above solutions.<sup>175</sup> Adapted with permission from ref. 175. Copyright 2016, American Chemical Society.

and coworkers developed a series of highly emissive carbon-conjugated frameworks ( $sp^2c$ -COFs) constructed by C=C linkages, which showed selectivity for  $Cu^{2+}$ .<sup>222</sup> The backbone between two proximate pyrene knots consisted of a cyano-substituted phenylenevinylene adopting twisted conformation, which served as an AIE-like chromophore to avoid the aggregation-caused fluorescence quenching (Fig. 15a).<sup>223</sup> The highly emissive property of  $sp^2c$ -COFs compared with the constituent monomer 1,3,6,8-tetrakis(4-formylphenyl)pyrene (TFPPy, Fig. 15b), as well as the cyano side groups in the frameworks that can serve as a ligand for triggering supramolecular interactions with specific metal species, renders  $sp^2c$ -COFs the ability to detect specific guest species. The addition of  $Cu^{2+}$  quenched the fluorescence intensity of  $sp^2c$ -COF in THF (Fig. 15c). By contrast, the addition of  $Zn^{2+}$  which cannot ligate with the -CN groups could not quench the emission (Fig. 15d). These results suggested that interaction with cyano groups was essential for triggering fluorescence sensing.  $sp^2c$ -COF was highly sensitive to the  $Cu^{2+}$  ion and achieved a LOD of 88 ppb.<sup>222</sup>

In addition to detecting  $Cr^{3+}$ ,  $Hg^{2+}$ ,  $Au^+$ , and  $Cu^{2+}$  ions mentioned above, fluorescent COFs were also applied for the sensing of  $Fe^{3+}$ ,<sup>184,224–227</sup>  $Al^{3+}$ ,<sup>228</sup> and  $UO_2^{2+}$ .<sup>229</sup> The introduction of cites with strong metal binding affinity can enhance the

sensitivity of detection for metal ions. For example, Chen and coworkers reported the TaDAP COF constructed by the condensation between 1,3,5-tris-(4-aminophenyl)triazine and 2,6-diformylpyridine, which was able to detect  $Fe^{3+}$  in the range of 0.02–0.2 mM.<sup>225</sup> However, only a moderate sensitivity with a LOD of 18  $\mu M$  can be achieved, probably because  $Fe^{3+}$  binding provided by the unidentate pyridine or triazine in the TaDAP COF was relatively weak.<sup>225</sup> By utilizing a strong chelating effect, Zhang and coworkers designed and synthesized a hydrazone-linked COF Bth-Dma, which showed improved sensitivity for the detection of  $Fe^{3+}$  ions in aqueous solution.<sup>226</sup> The chelation between  $Fe^{3+}$  and the COF was realized by the predesigned *O,N,O'*-chelating sites in the pore wall of the Bth-Dma COF,<sup>227</sup> which can affect fluorescence quenching through energy or electron transfer between the excited states of the COF and the d-orbital of  $Fe^{3+}$ .<sup>230</sup> As a “turn-off” type fluorescence sensor, the Bth-Dma COF could achieve a low LOD of 0.17  $\mu M$  in a wide dynamic response range of 0.5–100  $\mu M$   $Fe^{3+}$ .

In the examples mentioned above, the fluorescence quenching mechanism was used in the detection process. The dissipation of excitation energy by photo-induced electron transfer upon metal ion binding is usually responsible for this “turn-off” type response. Compared with the turn-off mechanism, the advantage of the fluorescence turn-on mechanism in detection is that if



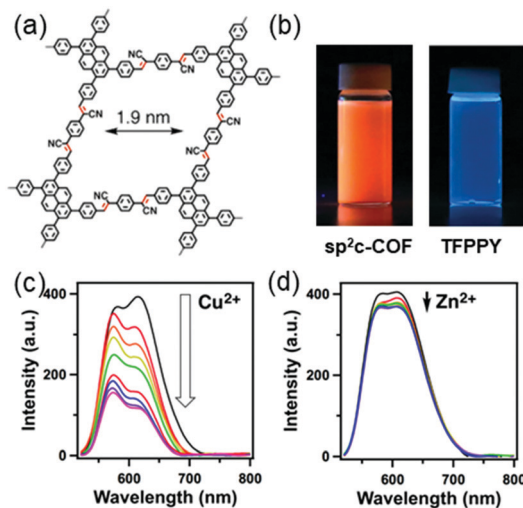


Fig. 15 (a) Chemical structure of  $\text{sp}^2\text{c-COF}$ . (b) Images of  $\text{sp}^2\text{c-COF}$  and the TFPy monomer dispersed in water under a UV lamp. Fluorescence spectral change of  $\text{sp}^2\text{c-COF}$  upon addition of (c)  $\text{Cu}^{2+}$  and (d)  $\text{Zn}^{2+}$  ions.<sup>222</sup> Adapted with permission from ref. 222. Copyright 2018, Springer Nature.

a completely dark background (completely quenched state) can be achieved, even a weak turn-on signal can be readily measured and thereby can allow trace detection.<sup>231,232</sup> The construction of turn-on type fluorescence detection relies on the mediation of the luminescence or quenching mechanism by utilizing an appropriate molecular design.

In some COFs, the luminescence properties can be primarily dependent on the linkers. When the photoinduced electron transfer process occurs in the linkers, it can cause excitation energy dissipation and lead to weak photoluminescence. In this case, preventing the fluorescence quenching process by coordinating the COF with metal ions can relieve the PET process, providing a promising approach to achieve “turn-on” type fluorescence detection. Using this strategy, Qiu and coworkers reported the first “turn-on” fluorescence sensor used for highly sensitive and selective detection of  $\text{Al}^{3+}$  based on COF nanosheets Bpy-NSs that incorporated bipyridine linkers.<sup>228</sup> The coordination of bipyridine sites in Bpy-NSs with  $\text{Al}^{3+}$  can eliminate the fluorescence quenching process caused by photoinduced electron transfer to result in a fluorescence “turn-on” effect (Fig. 16a). The fluorescence linearly increased with  $\text{Al}^{3+}$  concentration and achieved a 15.7-fold improvement with absolute fluorescence quantum yield increased from 0.15% to 1.74% (Fig. 16b). Although bipyridine has been reported to have coordination affinities to a few transition metal ions (e.g.,  $\text{Cu}^{2+}$ ,  $\text{Fe}^{3+}$ , and  $\text{Co}^{2+}$ ),<sup>233</sup> metal ions, including  $\text{Zn}^{2+}$ ,  $\text{Cd}^{2+}$ ,  $\text{Mn}^{2+}$ ,  $\text{Cr}^{3+}$ ,  $\text{Pb}^{2+}$ ,  $\text{Mg}^{2+}$ , etc., had little effect on the fluorescence of Bpy-NSs (Fig. 16c). The authors ascribed this selectivity to the higher energy levels of unoccupied d orbitals of the interfering ions than the 3s and 3p orbitals of  $\text{Al}^{3+}$ ; therefore, PET could not be effectively eliminated by these interfering ions.<sup>228</sup>

In addition to metal ions, fluorescent COFs were also used for pH detection in aqueous media.<sup>234,235</sup> pH is fundamental to

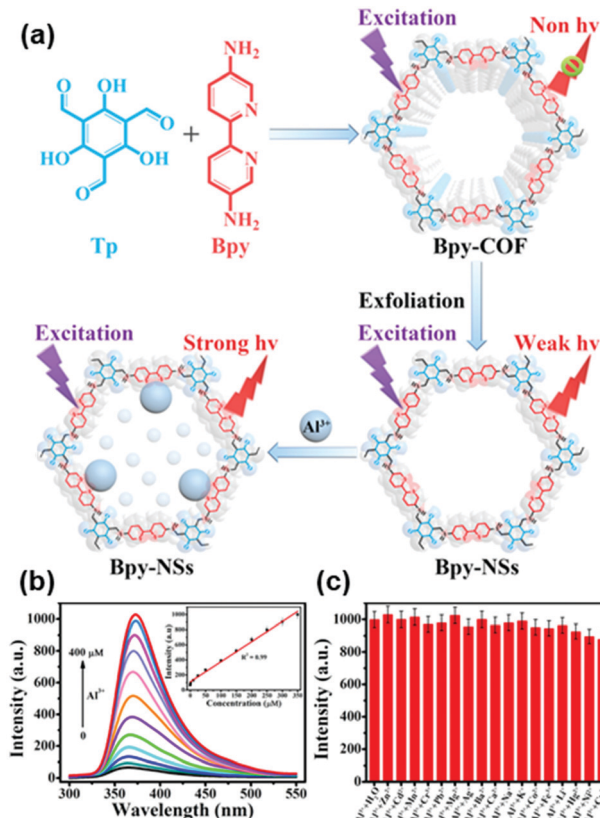


Fig. 16 (a) The schematic diagram for preparation of Bpy-NSs and detection of  $\text{Al}^{3+}$  in which  $\text{Al}^{3+}$  binding at the bipyridine sites inhibits the photoinduced electron transfer to result in a fluorescence “turn-on” effect. (b) Fluorescence spectral changes of Bpy-NSs after the addition of different concentrations of  $\text{Al}^{3+}$ . The inset is a linear calibration plot for  $\text{Al}^{3+}$  detection. (c) Fluorescence intensity changes of Bpy-NSs at 370 nm in the presence of  $\text{Al}^{3+}$  and other metal ions (350  $\mu\text{M}$ ).<sup>228</sup> Adapted with permission from ref. 228. Copyright 2019, American Chemical Society.

biological function and its measurement is therefore crucial across all biosciences. Although fluorescent COFs show great potential in the detection of organic volatiles, the weak stability and hydrophobicity of general Schiff base-based skeletons in aqueous solution can restrict their potential application in pH sensing. For developing pH-sensing systems, Liu and coworkers developed a  $\beta$ -ketoenamine based 2D COF (COF-JLU4), which had outstanding hydrolytic stability because of the stable and hydrophilic ketoenamine linkages.<sup>234</sup> The fluorescence intensity of COF-JLU4 decreased gradually with the increase of pH from 9.0 to 13.0 (Fig. 17a), which was attributed to the deprotonation process of the nitrogen in the framework.<sup>236</sup> When the pH was below 4.5, the luminescence emission at 428 nm increased dramatically with the decrease of pH. The fluorescence enhancement and blue-shift in acidic solution may be raised from the protonation of nitrogens (Fig. 17b). This pH-dependent fluorescence change could be recycled multiple times with similar degrees of fluorescence quenching (Fig. 17c and d).<sup>234</sup>

Compared with the detection of cations, the fluorescence detection of anions using COFs is currently less explored. This situation is probably because the interactions between COFs





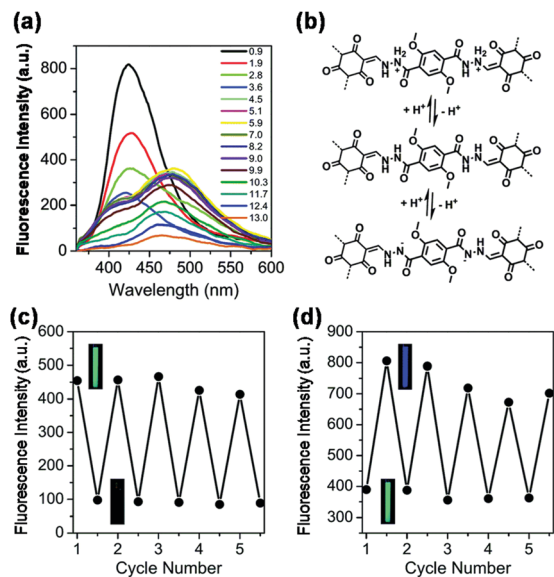


Fig. 17 (a) pH-Dependent fluorescence of COF-JLU4 in aqueous solutions with pH ranging from 0.9 to 13.0 measured under excitation at 334 nm. (b) Deprotonation and protonation processes of the COF-JLU4 framework in acidic and basic media. Reversible optical responses of COF-JLU4 (c) between the neutral (pH = 7.0) and basic conditions (pH = 13.0) and (d) between the neutral (pH = 7.0) and acidic conditions (pH = 1.0).<sup>234</sup> Adapted with permission from ref. 234. Copyright 2016, Royal Society of Chemistry.

and anions are still less explored and not well established. So far, the only report for the detection of anions is for  $F^-$ , which was achieved by Jiang and coworkers using TFPPy-DETHz-COF synthesized by condensation of 1,3,6,8-tetrakis(4-formylphenyl)pyrene (TFPPy) and 2,5-diethoxyterephthalohydrazide (DETHz).<sup>237</sup> The key to realizing the detection of  $F^-$  was the so-called pinpoint surgery on the nitrogen site of the hydrazone linkage by  $F^-$ , which scissored the N-H bond to give an  $N^-$  anion. This reaction eliminated the fluorescence quenching pathway and enabled an improvement of the light-emitting activity of the COF (Fig. 18a and b).<sup>237</sup> This COF emitted a weak green-yellow luminescence at 540 nm in THF with an absolute fluorescence quantum yield of only 4.5%. The addition of tetrabutylammonium fluoride to the THF dispersion of TFPPy-DETHz-COF increased the absolute fluorescence quantum yield to 17%, 3.8 fold that of the original one (Fig. 18c); on the other hand, other anions, including  $Cl^-$ ,  $Br^-$ ,  $I^-$ , and  $NO_3^-$ , did not change the luminescence under otherwise the same conditions (Fig. 18d and e). Time-resolved fluorescence spectroscopy suggested that the deprotonation of -NH groups by  $F^-$  ions suppressed the electron transfer from the linkage to the pyrene skeleton. Other halogen anions were inert because of their incapability to initiate the deprotonation of the -NH group. TFPPy-DETHz-COF was not only a switch-on type sensor but also showed high sensitivity to  $F^-$  with a detection limit down to 50.5 ppb (Fig. 18f), which was ranked the best among  $F^-$  sensors.<sup>238</sup>

**2.2.4 Detection of biological and biomedically relevant species.** Biomolecules, such as DNA, proteins, and amino acids,

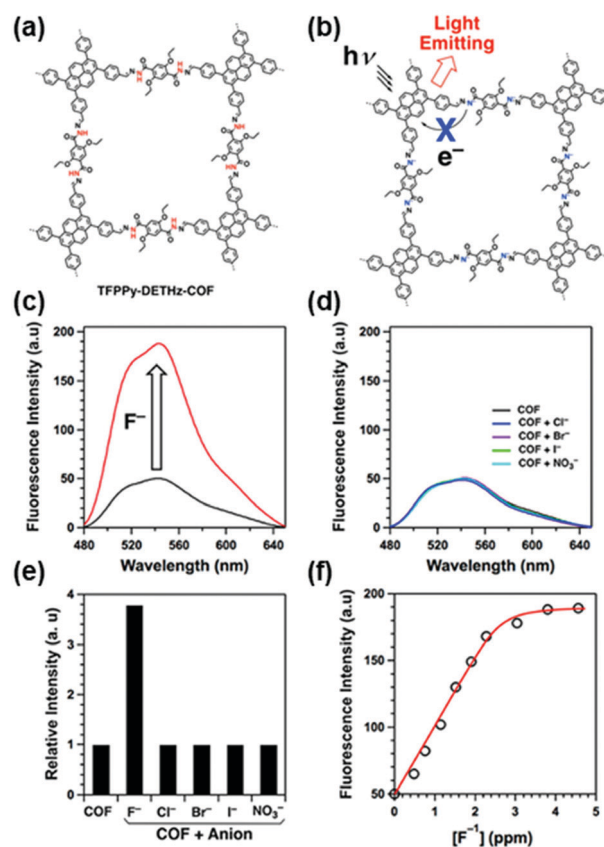


Fig. 18 (a) Chemical structure of hydrazone-linked TFPPy-DETHz-COF. (b) The fluorescence enhancement mechanism for  $F^-$  detection. Fluorescence spectral change of TFPPy-DETHz-COF upon addition of (c)  $F^-$  and (d)  $Cl^-$ ,  $Br^-$ ,  $I^-$ , and  $NO_3^-$ . (e) Relative fluorescence intensity of TFPPy-DETHz-COF upon the addition of anions. (f) The plot of fluorescence intensity versus  $[F^-]$ .<sup>237</sup> Adapted with permission from ref. 237. Copyright 2018, American Chemical Society.

play vital roles in metabolism. Detection of biomolecules is an important way to understand biochemical processes of organisms. Novel detection platforms that enable rapid, high-throughput, ultrasensitive, and specific detection of biomolecules are in great demand for the burgeoning areas of gene profiling, proteomics, drug discovery, disease diagnostics, and environmental analysis.<sup>239</sup> COFs have a few attractive features, such as high surface area, specific functional sites, and chemical stability, which have recently attracted great attention for their use in fluorescence detection of biomolecules.

So far, two different strategies have been used for the construction of COF based fluorescence detection platforms for biomolecules. In the first strategy, COFs are used as scaffolds or host matrices to support fluorescent probes (e.g., quantum dots, fluorescent metal ions) and receptors (e.g., molecularly imprinted polymers, bioreceptors) to form composite materials for detection, taking advantage of the porous structure and large surface-to-volume ratio of COFs. This strategy has been applied for the detection of DNA,<sup>240,241</sup> proteins,<sup>242</sup> natural antioxidants,<sup>243</sup> antibiotics,<sup>244</sup> and others.<sup>245–247</sup> Since this strategy relies on the modification of COFs to attain fluorescence property and specific



binding ability with analytes, we can see in the following discussions that the sensitivity and selectivity of these detection platforms highly depend on the type of auxiliary receptors. In the second strategy, prudent molecular design is used to construct COFs with intrinsic luminescence property and analyte binding capability. In this case, COFs are used as both responsive materials and transducers to yield detectable fluorescence signals that can be correlated to the identity and concentration of analytes. Recent efforts using this strategy have been devoted to the detection of DNA,<sup>248</sup> amino acids,<sup>249</sup> and small biology-related molecules.<sup>250,251</sup>

In 2017, Zhang and coworkers demonstrated a sensing platform for DNA detection by using ultrathin COF nanosheets generated from solvent-assisted liquid sonication from a structurally flexible TPA-COF (Fig. 19a and b).<sup>240</sup> The proposed detection mechanism is shown in Fig. 19c. Two hairpin DNA probes, H1 and H2, were applied, in which H1 was labeled with a fluorescent dye. Both of them can be adsorbed on the surface of TPA-COF NSs by  $\pi$ - $\pi$  stacking interactions, resulting in the fluorescence quenching of the dye. When the target DNA is present, it can specifically trigger a hybridization chain reaction (HCR) between H1 and H2 to yield long double-stranded DNA

(dsDNA), which has a very weak interaction with TPA-COF NSs. Therefore, the HCR generated long dsDNA will move away from the surface of TPA-COF NSs and result in the recovery of fluorescence of the dye, providing a quantitative detection of target DNA (Fig. 19d). Compared to the bulk TPA-COF material, TPA-COF NSs exhibited better fluorescence quenching ability (Fig. 19e), probably attributed to the increased surface area of TPA-COF NSs. The fluorescence intensity increased with the concentration of thymine (T) and exhibited a linear relationship in the range of 0–1 nM with a LOD of 20 pM (Fig. 19f), which was comparable with or even better than that of most 2D nanomaterial-based fluorescence DNA sensors.<sup>240</sup> Using a similar detection mechanism, Yan and coworkers also developed a fluorescence turn-on platform for sensing DNA using COF TpTta.<sup>241</sup> Under optimal conditions, a LOD (S/N = 3) of 3.7 nM was achieved. This TpTta COF-based sensing platform is also extendable for fluorescence turn-on detection of other biomolecules, such as ATP, by simply replacing the probe molecule.<sup>241</sup>

In addition to bioreceptors,<sup>240</sup> incorporation of molecularly imprinted polymers (MIPs) is another effective strategy to encode extrinsic material-analyte interaction onto COFs. MIPs are polymers with highly selective and effective recognition sites that are spatially and chemically complementary to the template used in the polymerization process.<sup>252,253</sup> Liu and coworkers developed a protocol for sensing bovine hemoglobin (BHB) using CdSe/ZnS quantum dot (QD)-grafted COF TpPa coupled with surface molecular imprinting technology.<sup>242</sup> TpPa was treated as a support for BHB-imprinted polymer-coated QDs whose amino group can non-covalently interact with protein targets selectively and sensitively to trigger detectable fluorescence signals. The QD-grafted COF could detect BHB concentrations over the range of 0.002–0.2 mg mL<sup>-1</sup> with a LOD of  $5.4 \times 10^{-4}$  mg mL<sup>-1</sup>. Various metal ions, such as Ca<sup>2+</sup>, Fe<sup>2+</sup>, Cu<sup>2+</sup>, Fe<sup>3+</sup>, Na<sup>+</sup>, and Zn<sup>2+</sup>, did not affect BHB detection. The strategy of adopting MIP-coated quantum dot-grafted COFs was also utilized for the detection of ferulic acid,<sup>243</sup> amino acid tyramine,<sup>245,246</sup> and a metabolite of carbadox in tissues, namely, quinoxaline-2-carboxylic acid.<sup>247</sup>

Recently, Yan *et al.* developed a lanthanide-functionalized COF-based hybrid material Eu@TpPa-1, which can act as a “turn-on” fluorescence sensor toward levofloxacin.<sup>244</sup> In the detection system, Eu<sup>3+</sup> played a bridge role to exert its characteristic emission in different concentrations of levofloxacin; TpPa-1 served as a host matrix to protect the introduced Eu<sup>3+</sup>. Eu@TpPa-1 showed strong pink-white and yellow emissions toward the high and low concentrations of levofloxacin, respectively, giving a linear range of  $10^{-6}$ – $10^{-2}$  M and a LOD at 0.2  $\mu$ M. Eu@TpPa-1 was successfully applied for sensing levofloxacin in the actual serum and urine samples with LODs at 0.2 and 0.6  $\mu$ M, respectively.

Although proven to be effective, complex fabrication processes are usually required for the modification of the COFs to execute detection in the above examples. Detection systems with concise configurations and good performance can be realized by constructing intrinsically fluorescent and responsive COFs.

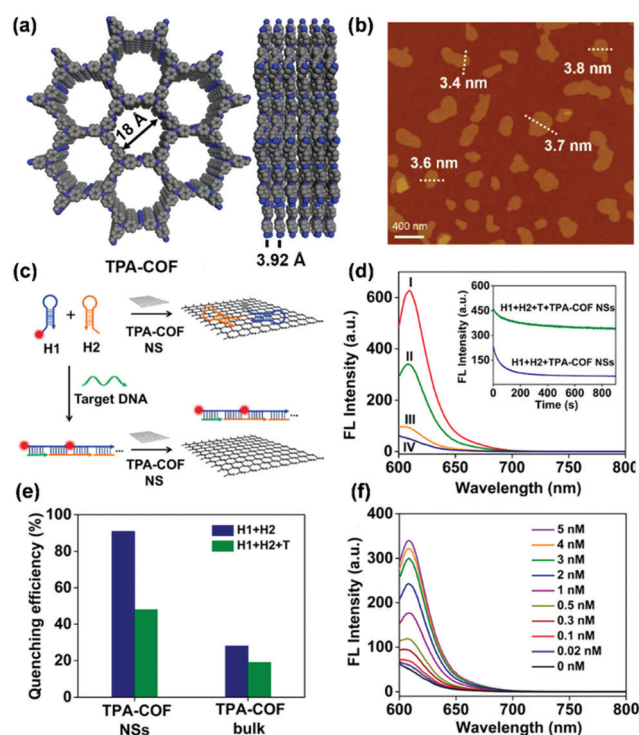


**Fig. 19** (a) Front and side view of the crystal structure model of TPA-COF. (b) AFM image of TPA-COF NSs. (c) Schematic illustration of a TPA-COF NS-based fluorescence sensor for the detection of DNA. (d) Fluorescence spectra under different experimental conditions: (I) H1 + H2; (II) H1 + H2 + T + TPA-COF NSs; (III) H1 + T + TPA-COF NSs; and (IV) H1 + H2 + TPA-COF NSs. Inset: Kinetic study on the fluorescence change of H1 + H2 and H1 + H2 + T in the presence of TPA-COF NSs. (e) Fluorescence quenching efficiency of TPA-COF NSs and bulk TPA-COF. (f) Fluorescence spectra of the proposed sensing platform in the presence of different concentrations of thymine.<sup>240</sup> Adapted with permission from ref. 240. Copyright 2017, American Chemical Society.



To introduce inherent analyte binding ability into COFs, Ajayaghosh and coworkers incorporated cationic fragment ethidium bromide into COF EB-TFP for the selective detection of double-stranded DNA (dsDNA) (EB-TFP).<sup>248</sup> In an aqueous medium, the COF EB-TFP self-exfoliated into ionic nanosheets (EB-TFP-iCONs). DNA with a long and periodic phosphate backbone can interact electrostatically with positively charged EB-TFP-iCONs, leading to the formation of hybrid EB-TFP-iCONs-DNA crystalline nanosheets (Fig. 20a and b). The EB-TFP-iCONs in the presence of dsDNA showed enhanced fluorescence at 600 nm and decreased intensity of the green emission at 510 nm (Fig. 20c). The authors hypothesized that this DNA-assisted reassembly of EB-TFP-iCONs may create a hydrophobic environment over the EB fragment of the iCONs, thereby preventing the excited-state proton transfer process to water and enhancing the emission. The addition of other phosphate-containing molecules such as monobasic and dibasic phosphates (MBP and DBP) and adenosine mono-, di-, and triphosphates (AMP, ADP, and ATP) to EB-TFP-iCONs did not result in any change in emission (Fig. 20d), indicating the selective interaction of double-stranded calf thymus DNA (ctDNA). Steady-state and time-resolved emission studies revealed that the reassembly phenomenon was highly selective for dsDNA when compared to single-stranded DNA (ssDNA), showing the potential of using EB-TFP-iCONs as a 2D fluorescent platform for the label-free detection of complementary DNA strands.<sup>248</sup>

Utilizing azine moieties as potential recognition sites, Zhao and coworkers demonstrated a signal amplification effect for amino acids and small pharmaceutical molecules using the ultrathin nanosheets of azine containing 2D COFs (NUS-30, NUS-31, and NUS-32) with AIE active tetraphenylethylene (TPE) moieties.<sup>249</sup> The azine moieties played a key role in providing

binding affinity toward amino acids by hydrogen bonds. Because of hydrogen-bond induced electron or energy transfer, a series of amino acids (L-alanine, L-threonine, and L-tryptophan) and pharmaceutical molecules (L-dopa) can trigger effective fluorescence quenching of COF nanosheets. The binding affinity of the COFs toward these amino acids increased with the total number of azine moieties within the COF structures. Compared with bulk COFs, COFs in nanosheet forms exhibited enhanced sensing sensitivity, indicating that the large exposed surface in the 2D sheets can allow sufficient contact and interaction with amino acids. The COF nanosheets were further integrated into membranes by electrospinning for detecting amino acids, though extended response time was needed compared with solution-based detection. Nevertheless, these results suggested that 2D COF nanosheets are promising material candidates for the fabrication of composite materials or devices for practical biosensing applications.<sup>249</sup>

Many biologically active molecules are chiral, including the naturally occurring amino acids, carbohydrates, and others. The discrimination of chirality from enantiomeric mixtures is of great importance because the physiological activities and biological functions are distinct for different enantiomers.<sup>254</sup> Although progress has also been made in incorporating chiral hydroxyl functionalities into COF structures for chromatographic separation of enantiomers,<sup>57,255</sup> it remains a challenge to introduce functional groups in chiral COFs for chiral optics and sensing. Through the incorporation of chiral groups into fluorescent COFs, detection of enantiomeric biomolecules can be possible. Cui and coworkers demonstrated fluorescent chiral COFs for chirality sensing of terpene flavor molecules,<sup>250</sup> which are a large and diverse class of naturally occurring organic chemicals with broad use and industrial relevance.<sup>256</sup> Two imine-linked chiral fluorescent COFs (CCOF 7 and CCOF 8) were elaborately designed and prepared by linking an enantiopure 1,1'-bi-2-naphthol (BINOL)-based linear dialdehyde with a tris(4-aminophenyl)benzene derivative or tetrakis(4-aminophenyl)ethene as building blocks (Fig. 21a and b). The COF can be readily exfoliated into ultrathin 2D nanosheets (Fig. 21c and d) and electrospun to make free-standing nanofiber membranes. In both the solution and membrane form, the fluorescence of COF nanosheets can be effectively quenched by chiral odor vapors *via* supramolecular interactions with the immobilized BINOL moieties. When nanosheets of CCOF 7 were treated with the two enantiomers of (α)-pinene, the rate of quenching caused by the (–)-enantiomer was faster than that with the (+)-enantiomer with a quenching ratio [QR =  $K_{sv}(-)/K_{sv}(+)$ ] of 3.41, showing enantioselectivity in the fluorescence recognition (Fig. 21e). Control experiments showed that the bulk sample of CCOF 7 exhibited much lower enantioselective performance than 7-NS (Fig. 21f). This feature may be attributed to the fact that the NSs have a more exposed external surface and accessible active binding sites, allowing sufficient contact and interaction with the analyte.<sup>162,240</sup> Similar selectivity was also observed using the nanofiber membrane of CCOF 7 and for other terpenes, including limonene, fenchone, terpinen-4-ol, and carvone, with the QR values ranging from 1.20 to 3.41 (Fig. 21g and h).

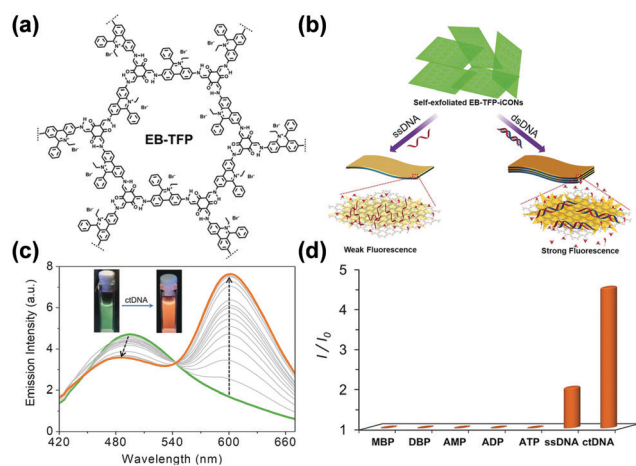


**Fig. 20** (a) Structure of EB-TFP-iCOF. (b) Schematic of EB-TFP-iCONs as a fluorescent platform for label-free detection of dsDNA. (c) Emission ( $\lambda_{\text{ex}} = 350$  nm) spectral changes of EB-TFP-iCONs upon the addition of ctDNA (0–32  $\mu\text{M}$ ). Inset: Corresponding changes in emission color upon illuminating with 365 nm UV light. (d) Selective fluorescence enhancement ( $\lambda_{\text{em}} = 600$  nm) of EB-TFP-iCONs upon adding MBP, DBP, AMP, ADP, ATP, ssDNA (20-mer), and ctDNA.<sup>248</sup> Adapted with permission from ref. 248. Copyright 2018, Wiley-VCH.





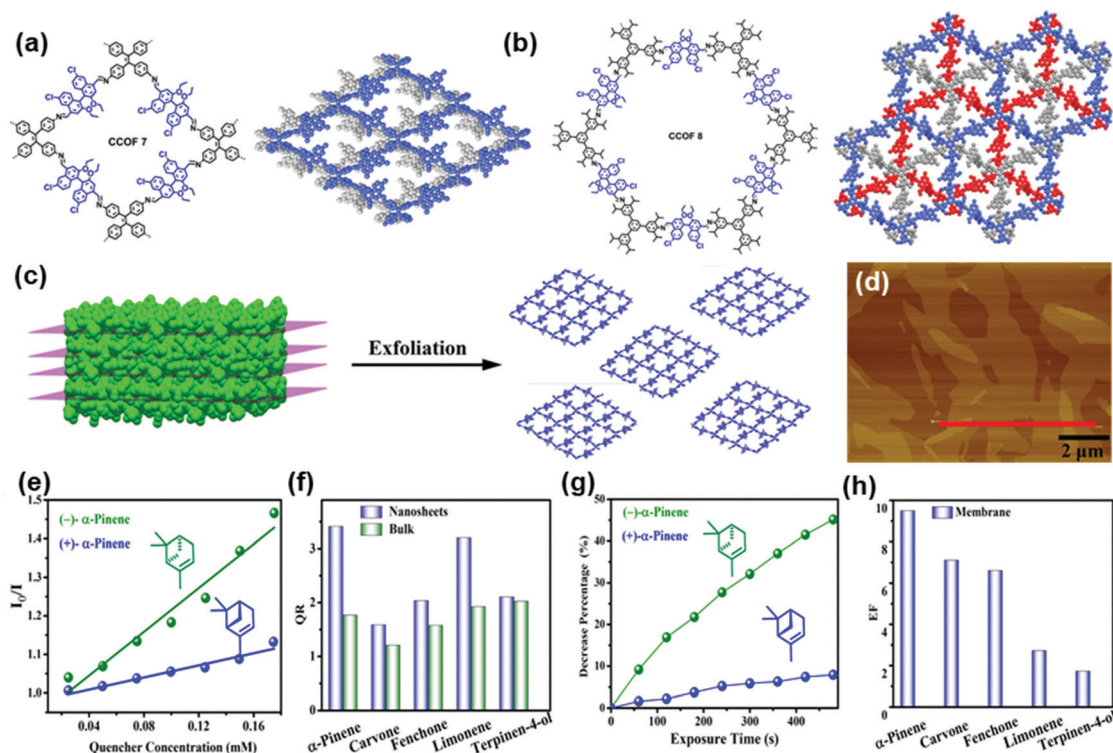


**Fig. 21** (a) Chemical structure and refined 2D crystal model of CCOF 7. (b) Chemical structure and refined 2D crystal model of CCOF 8. (c) Schematic diagram of exfoliation of COFs into ultrathin 2D NSs. (d) AFM image of the exfoliated nanosheet of CCOF-7. (e) Stern–Völmer plots of CCOF7-NS upon titration of  $\alpha$ -pinene in MeCN. (f) Enantioselective quenching ratio for several terpenes. (g) Decrease of fluorescence of the membrane made of CCOF7-NS upon exposure to  $\alpha$ -pinene. (h) Enantioselective fluorescence decrease ratio of the membrane for several vapors.<sup>250</sup> Adapted with permission from ref. 250. Copyright 2019, American Chemical Society.

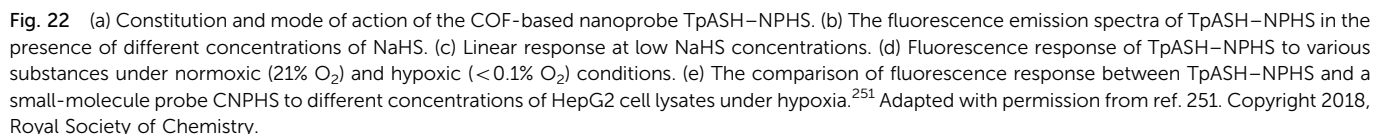
Compared to the BINOL-based homogeneous and membrane systems, the COF nanosheets exhibited greatly enhanced sensitivity and enantioselectivity owing to the confinement effect and the conformational rigidity of the sensing BINOL groups in the framework.<sup>250</sup> Integrating chiral auxiliary inside the open channels of COFs capable of amplifying chiral discrimination of analytes provided a feasible strategy toward the rational design of porous materials for chiral sensing of other biologically important molecules.

The fluorescence property of COFs has also been utilized in the detection of intracellular hydrogen sulfide. Small-molecule fluorescent probes have been widely applied for the detection and imaging of various biological targets; however, the bio-sensing performance of a small-molecule fluorescent probe can be susceptible to the complex biological environment. For example, intricate intracellular enzymes may affect the selectivity and sensitivity of the designed probe.<sup>257</sup> Zhang and coworkers envisaged that COFs can circumvent the problems associated with the interference by enzymes as encountered by small-molecule fluorescent probes, considering that the nanoscale pores of COFs can filter biomacromolecules (Fig. 22a).<sup>251</sup> To realize this concept, the authors designed a hybrid fluorescent probe TpASH-NPHS comprised of an imine-linked COF TpASH and a two-photon fluorescent probe 4-amino-1,8-naphthalimide derivative (NPHS) anchored to the COF through alkylation of the phenolic hydroxyl

group of TpASH. The azide units on NPHS can be reduced to amino groups in the presence of  $H_2S$ , which will enhance the fluorescence emission of NPHS. The hybrid fluorescent probe TpASH-NPHS was able to detect the concentration of  $NaHS$  in the range of 0–20  $\mu M$  with a LOD of 0.11  $\mu M$  (Fig. 22b and c). The fluorescence of TpASH-NPHS was insensitive to various interferents, including common anions, biothiols, cysteine, homocysteine, and reactive oxygen species under normoxic and hypoxic conditions (Fig. 22d). The fluorescence emission of TpASH-NPHS in the lysates of HepG2 cells was not affected but the small molecule fluorescent probe CNPHS showed an emission increase (Fig. 22e), indicating that this COF nanoprobe was able to abate the biomacromolecular interference. Because of the interference-resistant ability, TpASH-NPHS was used to image endogenous  $H_2S$  and to monitor the expression levels of the  $H_2S$ -generating enzyme cystathionine  $\gamma$ -lyase in a cirrhotic liver model.<sup>251</sup> This TpASH-NPHS system provided an example for the exploitation of COFs for interference-resistant and selective biosensing by fully utilizing their predesigned topology and pore structure.

The use of COFs for fluorescence-based chemical detection is a rapidly developing field. In recent years, COFs as key components in fluorescence detection have been successfully applied for the analysis of various volatiles, gases, ions, and biological analytes (Table 3). Although encouraging developments have been made, there are still a few challenges remaining.





nanosheets.<sup>258</sup> Secondly, in the current sensing platforms, the fluorescence turn-off mechanism based on metal–ligand coordination or donor–acceptor energy and charge transfer is much more frequently used than the fluorescence turn-on mechanism.<sup>175,176,190,191</sup> Compared to fluorescence turn-on sensors, fluorescence turn-off sensors can suffer from the limitations of higher background fluorescence and lower sensitivity, raising a great demand for developing highly luminescent COFs.<sup>259,260</sup> Only a few turn-on types of platforms have been developed for the detection of ions<sup>228,237</sup> and biology-related molecules,<sup>240,241,244,251</sup> and detection based on the switching of intrinsic fluorescence of COFs remains rare.<sup>228,237</sup> The challenges

Table 3 Summary of fluorescence-based detection using COFs

Analyte(s)	Type of response	COF	Detection architecture	LOD	Detection range	Other detection parameters	Ref.
TNP	Turn-off	Py-Azine	Py-Azine suspension	N/A	0–70 ppm	In acetonitrile; selectivity over DNP, DNT, NP, and NT	160
TNP	Turn-off	3D-Py-COF	3D-Py-COF suspension	N/A	0–20 ppm	In DMF	177
TNP	Turn-off	SNW-1	SNW-1 suspension	0.05 $\mu\text{M}$	0.2–52.4 $\mu\text{M}$	In 10% THF aqueous solution; selectivity over NB, 4-NT, DNT, TNT, tetryl, NP, DMF, DMSO, ethanol, acetone, acetonitrile, and benzene	183
TNP	Turn-off	Tf <sub>2</sub> BDH	Tf <sub>2</sub> BDH-CONs suspension	N/A	$0.5\text{--}4 \times 10^{-5}$ M	In isopropyl alcohol; selectivity over TNT, DNP, DNT and NP	190
TNP	Turn-on	Tf <sub>2</sub> BDH	Solid state Tf <sub>2</sub> BDH-CONs	$10^{-3}$ M	$5.4 \times 10^{-3}$ M	In gas phase; selectivity over TNT, DNP, DNT and NP	190
TNP	Turn-off	PI-COF	PI-CONs dispersion	0.25 $\mu\text{M}$	0.5–21 $\mu\text{M}$	In ethanol; selectivity over NB, NT, DNT, TNT, HQ, AN, PPD, NP, and DNP	191
TNP	Turn-off	TRIPTA	TRIPTA suspension	N/A	$5.2 \times 10^{-8}\text{--}5.46 \times 10^{-7}$ M	In acetonitrile	192
TNP	Turn-off	TAPB-TFPB	TAPB-TFPB dispersion	N/A	0–13 ppm	In acetonitrile; selectivity over DNT, <i>p</i> -DNB and <i>m</i> DNB	193
TNP	Turn-off	<sup>i</sup> PrTAPB-TFPB	<sup>i</sup> PrTAPB-TFPB dispersion	N/A	0–22 ppm	In acetonitrile; selectivity over DNT, <i>p</i> -DNB and <i>m</i> DNB	193
TNP	Turn-off	TAPB-TFP	TAPB-TFP dispersion	N/A	0–15 ppm	In acetonitrile; selectivity over DNT, <i>p</i> -DNB and <i>m</i> DNB	193
TNP	Turn-off	<sup>i</sup> PrTAPB-TFP	<sup>i</sup> PrTAPB-TFP dispersion	N/A	0–23 ppm	In acetonitrile; selectivity over DNT, <i>p</i> -DNB and <i>m</i> DNB	193
TNP	Turn-off	<b>1</b>	<b>1</b> dispersion	N/A	2–25 $\mu\text{M}$	In water; selectivity over 4-NT, 2-NT, 2,6-DNT, NB, 2,4-DNT, and DNB	194
TNP	Turn-off	COF-BABD-DB	COF-BABD-DB suspension	N/A	1–12.5 $\mu\text{M}$	In acetonitrile; selectivity over DNP, NP, NT, NB, DNB, and DNT	200
TNP	Turn-off	COFBABD-BZ	COFBABD-BZ suspension	N/A	1–12.5 $\mu\text{M}$	In acetonitrile; selectivity over DNP, DNB, NP, NT, NB, and DNT	200
TNP	Turn-off	TPE-Ph	TPE-Ph dispersion	N/A	1–25 ppm	In acetone; selectivity over DNP, DNT, NT, and NP	201
TNP	Turn-off	<sup>i</sup> PrTAPB-Azo-COP	<sup>i</sup> PrTAPB-Azo-COP dispersion	N/A	0–13 ppm	In acetonitrile; selectivity over DNT and <i>m</i> -DNB	261
DNT	Turn-off	PAF-15	PAF-15 dispersion	N/A	1.5–150 ppm	In CHCl <sub>3</sub> ; selectivity over benzene, toluene, chlorobenzene, bromobenzene, phenol, and aniline	188
TNT	Turn-off	PAF-15	PAF-15 dispersion	N/A	1.5–150 ppm	In CHCl <sub>3</sub> ; selectivity over benzene, toluene, chlorobenzene, bromobenzene, phenol, and aniline	188
NB	Turn-off	PAF-15	PAF-15 dispersion	N/A	1.5–150 ppm	In CHCl <sub>3</sub> ; benzene, toluene, chlorobenzene, bromobenzene, phenol, and aniline	188
DNP	Turn-off	TRIPTA	TRIPTA dispersion	N/A	$5.2 \times 10^{-8}\text{--}5.46 \times 10^{-7}$ M	In acetonitrile	192
DNT	Turn-off	TRIPTA	TRIPTA dispersion	N/A	$5.2 \times 10^{-8}\text{--}5.46 \times 10^{-7}$ M	In acetonitrile	192
NP	Turn-off	TRIPTA	TRIPTA dispersion	N/A	$5.2 \times 10^{-8}\text{--}5.46 \times 10^{-7}$ M	In acetonitrile	192
<i>p</i> -DNB	Turn-off	<sup>i</sup> PrTAPB-Azo-COP	<sup>i</sup> PrTAPB-Azo-COP dispersion	N/A	0–329 ppm	In acetonitrile; selectivity over DNT and <i>m</i> -DNB	261
TATP	Turn-off	<b>3</b> <sup>PD</sup>	<b>3</b> <sup>PD</sup> dispersion	~1 $\mu\text{M}$	5–100 $\mu\text{M}$	In DCM	262







Table 3 (continued)

Analyte(s)	Type of response	COF	Detection architecture	LOD	Detection range	Other detection parameters	Ref.
Janus Green	Turn-off	IMDEA-COF-1	IMDEA-COF-1 suspension	N/A	10–40 $\mu\text{M}$	In aqueous solution; selectivity over methylene blue, malachite green, bromophenol blue, crystal violet, and thionin	196
H <sub>2</sub> O	Ratiometric	TzDa	TzDa dispersion	0.085, 0.022, 0.026, 0.006, and 0.034 wt%	1.1–7.7, 0.1–5.1, 0.5–5.1, 0.6–3.2, and 0.4–2.5 wt%	In IPA, acetone, THF, EtOAc, and ethanol	206
NH <sub>3</sub>	Turn-off	TPE-Ph	TPE-Ph dispersion	<0.3 ppm	0.3–9.7 ppm	In toluene	175
NH <sub>3</sub>	Turn-on	COP-1	COP-1 dispersion	0.059% (v/v)	1.16–5.80% (v/v)	In gas phase; selectivity over benzene, methylbenzene, dimethylbenzene and trichloromethane; reversible	137
HCl	Turn-off	COP-1	COP-1 solid film	0.011% (v/v)	1.16–5.80% (v/v)	In gas phase; selectivity over CO <sub>2</sub> , SO <sub>2</sub> , H <sub>2</sub> S and Cl <sub>2</sub> ; reversible	137
HCl	N/A	COF-ETBA-DAB	COF-ETBA-DAB dispersion	<0.13 mM	0.13–91 mM	In 1,4-dioxane; response time <1 s	141
H <sub>2</sub> S	Turn-on	TPASH	TPASH-NPHS dispersion	0.12 $\mu\text{M}$	1 $\mu\text{M}$ –5 mM	In PBS, pH = 7.4; selectivity over Cl <sup>−</sup> , Br <sup>−</sup> , I <sup>−</sup> , HCO <sub>3</sub> <sup>−</sup> , HPO <sub>4</sub> <sup>2−</sup> , OAc <sup>−</sup> , NO <sub>2</sub> <sup>−</sup> , SO <sub>4</sub> <sup>2−</sup> , SO <sub>3</sub> <sup>2−</sup> , HSO <sub>3</sub> <sup>−</sup> , S <sub>2</sub> O <sub>3</sub> <sup>2−</sup> , S <sub>2</sub> O <sub>5</sub> <sup>2−</sup> , GSH, Cys, Hcy, ClO <sup>−</sup> and H <sub>2</sub> O <sub>2</sub> ; imaging in live cells, tumor tissues, cirrhotic liver model	251
Cu <sup>3+</sup>	Turn-off	PI	PI nanosheet suspension	N/A	$1 \times 10^{-4}$ – $1 \times 10^{-2}$ M	In water; K <sup>+</sup> , Ca <sup>2+</sup> , Cd <sup>2+</sup> , Pb <sup>2+</sup> , Mn <sup>2+</sup>	213
Au <sup>+</sup>	Turn-off	TTB-COF	TTB-COF dispersion	0.87 $\mu\text{M}$	1.0–10.0 $\mu\text{M}$	Hg <sup>2+</sup> , Mg <sup>2+</sup> , Co <sup>2+</sup> , Cu <sup>2+</sup> , and Zn <sup>2+</sup>	215
Cu <sup>2+</sup>	Turn-off	COF-JLU3	COF-JLU3 dispersion	0.31 $\mu\text{M}$	0–200 $\mu\text{M}$	In acetonitrile; Fe <sup>3+</sup> , Ni <sup>2+</sup> , Co <sup>2+</sup> , Zn <sup>2+</sup> , and Cd <sup>2+</sup>	215
Cu <sup>2+</sup>	Turn-off	sp <sup>2</sup> c-COF	sp <sup>2</sup> c-COF dispersion	88 ppb	$0-0.3 \times 10^{-4}$ M	In THF; selectivity over Li <sup>+</sup> , Na <sup>+</sup> , K <sup>+</sup> , Mg <sup>2+</sup> , Ca <sup>2+</sup> , Ba <sup>2+</sup> , Zn <sup>2+</sup> , Cd <sup>2+</sup> , Ni <sup>2+</sup> , Pb <sup>2+</sup> , Co <sup>2+</sup> , Ag <sup>+</sup> , Fe <sup>3+</sup> and Al <sup>3+</sup>	176
Cu <sup>2+</sup>	Turn-off	N/A	Dispersion of carbon quantum dot scaffolded COFs	0.50 nM; 2.4 nM	0.0010–10.0 $\mu\text{M}$ ; 0.0032–32.0 $\mu\text{M}$	pH = 7.0; selectivity over Pb <sup>2+</sup> , Mg <sup>2+</sup> , Hg <sup>2+</sup> , Zn <sup>2+</sup> , Fe <sup>3+</sup> , Fe <sup>2+</sup> , Co <sup>2+</sup> , Cd <sup>2+</sup> , Cr <sup>3+</sup> , Ni <sup>2+</sup> , K <sup>+</sup> , Ca <sup>2+</sup> , Na <sup>+</sup> , Gly, Cys, and HSA; blood, wastewater	222
Fe <sup>3+</sup>	Turn-off	DhaTab	DhaTab dispersion	0.12 $\mu\text{M}$	5–500 $\mu\text{M}$	In DMF/H <sub>2</sub> O (9:1, v/v); selectivity over Na <sup>+</sup> , Mg <sup>2+</sup> , Al <sup>3+</sup> , K <sup>+</sup> , Ca <sup>2+</sup> , Cu <sup>2+</sup> , Zn <sup>2+</sup> , Pb <sup>2+</sup> , Ag <sup>+</sup> , and Cd <sup>2+</sup>	184
Fe <sup>3+</sup>	Turn-off	PI-COF 201	PI-COF 201 suspension	0.13 $\mu\text{M}$	0–1 mM	In DMF; selectivity over Na <sup>+</sup> , K <sup>+</sup> , Co <sup>2+</sup> , Pb <sup>2+</sup> , Sr <sup>2+</sup> , Mg <sup>2+</sup> , Ca <sup>2+</sup> , Ag <sup>+</sup> , La <sup>3+</sup> , Ce <sup>3+</sup> , and Cu <sup>2+</sup>	224
Fe <sup>3+</sup>	Turn-off	PI-COF 202	PI-COF 202 suspension	0.13 $\mu\text{M}$	0–1 mM	In DMF; selectivity over Na <sup>+</sup> , K <sup>+</sup> , Co <sup>2+</sup> , Pb <sup>2+</sup> , Sr <sup>2+</sup> , Mg <sup>2+</sup> , Ca <sup>2+</sup> , Ag <sup>+</sup> , La <sup>3+</sup> , Ce <sup>3+</sup> , and Cu <sup>2+</sup>	224
Fe <sup>3+</sup>	Turn-off	TaDAP	TaDAP dispersion	18 mM	0.02–0.86 mM	In DMF/H <sub>2</sub> O (9:1, v/v); selectivity over Na <sup>+</sup> , Ag <sup>+</sup> , K <sup>+</sup> , Ca <sup>2+</sup> , Cu <sup>2+</sup> , Co <sup>2+</sup> , Mn <sup>2+</sup> , Ba <sup>2+</sup> , Co <sup>2+</sup> , Zn <sup>2+</sup> , Pb <sup>2+</sup> , Mg <sup>2+</sup> , Cr <sup>3+</sup> , and Al <sup>3+</sup>	225
Fe <sup>3+</sup>	Turn-off	Bth-Dma	Bth-Dma dispersion	0.17 $\mu\text{M}$	0.5–100 $\mu\text{M}$	In water; selectivity over Na <sup>+</sup> , K <sup>+</sup> , Mg <sup>2+</sup> , Ba <sup>2+</sup> , Mn <sup>2+</sup> , Ca <sup>2+</sup> , Gd <sup>3+</sup> , Zn <sup>2+</sup> , Ni <sup>2+</sup> , Co <sup>2+</sup> , La <sup>3+</sup> , Nd <sup>3+</sup> , Fe <sup>2+</sup> , or Cu <sup>2+</sup>	226
Al <sup>3+</sup>	Turn-on	Bpy-COF	Bpy-COF NS dispersion	N/A	0–400 $\mu\text{M}$	In water; selectivity over Zn <sup>2+</sup> , Cd <sup>2+</sup> , Mn <sup>2+</sup> , Cr <sup>3+</sup> , Pb <sup>2+</sup> , Mg <sup>2+</sup> , Ag <sup>+</sup> , Ba <sup>2+</sup> , Ca <sup>2+</sup> , Na <sup>+</sup> , K <sup>+</sup> , Co <sup>2+</sup> , Fe <sup>3+</sup> , Li <sup>+</sup> , Hg <sup>2+</sup> , Ni <sup>2+</sup> , and Cu <sup>2+</sup>	228

Table 3 (continued)

Analyte(s)	Type of response	COF	Detection architecture	LOD	Detection range	Other detection parameters	Ref.
UO <sub>2</sub> <sup>2+</sup>	Turn-off	TPPT-BTAN-AO	TPPT-BTAN-AO dispersion	6.7 nM	0–20 µM	In H <sub>2</sub> O; selectivity over Co <sup>2+</sup> , Ca <sup>2+</sup> , Cd <sup>2+</sup> , Cs <sup>+</sup> , Cr <sup>3+</sup> , Mn <sup>2+</sup> , Fe <sup>3+</sup> , Cu <sup>2+</sup> , Ni <sup>2+</sup> , Al <sup>3+</sup> , Zn <sup>2+</sup> , Mg <sup>2+</sup> , Pd <sup>2+</sup> , Ba <sup>2+</sup> , Ce <sup>3+</sup> , Nd <sup>3+</sup> , Sm <sup>3+</sup> , and La <sup>3+</sup>	229
UO <sub>2</sub> <sup>2+</sup>	Turn-off	NS-COF	NS-COF NS dispersion	N/A	0.8–36 µM	In DMF; selectivity over Nd <sup>3+</sup> , Sm <sup>3+</sup> , La <sup>3+</sup> , Ce <sup>3+</sup> , Mn <sup>2+</sup> , Sr <sup>2+</sup> , Ba <sup>2+</sup> , Ni <sup>2+</sup> , Co <sup>2+</sup> , and Zn <sup>2+</sup>	264
F <sup>−</sup>	Turn-on	TPPPY-DETHz-COF	TPPPY-DETHz-COF dispersion	N/A	0–4 ppm	In THF; selectivity over Cl <sup>−</sup> , Br <sup>−</sup> , I <sup>−</sup> , and NO <sub>3</sub> <sup>−</sup>	237
H <sup>+</sup>	Turn-on	COF-JLU4	COF-JLU4 dispersion	N/A	pH 0.9–1.3	In aqueous solution; reversible	234
H <sup>+</sup>	Turn-off	COF-HQ	COF-HQ suspension	N/A	pH 1–5	In aqueous solution	235
DNA	Turn-on	TPA-COF	Suspension of TPA-COF NSs/H1 + H2	20 pM	0.02–5 nm	50 mM Na <sub>2</sub> HPO <sub>4</sub> and 0.75 M NaCl; pH = 7.4; selectivity over T, single-base mismatch DNA, random DNA	240
DNA	Turn-on	TpTta	FAM-labeled prob/TpTta suspension	3.7 nm	10–100 nm	10 mM Tris-HCl, 50 mM NaCl, 10 mM MgCl <sub>2</sub> , pH = 7.4	241
DNA	Ratiometric	EB-TFP	EB-TFP suspension	N/A	0–32 µM	20 mM phosphate buffer, 2 mM NaCl, pH = 7.2; selectivity over MBP, DBP, AMP, ADP, ATP, and ssDNA	248
ATP	Turn-on	TpTta	FAM-labeled ATP aptamer/TpTta suspension	N/A	25–200 mM	20 mM Tris-HCl, 140 mM NaCl, 5 mM KCl, pH = 7.4	241
BHb	Turn-off	TpPa	CdSe/ZnS QDs/TpPa dispersion	5.4 × 10 <sup>−4</sup> mg mL <sup>−1</sup>	0.002–0.2 mg mL <sup>−1</sup>	PBS buffer, pH = 6.7; Ca <sup>2+</sup> , Fe <sup>2+</sup> , Cu <sup>2+</sup> , Fe <sup>3+</sup> , Na <sup>+</sup> , Zn <sup>2+</sup> , K <sup>+</sup> , and Mg <sup>2+</sup>	242
Ferulic acid	Turn-off	TpPa	QDs-grafted TpPa/MIP dispersion	5 µg kg <sup>−1</sup>	0.03 to 60 mg kg <sup>−1</sup>	In ethanol; selectivity over cinnamic acid, syringic acid, and caffeic acid	243
Levofloxacin	Turn-on	TpPa-1	Eu@TpPa-1 suspension	0.2 µM	10 <sup>−6</sup> –10 <sup>−2</sup> M	In water; selectivity over urea, L-proline, NaHCO <sub>3</sub> , NaCl, KCl, glucose, MgCl <sub>2</sub> , CaCl <sub>2</sub> , creatinine, Na <sub>2</sub> SO <sub>4</sub> , creatine, NH <sub>4</sub> Cl; serum, urine	244
Tyramine	Turn-off	TpPa	CdSe-ZnS QD grafted TpPa/MIOP dispersion	7.0 µg kg <sup>−1</sup>	35–35 000 µg kg <sup>−1</sup>	In ethanol; selectivity over HIS and PEA; meat sample	245
Tryptamine	Turn-off	TpPa	CNDs-embedded TpPa/MIPs dispersion	7.0 µg kg <sup>−1</sup>	0.025–0.4 mg kg <sup>−1</sup>	In ethanol; selectivity over HIS	246
Quinoxaline-2-carboxylic acid	Turn-off	TpPa	CdSe-ZnS QD grafted TpPa/MIPs dispersion	0.85 µmol L <sup>−1</sup>	1–50 µmol L <sup>−1</sup>	In acetonitrile/methanol, PBS, pH = 7.5; CBX, MEQ, MQCA, and OLA; meat samples	247
L-Phenylalanine	Turn-off	NUS-30	NUS-30 NS dispersion	N/A	N/A	In acetonitrile	249
L-Dopa	Turn-off	NUS-30	NUS-30 NSs/PVDF membrane	N/A	N/A	N/A	249
(−)-α-Pinene	Turn-off	CCOF 7	CCOF 7 NS suspension	N/A	10–170 µM	In acetonitrile; selectivity over (+)-α-pinene	250
(−)-α-Pinene	Turn-off	CCOF 7	CCOF 7@PVDF	N/A	0–150 µM	In acetonitrile; selectivity over (+)-α-pinene	250
4-Ethylguaiacol	Turn-off	TAPA	QD-grafted COFs@MIPs dispersion	17 ng mL <sup>−1</sup>	0.025–1 µg mL <sup>−1</sup>	In ethanol; selectivity over maltol, 4-vinylguaiacol, and <i>p</i> -cresol; response time 15 min; wine sample	265
•OH	Turn-off	COF-TpMA	COF-TpMA suspension	N/A	0.1–10 µg mL <sup>−1</sup>	In DMSO/PBS buffer (1:9, v/v, 20 mM), pH = 7.4; response time 2 min; cells	207



for developing fluorescence turn-on type detection systems may lie in the limited understanding and control of the fluorescence emission mechanism of COFs under the participation of the analyte molecules, especially in a complex detection environment. Learning from the well-established small molecule-based fluorescence detection systems and introducing them into framework materials may be one of the feasible solutions. Thirdly, although satisfactory selectivity for certain analytes has been demonstrated, the selectivity of most COF-based sensing strategies is limited due to the lack of a specific recognition group. Strategic molecular design is needed to install sophisticated recognition elements in COFs. Post-synthetic modification strategies have played a key role in the development and construction of functionalized COFs, which can endow COFs with effective and selective active sites for analyte binding. However, current post-synthetic modifications of COFs are limited to channel wall functionalization. Precise control of the quantity and distribution of functional groups within COFs is still challenging. Therefore, directly embedding the active sites in the building blocks for the reticular synthesis can be another alternative, though the compatibility between active sites and reticular reactions for COF synthesis needs to be carefully considered.

## 2.3 Detection based on electrically transduced methods

**2.3.1 Basics about electrically transduced detection.** As discussed in Sections 2.1 and 2.2, detection based on chromism and luminescence relies on the change of optical properties of the material to acquire information of analytes. In contrast to chromism and luminescence-based detection, electrically transduced detection uses the change of electrical properties (such as conductivity, work function, or electrical permittivity) of the material triggered by material–analyte interactions. Various electronic components, generally including resistor, diode, field-effect transistor, capacitor, and electrochemical configuration, can be adopted for the measurement of the magnitude, frequency, or phase changes in the resistance, current, voltage/electrical potential, and capacitance to obtain information regarding the material–analyte binding event. In terms of advantages, electrically transduced detection features simplicity and compatibility with standard electronic technologies and can produce signals that can be efficiently acquired, processed, stored, and analyzed. The use of a material for electrically transduced detection requires the consideration of its ability to selectively interact with the target analyte and to consequently respond to this interaction as changes in electrical properties. Although multiple configurations are potentially available, the use of COFs in electrically transduced detection so far mainly centers on two types of configurations, electrochemical and chemiresistive detection.

**Electrochemical detection technique.** Electrochemical detection is one of the largest groups of analytical methods that have been widely applied for chemical detection. It is recognized to be a promising technology for specific and sensitive detection of various types of analytes in the solution phase due to its capability for fast, simple, direct, and sensitive analysis

even in a complex sample matrix and due to the great potential in device miniaturization, integration, and commercialization.<sup>266</sup> In electrochemical detection, the responsive material can interact with the analyte of interest through chemical or biological interaction, such that the charge transport characteristic of the tested system can be transduced into a measurable electrical signal in the form of potential, current, charge accumulation, or conductance/impedance change. Based on the way of acquiring and monitoring electrical signals, analytical techniques of electrochemistry can be further divided into three main categories, namely, potentiometry, amperometry, and conductometry, which measure the potential, current, and conductance/resistance of the detection system, respectively.

In potentiometric measurements, the difference in the electrical potential of the working electrodes relative to the potential of a reference electrode is measured, usually by using a two-electrode galvanic cell under ideally zero current conditions. A local equilibrium is built at the electrode–sample interface as a result of analyte partitioning between the working electrode and the sample solution. The measured potential is used to determine the analytical quantity of interest in the solution. This potential can be described by the Nernst equation, which reveals a linear dependence of the response,  $E$ , on the logarithm of a function of the activity of the ion in solution.

$$E = E^\circ + \frac{RT}{nF} \ln[a_i]$$

In the equation,  $E$  is the potential ( $I$ ) electrical potential between the working and reference electrode,  $E^\circ$  is the standard potential under standard conditions (273.15 K and 100 kPa),  $R$  is the gas constant,  $F$  is the Faraday constant,  $n$  is the charge number of the primary ion, and  $a_i$  is the activity of the principal ion. When more than one relevant species are present, the overall signal would be from the contribution of both the analyte of interest and interfering species. To ensure selectivity, a membrane material that is selective to one species is required for the modification of the working electrode, for example, an ionophore that is selective to a specific ion of interest.

In amperometric detection, the current is measured over time with a fixed potential in a three-electrode set-up comprising a working electrode, counter electrode, and reference electrode. During amperometric detection, electrochemical reactions of analytes occur at the electrode surface. The essential operational feature of amperometric detection is the electron transfer between the working electrode and the analyte. When the working electrode is placed in a stirred solution (batch mode) or a flowing stream (continuous mode), and with the working potential fixed at a value corresponding to the limiting current plateau region, the current,  $i_L$ , is a function of the concentration  $c$  of one redox species:

$$i_L = \frac{nFADc}{d}$$

where  $n$  is the number of electrons transferred,  $A$  is the surface area,  $D$  is the diffusion coefficient,  $F$  is the Faraday constant, and  $d$  is the thickness of the diffusive layer. The analyte of





interest that is electroactive at the applied potential is suitable for amperometric detection. Interference of the non-electroactive compounds can be avoided. Using an array of sensors working at different potentials, it is also possible to differentiate several electroactive compounds, since at low positive/negative potentials, only strong reducing/oxidizing compounds may be detected. However, pH, ionic strength, and electrochemical activity of the solvent and the electrolyte, as well as the presence of electroactive impurities (such as dissolved oxygen or trace metals) may affect the signal in the detection.

Voltammetric detection shares a similar set-up with amperometric detection. The difference is that the potential applied in voltammetric detection is continuously changed following a well-defined ramp. Typical potential ramps can be linear, and the corresponding technique is called linear sweep voltammetry (LSV). Alternatively, if the potential is cycled between two limiting values with a defined rate, this technique is called cyclic voltammetry (CV). The potential also can be pulsed with a certain amplitude and frequency, like in the case of differential pulse voltammetry (DPV) or square wave voltammetry (SWV). All these techniques are characterized by a signal that depends on the capability of the analytes to be either oxidized and/or reduced at the working electrode. The position and intensity of the corresponding current-potential wave can be respectively used as a fingerprint for identifying an analyte and as a reference signal for quantifying its concentration.

Conductometric detection is carried out by measuring the impedance or conductance change of a thin film or bulk solution in the presence of analyte species. The most used conductometric technique is electrochemical impedance spectroscopy (EIS), which has been used to identify and separate different contributions to the electric and dielectric responses of a material. Similar to voltammetric/amperometric techniques, EIS predominantly utilizes a three-electrode configuration for electroanalytical measurements. A sinusoidal potential excitation with a small magnitude is imposed.<sup>267</sup> The current response is a sinusoidal wave with the same frequency of perturbation potential, but with different amplitude and phase.<sup>268,269</sup> The magnitude of the recorded phase shift depends on the nature of the electrolyte, diffusion process, electrode kinetics, and chemical reactions that take place in the electrochemical cell.<sup>10</sup> For instance, a change in the impedance of the electrochemical cell can be used to follow reactions that produce a change in the number, charge, or mobility of analytes; a change in capacitance is indicative of the change in the dielectric constant of the recognition layer at the electrode surface due to the presence of analytes.<sup>270</sup>

**Chemiresistive detection.** Chemiresistive detection is one of the widely applied methods for electrically transduced sensing of gaseous and volatile analytes. A chemiresistive device, called chemiresistor, usually consists of two electrodes connected with a chemiresistive material deposited onto an insulating support. With the aid of amperometric detection, by monitoring the current flowing through the device under a fixed potential, the conductivity/resistance change of responsive materials upon their interactions with analyte molecules is analyzed. Compared with

optical detection, chemiresistive detection offers the advantages of simplicity, compatibility with conventional direct current circuits, low cost, and the ease of high precision measurement. Materials with suitable conductivity are required to ensure detectable electrical signals for the implementation of chemiresistive detection. Various conductive materials, like graphene,<sup>34,117</sup> metal oxides,<sup>118,119,271</sup> and carbon nanotubes,<sup>116</sup> have been extensively applied for chemiresistive detection.

*Potential advantages of COFs for electrically transduced chemical detection.* Considering that there are multiple analytical configurations available, a material can be utilized in different ways for electrically transduced detection. Firstly, for selective recognition of a species of interest, a recognition element is required for the development of electrochemical detection. For example, in potentiometric detection, the perm-selective membrane is a key component that selectively binds to the target ion. In amperometric or voltammetric detection, the recognition element should selectively allow diffusion of the electrochemically active species to the electrode surface. Secondly, materials with good electron transport properties are critically important for their utilization as electrode materials for electrically transduced detection. The charge transfer interactions at the interface between an electrode and analytes in a liquid or gas phase determine the intensity of electrical signals being transduced. Sufficient electrical conductance is needed for the recognition layer of the working electrode in amperometric/voltammetric and chemiresistive detection to enhance the electron transfer.

COFs have porous and stable structures, highly accessible and programmable active sites, and tunable electrical properties. This multifunctionality makes COFs promising and attractive materials in electrically transduced detection. First, COFs can be constructed with abundant accessible analyte binding sites through reticular synthesis or post-modification. Thus, COFs can be used as independent selective layers to modify the working electrodes to endow selectivity for a working electrode.<sup>272,273</sup> Second, COFs can be designed to have high surface areas, chemically stable skeletons, and good compatibility with other nanomaterials. Therefore, COFs can serve as excellent scaffolds to support different kinds of receptors, as electron mediators, as a conductive matrix, and/or as an electrochemically active material that can provide selective recognition ability or enhance electrochemical performance for the detection system.<sup>274–282</sup> Thirdly, through the choice of building blocks, the method for reticular synthesis, and post-functionalization, COFs can be built with inherent electrochemical activity and conductivity. In contrast to the first two situations, COFs themselves can act as active materials to mediate redox reactions of specific analytes for electrochemical detection<sup>283</sup> or as transducers in chemiresistive detection.<sup>91,128</sup> Among these three aspects, using COF as scaffolds for the modification of working electrodes in an electrochemical platform is currently the most applied strategy for electrically transduced detection.

**2.3.2 Electrically transduced detection using COFs.** Electrochemical detection based on COFs has been used for the analysis of a series of biology-related analytes in solution, such as DNA,<sup>272</sup>



proteins,<sup>274,277,278,284,285</sup> antibiotics,<sup>279,280</sup> and drug molecules.<sup>281,282,286</sup> Additionally, electrochemical detection of lead,<sup>287</sup> humidity,<sup>273</sup> and hydrogen peroxide<sup>283</sup> has also been reported. Compared with electrochemical methods, chemiresistive detection using COFs is less investigated, but several examples in gas sensing are beginning to emerge.<sup>91,128,288</sup>

In 2014, Wang *et al.* reported the first example of using COF (COF-LZU1) for electrochemical sensing of biomolecules.<sup>272</sup> The imine-linked COF-LZU1 was grown on an amino-functionalized silicon substrate, leaving a large number of edge amino groups on the surface of COF films (Fig. 23). These exposed amino groups are very helpful for adhesion of biomolecules, such as proteins or DNA, through strong electrostatic interactions. In aqueous solutions, the functional groups on biomolecules can be electrolyzed, which can promote the electrostatic interactions between biomolecules and COF films and improve the electronic charges flowing at the interfaces. The charged biomolecular species could also diffuse into the pores of COFs, resulting in a further enhancement of the electrochemical property. Consequently, EIS results demonstrated that the charge-transfer resistance ( $R_{ct}$ ) of the composite electrodes declined upon bovine serum albumin (BSA) adsorption and probe DNA immobilization, indicating that the adsorption of biomolecules onto COF films strengthened the electrochemical activity of the functional film.<sup>289,290</sup> This study showed that COFs could be alternative materials for biosensors by taking advantage of their functional groups on surfaces and porous structures.

COFs with an ordered structure, high porosity, low density, good biocompatibility, and outstanding stability<sup>291,292</sup> can act as platforms for anchoring selectors, such as aptamer strands<sup>275,278,285</sup> and antibodies,<sup>274,284</sup> for detecting other biomolecules. Aptamers are single-stranded DNA or RNA oligonucleotides that can show specific affinity toward target molecules. Zhou and coworkers reported a novel multiple electrochemical aptasensor based on

COF TBAPy-MA-COF-COOH for sensitive and simultaneous detection of miRNA 155 and miRNA 122.<sup>275</sup> The nanowires of TBAPy-MA-COF-COOH were used as a platform for anchoring single-stranded DNA (ssDNA), which was further hybridized with the complementary aptamer (cApt) probes of miRNA 155 and miRNA 122. Shell-encoded Au NPs with Cu<sub>2</sub>O were used as signal labels to connect to aptamer cApts. When contacting miRNAs, the signal labels immobilized with cApts were released from the hybridized DNA complex, which resulted in a substantial decrease of the DPV peak current of the signal labels. This TBAPy-MA-COF-COOH-based aptasensor can detect miRNA 155 and miRNA 122, with ultrasensitive low detection limits of 6.7 and 1.5 fM (S/N = 3), respectively, in a wide linear range of 0.01–1000 pM.

By anchoring antibodies and aptamers as selectors to COFs, several platforms for the detection of C-reactive protein (CRP) were developed.<sup>274,276,284,285</sup> For example, Yang and coworkers constructed a label-free CRP immunosensor using Pd(II)-coordinated COF-LZU1 (Pd/COF-LZU1)<sup>60</sup> immobilized with anti-CRP on the surface of a glassy carbon electrode (GCE).<sup>274</sup> When anti-CRP binds with CRP, the formed immune complex obstructs the electric signal of Fe(CN)<sub>6</sub><sup>4-/3-</sup>, which can be used to realize label-free detection of CRP by EIS and DPV. Under optimal experimental conditions, a linear range of 5–180 ng mL<sup>-1</sup> with an LOD of 1.66 ng mL<sup>-1</sup> was achieved.<sup>274</sup> An ultrasensitive electrochemical immunoassay for the detection of CRP was later demonstrated by the same group by using COF-LZU8 and the Au NPs-CoS/graphene oxide (GO) nanocomposite.<sup>284</sup> COF-LZU8 was functionalized by Au NPs and thionine (Thi) to serve as the electron transfer mediator, while the Au NPs-CoS/graphene oxide (GO) nanocomposite was utilized to immobilize the CRP antibody. Due to the high surface area of COF-LZU8, a great quantity of Thi could be adsorbed on the surface of the COF to amplify the PDV signal. Under optimum conditions, the system achieved a linear range of CRP detection of 0.05–150 ng mL<sup>-1</sup> with an LOD of 0.016 ng mL<sup>-1</sup>. The same group also developed a sandwich CPR electrochemical immunosensor comprising Au NP functionalized COF (Au NPs@COF-TpPa-1) as the matrix to immobilize the CRP antibody and nano-mimetic enzyme Co<sub>3</sub>O<sub>4</sub> NPs as tags to label the secondary CRP antibody.<sup>276</sup> This immunosensor can achieve a LOD of 0.017 ng mL<sup>-1</sup> for CRP and with good selectivity over other interferents, such as carcinoembryonic antigen (CEA), human chorionic gonadotropin (HCG), BSA, and prostate specific antigen (PSA).<sup>276</sup> A photoelectrochemical aptasensor for the label-free detection of CRP based on a 2D porphyrinic COF (p-COF) was developed by Zhang *et al.*<sup>285</sup> p-COF and aptamer modified silver NPs were used to generate a functionalized ITO/NiS electrode. CRP promoted the electron transfer between the active molecules H<sub>2</sub>O<sub>2</sub> and the electrode, diminishing the amplification effect of the photocurrent induced by H<sub>2</sub>O<sub>2</sub>, and leading to a decrease in the photocurrent response of the modified ITO/NiS electrode. The developed aptasensor exhibited a wide linear range of 0.5–100 ng mL<sup>-1</sup> and a LOD of 0.1 ng mL<sup>-1</sup>.

By introducing aptamers into a porphyrin-based COF (p-COF), Yan *et al.* developed an aptasensor that can selectively

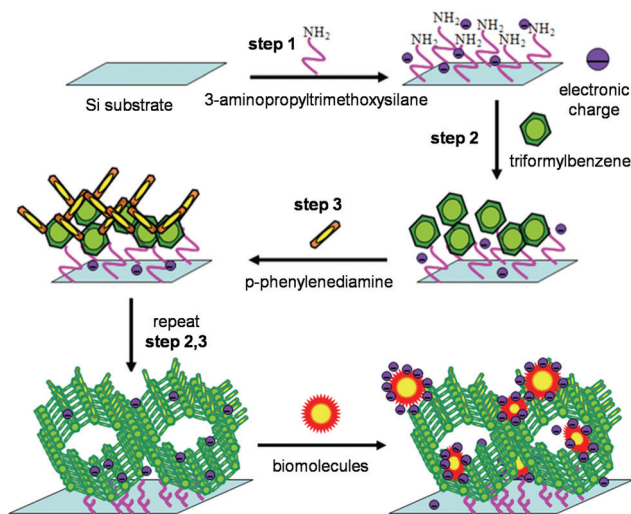


Fig. 23 Construction of an imine-linked COF on the surface for biomolecular detection.<sup>272</sup> Reprinted with permission from ref. 272. Copyright 2014, John Wiley and Sons.



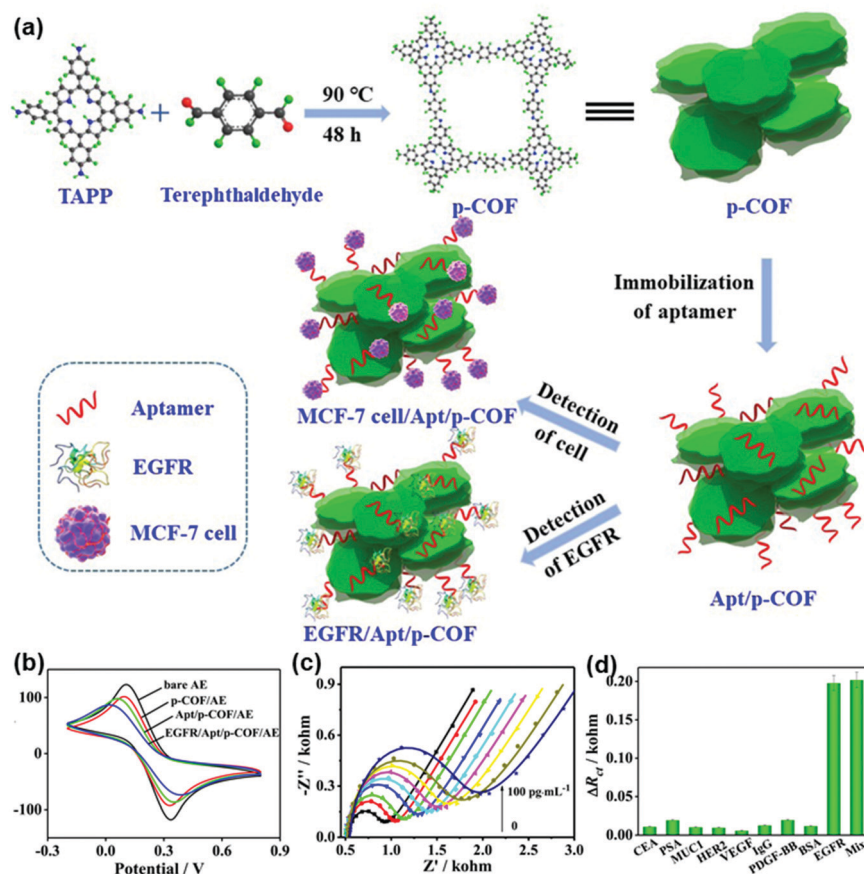


Fig. 24 (a) Schematic diagram of the p-COF-based aptasensor for detecting EGFR or MCF-7 cells. (b) CV curves of the p-COF-based aptasensor for detection of EGFR using the Au electrode (AE), p-COF/AE, Apt/p-COF/AE, and EGFR/Apt/p-COF/AE. (c) EIS responses of Apt/p-COF/AE with different EGFR concentrations of 0, 0.05, 0.1, 0.5, 1, 5, 50, and 100  $\mu\text{g mL}^{-1}$ . (d) Change of the charge transfer impedance ( $\Delta R_{ct}$ ) values of the p-COF-based electrochemical aptasensor by separately adding the interferents CEA, PSA, MUC1, HER2, VEGF, IgG, PDGF-BB, and BSA with a concentration of 0.1  $\text{ng mL}^{-1}$ , EGFR (0.1  $\mu\text{g mL}^{-1}$ ), and their mixture.<sup>278</sup> Adapted with permission from ref. 278. Copyright 2019, Elsevier.

and sensitively bind epidermal growth factor receptor (EGFR) and detect human breast carcinoma MCF-7 cells.<sup>278</sup> The label-free EGFR-targeting aptamer was immobilized onto p-COF *via* electrostatic interactions,  $\pi$ - $\pi$  stacking, and hydrogen bonding (Fig. 24a). When aptamer/p-COF was exposed to EGFR solution or living MCF-7 cells, interaction *via* biorecognition between these strands and EGFR or cells lowered the access of the redox probe ( $[\text{Fe}(\text{CN})_6]^{3-/4-}$ ) to the surface of the modified working electrode, leading to a decrease in electrochemical signals. The decrease in electrochemical responses was successively determined by CV (Fig. 24b), DPV, and EIS (Fig. 24c). The p-COF-based aptasensor exhibited extremely low LODs of 5.64 and 7.54  $\text{fg mL}^{-1}$  obtained from DPV and EIS, respectively, with a broad linear detection range of 0.05–100  $\mu\text{g mL}^{-1}$  EGFR. Interferents, including CEA, PSA, MUC1, HER2, VEGF, IgG, PDGF-BB, and BSA, had negligible effects on EGFR detection (Fig. 24d). When detecting living MCF-7 cells, the p-COF-based aptasensor showed a LOD of 61 cells  $\text{mL}^{-1}$  with a linear detection range of 500–10<sup>5</sup> cells  $\text{mL}^{-1}$ . The authors attributed the sensing performance of the p-COF aptasensor, including high selectivity, good stability, reproducibility, acceptable recyclability, and favorable applicability in human serum samples,

to a few structural features of the COF: (1) the two-dimensional nanosheet structure of p-COF can produce abundant binding sites for aptamer strands or biomolecules;<sup>293</sup> (2) the highly conjugated structure of p-COF can enhance the interaction with biomolecules, as well as improve the electrochemical activity; (3) the large channels of p-COF can facilitate aptamer immobilization and increase the amount of the probe adsorbed, further enhancing the detection sensitivity toward analytes.

A sandwich-type electrochemical immunosensor was constructed by Ren and coworkers for the ultrasensitive detection of cardiac troponin I (cTnI),<sup>277</sup> the accurate and rapid detection of which can help prevent acute myocardial infarction. In this immunosensor,  $\text{TiO}_2$  NPs modified with conductive polypyrrole ( $\text{TiO}_2$ -PPy) were used as the substrate material for the immobilization of the primary antibody  $\text{Ab}_1$ -cTnI. Au NP doped COFs and the electron mediator toluidine blue (TB-Au-COFs) behaved as labels for achieving signal amplification (Fig. 25a). Meanwhile, TB-Au-COFs also provided active sites for the immobilization of the secondary antibody  $\text{Ab}_2$ -cTnI. Square wave voltammetry (SWV) showed a linear increase of current with the increase of cTnI concentrations from 0.5  $\mu\text{g mL}^{-1}$  to 10.0  $\text{ng mL}^{-1}$  (Fig. 25b and c), affording a low LOD of 0.17  $\mu\text{g mL}^{-1}$ . When this





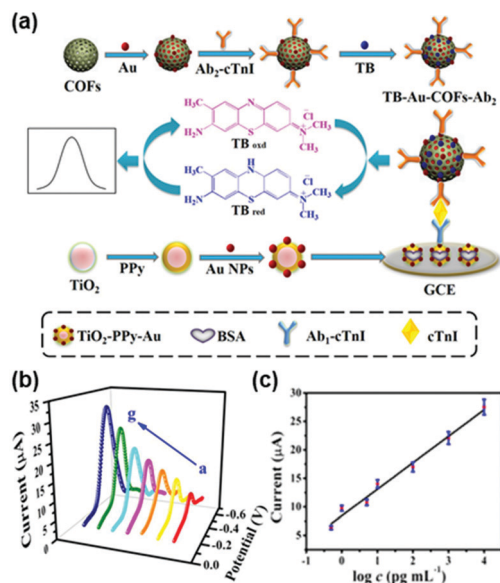


Fig. 25 (a) Schematic illustration of the sandwich-type electrochemical immunosensor. (b) SWV current responses with increasing cTnI concentrations from 0.5 pg mL<sup>-1</sup> to 10.0 ng mL<sup>-1</sup>. (c) Calibration curve of the immunosensor for the detection of different concentrations of cTnI.<sup>277</sup> Adapted with permission from ref. 277. Copyright 2018, Elsevier.

immunosensor was used to test cTnI in human serum samples, good recoveries (96.0–102%) and low relative standard deviations (1.8–3.9%) were achieved.<sup>277</sup>

Besides the detection of DNA,<sup>272</sup> RNA,<sup>275</sup> and proteins<sup>274,277,278,284,285</sup> demonstrated above, COFs have also been investigated for the detection of antibiotics<sup>279,280</sup> and drug molecules.<sup>281,282,286</sup> In those studies, without exceptions, COFs have been carefully modified with various functional nanomaterials including MOFs,<sup>279,286</sup> Au NPs,<sup>281</sup> and MWCNTs,<sup>282</sup> and/or connected with selectors, such as aptamer<sup>280,286</sup> and MIP,<sup>282</sup> to form a compositional material. Usually, the large surface area and abundant functional groups of COFs, the electrochemical activities or catalytic abilities of the nanoparticles, and/or selective binding ability from the selectors can function conjointly to result in a synergistic effect to improve the detection performance of the compositional material which the components in isolation are not able to achieve. For example, Au NPs are one kind of widely used nanomaterials in electrochemical sensors due to their unique catalytic activity; however, free Au NPs tend to agglomerate which is detrimental to their catalytic performance. TAPB-DMTP-COFs can act as the host matrix to support Au NPs with the unsaturated amine group present on TAPB-DMTP-COF, which can effectively avoid the agglomeration of Au NPs.<sup>281</sup> The electrochemical detection using the Au NP modified COF composite (TAPB-DMTP-COF/Au NPs) exhibited a good electrocatalytic activity toward the oxidation of chlorogenic acid (CGA)<sup>294,295</sup> and displayed a wide linear range of  $1.0 \times 10^{-8}$ – $4.0 \times 10^{-5}$  mol L<sup>-1</sup>, a low LOD of  $9.5 \times 10^{-9}$  mol L<sup>-1</sup> as well as a good repeatability of 4.1% in  $2.0 \times 10^{-5}$  mol L<sup>-1</sup> CGA.<sup>281</sup> Compared with Au NPs, the improved stability of the

system resulted in excellent durability with a cycling time of more than 100.<sup>281</sup>

COFs developed thus far experienced limited utility as electrode materials in electrochemical analysis, due to their low conductivity resulting in low current output. Combining COFs with a conductive matrix<sup>296,297</sup> provides a practical strategy to overcome the conductivity issues of COFs to improve their electrochemical performance.<sup>298</sup> Xu and coworkers used a composite comprising conductive amino-functionalized carbon nanotubes and COF<sub>TTA-DHTA</sub> (NH<sub>2</sub>-MWCNT@COF<sub>TTA-DHTA</sub>), as well as molybdenum disulfide (MoS<sub>2</sub>) to modify the GCE as a novel electrochemical sensor for selective recognition of sulfamerazine (SMR).<sup>282</sup> A molecularly imprinted polymer (MIP) membrane was anchored on the surface of this modified GCE further to achieve selective recognition of SMR. The electrochemical performance of the assembled electrochemical sensor was investigated with DPV and CV. This sensor displayed excellent selectivity for SMR and good reproducibility. Under optimal conditions, the sensor offered a wide current response for SMR from  $3.0 \times 10^{-7}$  to  $2.0 \times 10^{-4}$  mol L<sup>-1</sup>, with a LOD of  $1.1 \times 10^{-7}$  mol L<sup>-1</sup>. Furthermore, this developed sensor was successfully applied for the determination of SMR in pork and chicken samples with recoveries of 86.0–102.0%; the results were comparable to those obtained by high-performance liquid chromatography.<sup>282</sup>

COF-based conductive composites can be fabricated into electrodes for electrochemical detection of metal ions. For instance, Wang and coworkers developed an electrochemical sensor for the sensitive and selective determination of Pd<sup>2+</sup> in an aqueous medium using a carbon paste electrode by mixing TAPB-DMTP-COF with graphite.<sup>299</sup> Pd<sup>2+</sup> was detected by differential pulse anodic stripping voltammetry. Under optimum conditions, the method showed excellent linearity to the concentration of Pd<sup>2+</sup> in the range of 0.0050 to 2.0 μmol L<sup>-1</sup> with a LOD of 1.9 nM. The extraordinary performance was ascribed to the high specific surface of TAPB-DMTP-COF that provided a high effective electroactive surface area and the abundant terminal amino groups at the edges of the COF that had coordination capability to Pd<sup>2+</sup>. Sulfhydryl functionalized COF modified Au electrodes were fabricated by Wang *et al.* for the selective detection of Pd<sup>2+</sup> in water samples.<sup>287</sup> The sulfhydryl groups were introduced by post-synthetic modification to enhance the selectivity for Pd<sup>2+</sup>. A LOD of 0.015 ng mL<sup>-1</sup> was obtained, lower than the level of Pd<sup>2+</sup> in drinking water permitted by the WHO (10 ng mL<sup>-1</sup>). Metal ions, such as Mg<sup>2+</sup>, Ni<sup>2+</sup>, Zn<sup>2+</sup>, Cr<sup>2+</sup>, Fe<sup>2+</sup>, Cu<sup>2+</sup>, Cd<sup>2+</sup>, Hg<sup>2+</sup>, and Ca<sup>2+</sup>, have a negligible influence on Pd<sup>2+</sup> detection.<sup>287</sup>

Utilizing the affinity of the boron ester linkage towards water molecules, Pal and coworkers developed a truxene-based boron ester COF (COF-TXDBA) for the measurement of relative humidity (RH) using EIS.<sup>273</sup> The condensation reaction between the truxene based ligand and 1,4-phenylenediboronic acid (DBA) gave a crystalline COF with boron ester linkages. The powder X-ray diffraction experiment indicated that boron ester linkages interacted with water molecules in the planar sheets of COF backbones with the empty orbitals of the boron atom interacting with the electron lone pair of the oxygen atom in the



water molecule. Under low RH, water molecules were adsorbed on the surface of COF-TXDBA to form the first chemisorbed layers, which were discontinuous under low RH, thus resulting in high impedance. However, under high RH, a multilayer of water molecules can form, which favors the charge transportation process by the Grotthuss chain reaction ( $\text{H}_2\text{O} + \text{H}_3\text{O}^+ \rightarrow \text{H}_3\text{O}^+ + \text{H}_2\text{O}$ ), and results in a sharp increase in the proton conductivity of the sensor.<sup>300</sup> This COF-TXDBA based RH sensor exhibited a reversible change of 3 orders of magnitude in impedance in the RH range of 11–98% with a response and recovery time of 37 s and 42 s, respectively.

Redox-active materials can usually serve as redox mediators to couple with the redox reactions of electrochemically active analytes. The redox potential of analyte species can then be brought to moderate or low values, which will be easier to access using normal amperometric and voltammetric testing conditions. The possible signals from redox-active interference species or electrolytes can also be minimized. To serve as an electron mediator in electrochemical detection, COFs have largely relied on the external electrochemically active components, such as redox-active organic molecules<sup>277,284</sup> and Au NPs.<sup>281</sup> The intrinsic redox activity of COFs has been less utilized. However, incorporating redox-active ligands can be used as a strategy to generate COFs with multiple redox processes,<sup>74,301–307</sup> which could be used as active materials to catalyze specific substances and to construct ratiometric electrochemical sensors. Wang and coworkers reported a COF ( $\text{COF}_{\text{DHTA-TTA}}$ ) with electroactive monomers 4,4',4''-(1,3,5-triazine-2,4,6-triyl)trianiline (TTA) and 2,5-dihydroxyterephthalaldehyde (DHTA) as multiple redox-active sites as a novel electrochemical sensing and biosensing platform (Fig. 26a).<sup>283</sup>  $\text{COF}_{\text{DHTA-TTA}}$  itself can be directly used as an active material in a ratiometric electrochemical sensor for the determination of hydrogen peroxide and pH level based on current and potential signals. The ratio of current at  $-0.5$  and  $0.3$  V linearly increased with  $\text{H}_2\text{O}_2$  concentration from  $8.06$  to  $400$   $\mu\text{M}$ , and the LOD was estimated to be  $2.42$   $\mu\text{M}$  (Fig. 26b). The DPV response of  $\text{COF}_{\text{DHTA-TTA}}/\text{GCE}$  in the presence of interfering chemicals, including glucose, galactose, mannose, fructose,  $\text{Cl}^-$ ,  $\text{K}^+$ , UA, and AA, had only slight effects on  $\text{H}_2\text{O}_2$  detection (Fig. 26c). As the electron transport process of  $\text{COF}_{\text{DHTA-TTA}}/\text{GCE}$  was accompanied by  $\text{H}^+$  transfer, pH could be also determined. The peak potential at around  $-0.15$  V linearly shifted as the pH of PBS (phosphate buffered saline) solution varied from  $11.0$  to  $3.0$  with a high sensitivity of  $64.2$   $\text{mV pH}^{-1}$  (Fig. 26d). Because  $\text{COF}_{\text{DHTA-TTA}}$  had a good catalytic activity for oxygen reduction reaction in PBS ( $\text{pH} = 7.0$ ), glucose oxidase was further loaded on  $\text{COF}_{\text{DHTA-TTA}}$  via its nanosized pores and abundant active sites from the N-rich skeleton for glucose sensing. The glucose oxidase- $\text{COF}_{\text{DHTA-TTA}}$  system exhibited linear responses to glucose from  $1.26$   $\mu\text{M}$  to  $6.0$   $\text{mM}$  at  $-0.30$  V, as well as from  $0.60$   $\mu\text{M}$  to  $6.0$   $\text{mM}$  at  $-0.53$  V (Fig. 26e). This work presented an example to construct electrochemical sensors by directly using redox-active COFs as electroactive materials.<sup>283</sup>

As demonstrated in the previous sections, COFs are appealing candidates for the fabrication of devices for chemical

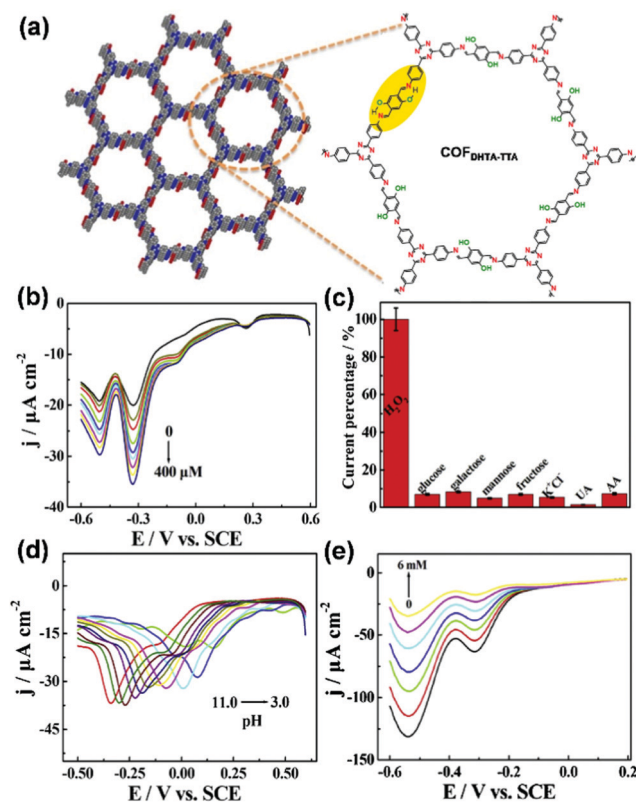


Fig. 26 (a) Chemical model and structure of  $\text{COF}_{\text{DHTA-TTA}}$ . (b) DPV responses of  $\text{COF}_{\text{DHTA-TTA}}/\text{GCE}$  in  $0.2$  M  $\text{N}_2$ -saturated PBS ( $\text{pH} = 7.0$ ) toward different  $\text{H}_2\text{O}_2$  concentrations. (c) DPV response of  $\text{COF}_{\text{DHTA-TTA}}/\text{GCE}$  toward glucose, galactose, mannose, fructose,  $\text{Cl}^-$ ,  $\text{K}^+$ , UA, and AA in  $0.2$  M  $\text{N}_2$ -saturated PBS ( $\text{pH} = 7.0$ ). (d) DPV response of  $\text{COF}_{\text{DHTA-TTA}}/\text{GCE}$  in  $0.2$  M  $\text{N}_2$ -saturated PBS with different pH. (e) DPV responses of GOD/ $\text{COF}_{\text{DHTA-TTA}}/\text{GCE}$  in  $0.2$  M  $\text{O}_2$ -saturated PBS ( $\text{pH} = 7.0$ ) with constant addition of glucose.<sup>283</sup> Adapted with permission from ref. 283. Copyright 2019, Elsevier.

detection in the context of their large surface-to-volume ratio, chemically robust skeleton, and programmable functional active sites for analytes. However, significant challenges arise when utilizing them directly in electrically transduced detection as stimuli-responsive electrodes because most COFs have insufficient electrical conductivity to be integrated into electronic devices. Several conductive COFs, however, have been recently developed<sup>91–93,308–311</sup> by taking inspiration from the development of other classes of conductive materials including conductive organic polymers,<sup>312,313</sup> conductive organic molecular solids,<sup>314–316</sup> and conductive metal–organic frameworks.<sup>317–319</sup> The construction of conductive COFs usually follows the basic design principles of maximizing the through-bond and through-space charge transport by employing electroactive building units, conjugated linkages, stacked structures, and chemical doping.<sup>91–93,125,262,308–311,320–322</sup> These developments of COFs with moderate to good electrical conductivity<sup>78,91,92,125,309–311,320,322,323</sup> provide new opportunities for electrically transduced detection.

In 2019, our research team constructed a conductive COF ( $\text{COF-DC-8}$ ) through the aromatic annulation of 2,3,9,10,16,17,23,24-octa-aminophthalocyanine nickel(II) and pyrene-4,5,9,10-tetraone



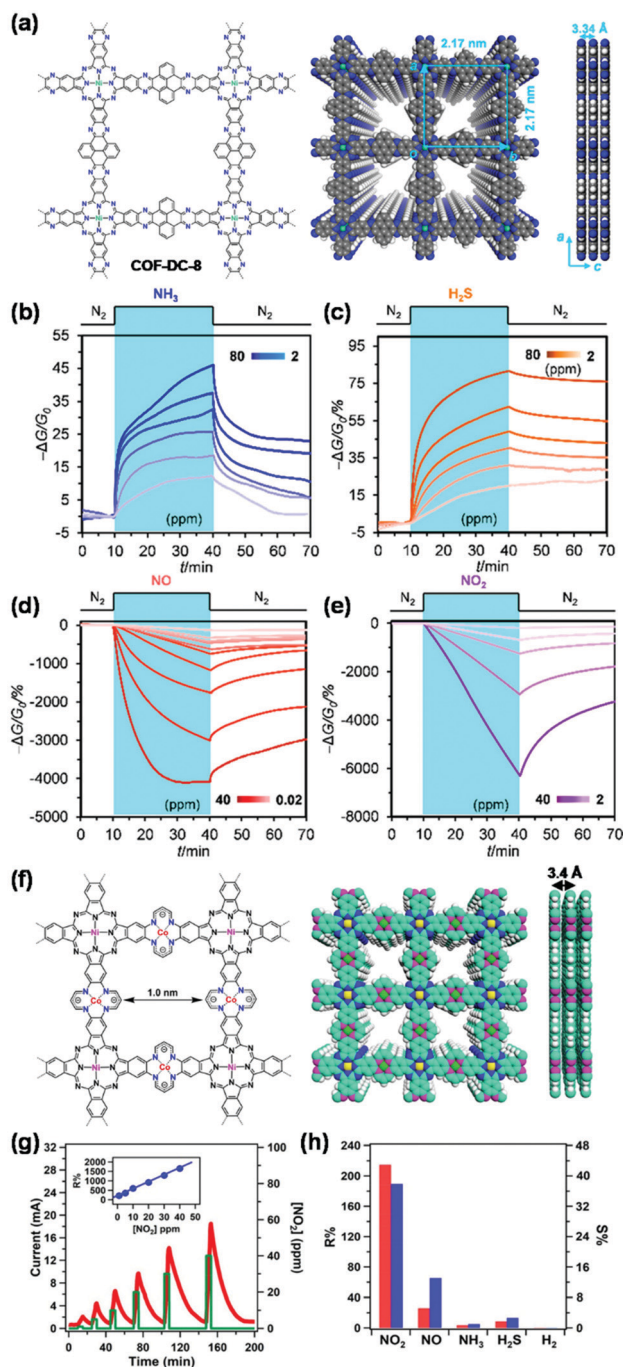


Fig. 27 (a) Chemical structure and model of **COF-DC-8**. Chemiresistive responses of devices with integrated **COF-DC-8** to (b)  $\text{NH}_3$ , (c)  $\text{H}_2\text{S}$ , (d)  $\text{NO}$ , and (e)  $\text{NO}_2$  under an applied voltage of 1.0 V and in an atmosphere of dry nitrogen.<sup>91</sup> Adapted with permission from ref. 91. Copyright 2019, American Chemical Society. (f) Chemical structure and model of **NiPc-CoTAA**. (g) Time-dependent response–recovery current plot of the NiPc-CoTAA film at  $\text{NO}_2$  concentrations from 1 to 40 ppm. The inset shows the linear relation between  $R\%$  and  $\text{NO}_2$  concentration. (h) Responsivity and sensitivity of the NiPc-CoTAA film towards different gases  $\text{NO}_2$ ,  $\text{NO}$ ,  $\text{NH}_3$ ,  $\text{H}_2\text{S}$ , and  $\text{H}_2$  at 1 ppm (red bar,  $R\%$ ; blue bar,  $S\%$ ).<sup>288</sup> Adapted with permission from ref. 288. Copyright 2021, John Wiley and Sons.

and demonstrated the first implementation of a conductive COF as the active material for chemiresistive detection (Fig. 27a).<sup>91</sup>

The intrinsic bulk conductivity of the COF material reached  $2.51 \times 10^{-3} \text{ S m}^{-1}$ . This good electrical conductivity, together with the ability of the built-in nickelphthalocyanine units to interact with a wide range of analytes, made this COF a promising candidate for chemiresistive gas detection. Upon integration into chemiresistive devices, COF-DC-8 showed excellent responses to various reducing and oxidizing gases, including  $\text{NH}_3$ ,  $\text{H}_2\text{S}$ ,  $\text{NO}$ , and  $\text{NO}_2$  (Fig. 27b–e). COF-DC-8 was found to be especially sensitive toward oxidizing gases, with pronounced responses observed for  $\text{NO}$  and  $\text{NO}_2$ , which was consistent with the p-type characteristic of the COF. The LODs for these gases reached the parts-per-billion (ppb) level, which was 70 ppb for  $\text{NH}_3$ , 204 ppb for  $\text{H}_2\text{S}$ , 5 ppb for  $\text{NO}$ , and 16 ppb for  $\text{NO}_2$ , based on response values at 1.5 min exposure. Electron paramagnetic resonance spectroscopy and X-ray photoelectron spectroscopy studies suggested that the chemiresistive response of COF-DC-8 involved charge-transfer interactions between the analyte and the nickelphthalocyanine component of the framework.<sup>91</sup> This study demonstrated the high potential of using conductive COFs in chemiresistive detection.

Recently, Huang and coworkers developed a new kind of conductive phthalocyanine-based framework NiPc-CoTAA for  $\text{NO}_2$  detection (Fig. 27f).<sup>288</sup> NiPc-CoTAA featured a conjugated tetraaza[14]annulene linkage and densely stacked  $\pi$ -units, which rendered this material with a low band gap of 0.86 eV and high electrical conductivity up to  $8.16 \times 10^{-3} \text{ S m}^{-1}$ . The thin film device of NiPc-CoTAA made by the steam-assisted conversion method exhibited significant sensitivity towards several redox gases, including  $\text{NO}_2$ ,  $\text{NO}$ ,  $\text{NH}_3$ ,  $\text{H}_2\text{S}$ , and  $\text{H}_2$ . Upon exposure to  $\text{NO}_2$  gas at concentrations of 1–40 ppm at 298 K, the NiPc-CoTAA thin-film device exhibited a high response up to 1658% with good linearity (Fig. 27g). NiPc-CoTAA exhibited a superior  $\text{NO}_2$  sensing selectivity to that of  $\text{NO}$ ,  $\text{NH}_3$ ,  $\text{H}_2\text{S}$ , and  $\text{H}_2$  at 298 K (Fig. 27h). These results demonstrated that the NiPc-CoTAA film not only exhibited high sensitivity, but also good selectivity as a chemiresistive sensor.<sup>288</sup>

As the analyte–material interaction can result in changes of both optical and electrical properties of COFs, it is possible to realize different types of transduction modes by using the same COF detection system. Bojdys and coworkers reported a 2D COF PBHP-TAPT made up of chemoresistant  $\beta$ -amino enone bridges (PBHP) and Lewis-basic triazine moieties (TAPT), which was capable of real-time, reversible sensing of volatile acids and bases through both the optical and conductivity changes of the material.<sup>128</sup> The study showed that a single-site protonation occurred at the triazine moiety upon the exposure to acid. This protonation gave the triazine moieties a localized positive charge, drawing  $\pi$ -electron density from the neighboring functional groups of triazine units, which caused a fluorescence quenching of the COF accompanied by a color change from yellow to red. Interestingly, besides optical changes, the acid–base exposure cycle led to a reversible conductivity change of the COF. PBHP-TAPT had a normalized conductivity of  $1.32 \times 10^{-8} \text{ S m}^{-1}$ , which upon protonation was increased by 170-fold to  $2.18 \times 10^{-6} \text{ S m}^{-1}$ . The conductivity dropped close to the original value when the sample was regenerated with  $\text{NH}_3$  vapors. Solid-state UV-vis diffuse reflectance spectroscopy showed that the



bandgap of the PBHP-TAPT COF decreased by  $\sim 0.3$  eV upon protonation. This study illustrated that both the optical and electronic property change of a COF can be used for chemical detection. Taking full advantage of the porous structure and the fully aromatic donor-acceptor conjugation of COFs is a powerful approach to design practical sensors and switches.<sup>128</sup>

COFs have shown good potential in electrically transduced detection in various biology-related analytes, metal ions, humidity, pH, and gases (Table 4). Several platforms have been utilized for real sample detection, showing excellent sensitivity and selectivity.<sup>276–278,282,287</sup> Those achievements capitalize on the intriguing features of large surface area, abundant active binding sites, and feasible functionalization ability. Despite the encouraging progress, the use of COFs for electrically transduced detection is still at a very early stage and there are still several impending challenges in making use of the full potential of COFs in electrically transduced detection. It is worth noting that most of the current detection systems relied heavily on the construction of composite materials for the improvement of sensing performance. The fabrication of these composites usually needs tedious engineering procedures that involve multiple components. The resulting composites may be challenged in long-term stability that can be detrimental to the detection performance.<sup>324</sup> To date, there is still no report on which COFs are used solely as electrode materials for electrochemical detection. One major reason for this is that many COFs have low electrical conductivity. The combination with conductive additives provides a solution for this issue;<sup>282,299</sup> however, it may be at the expense of device simplicity and stability. Using composite materials may also result in the reduction of surface area, the shielding of analyte binding sites, as well as the interference of redox-active components embedded within the COF, leading to unpredictable changes in the detection process.<sup>319</sup> Compared with the use of COF composites, the epitaxial growth of COFs on conductive substrates may provide a better alternative for obtaining stable electrode materials with improved electrochemical performance.<sup>298,302,325,326</sup> Last, but not least, the development of COFs that have an elegant combination of high electrical conductivity, specific active binding sites for the target, as well as redox-active units is expected to lead to advanced applications of this group of multifunctional materials in electrically transduced detection.

## 2.4 Detection based on extraction coupled with chromatography and spectrometry

**2.4.1 Basics of extraction coupled with chromatography and spectrometry for detection.** Chromatography combined with various instrumental techniques, such as mass spectrometry and nuclear magnetic resonance spectroscopy, is one of the primary techniques traditionally being recognized as reliable and robust for routine chemical analysis.<sup>328,329</sup> However, many sources of samples are usually adulterated with various backgrounds, such as hydrocarbons, inorganic salts, or other interfering chemicals, that pose difficulties in chromatographic and spectroscopic analysis because in the presence of these

background or interfering chemicals, these analyses may give spurious information because of the eclipse of analyte signals by background signals.<sup>24</sup> Moreover, the analyte of interest can be present in a very low concentration in the real samples. A direct analysis may fail to give a reliable signal to ensure the accuracy of the detection.

Therefore, prior to instrumental analysis of trace-level analytes in complex samples, sample preparation is an inevitable part of the extraction and enrichment of target analytes from a sample matrix.<sup>330</sup> Extraction techniques are promising tools in sample preparation for separation and enrichment. Solid-phase extraction (SPE), which is based on the partition equilibrium of the analytes between the sample and the solid absorbent,<sup>331</sup> can enrich and purify targets simultaneously. It has become the most widely applied extraction technique because of its high extraction efficiency, simple operation, good reproducibility, and low required consumption.<sup>24,331</sup> Up to now, a series of SPE methods have been developed, including dispersive microsolid-phase extraction, magnetic solid-phase extraction, and solid-phase microextraction. In microsolid-phase extraction, the suspension of nanomaterial adsorbents is directly mixed into the aqueous sample and dispersed by ultrasonication, and then adsorbents are separated from the sample solution by centrifugation or filtration.<sup>332</sup> Magnetic solid-phase extraction (MSPE) is based on the universal dispersion of a magnetizable or magnetic material as the sorbent.<sup>333</sup> In MSPE, the solid phase can be easily separated under a magnetic field, which simplifies the preparation steps. Solid-phase microextraction (SPME) involves the use of a fused silica or metal fiber substrate covered with an appropriate sorbent coated thin layer, which can extract different kinds of volatile and non-volatile analytes from the gas or liquid phase.<sup>334,335</sup> SPME is a non-exhaustive sample pretreatment and can shorten the time of extraction, improve efficiency and enhance sensitivity due to the integration of sampling, analyte or matrix isolation, and enrichment into a single step.<sup>336</sup>

In SPE, elimination of backgrounds can be achieved by partitioning the desired analytes from complex samples to the surface of the SPE sorbent. This partition is kinetically or thermodynamically driven by the physiochemical properties of the SPE sorbent. Therefore, the composition and structure of the adsorbent material play an important role in extraction which determines the selectivity and sensitivity of the analysis.<sup>337</sup> Polymeric sorbents are often used; however, they may suffer from irreversible sorption, ineffective transportation of analytes, and swelling, which can lead to slow adsorption/desorption kinetics and impair selective adsorption.<sup>338–340</sup> Many new coatings have been developed, such as ionic liquid/polymeric ionic liquids,<sup>341</sup> molecularly imprinted polymers,<sup>342</sup> carbon nanotubes (CNTs),<sup>343</sup> graphene,<sup>344</sup> and metal/metal oxide nanoparticles.<sup>345</sup> However, these materials still have their limitations, such as low adsorption capacity, limited stability in aqueous samples with low or high pH, and low selectivity.

Significant efforts have been devoted to the development of advanced sorbent materials with improved selectivity or specificity towards target analytes, high sorptive capacity, and





Table 4 Summary of electrically transduced detection using COFs

Analyte(s)	Method	COF	Detection architecture	LOD	Detection range	Other detection parameters	Ref.
BSA	Electrochemistry: EIS	COF-LZU1	COF-LZU1/Si	N/A	N/A	0.1 M KCl	272
DNA	Electrochemistry: EIS	COF-LZU1	COF-LZU1/Si	N/A	N/A	0.1 M KCl	272
CRP	Electrochemistry: EIS, DPV	COF-LZU1	Pd-COF-LZU1-anti-CRP/GCE	1.66 ng mL <sup>-1</sup>	5–180 ng mL <sup>-1</sup>	0.01 M PBS, pH = 7.5; selectivity over BSA, HCG, Gly, Glu	274
H <sub>2</sub> O	Electrochemistry: EIS	COF-TXDBA	COF-TXDBA/Ag-Pd electrode	N/A	11% RH and 98% RH	Response time 37 s, recovery time 42 s, reversible	273
CRP	Electrochemistry: DPV	COF-LZU8	Thi-Au NPs-COF-LZU8	0.016 ng mL <sup>-1</sup>	0.05–150 ng mL <sup>-1</sup>	N/A	284
CRP	Electrochemistry: EIS, CV	COF-TpPa-1	Au NPs@COF-TpPa-1/chitosan/GCE	0.017 ng mL <sup>-1</sup>	0.05–80 ng mL <sup>-1</sup>	PBS buffer, pH = 7.5; selectivity over CEA, HCG, BSA, PSA	276
OTC	Electrochemistry: EIS, CV	MCA	Ce-MOF@MCA/aptaMER/AE	35 fM	2 × 10 <sup>-4</sup> –1.0 nM	0.1 M PBS, pH = 7.4; selectivity over NO <sub>3</sub> <sup>-</sup> , Cl <sup>-</sup> , Ca <sup>2+</sup> , Mg <sup>2+</sup> , L-alanine, D-phenylalanine, AMP, bleomycin, doxycycline hyclate, streptomycin sulphate, Kana, UA, and urea; milk, wastewater, and urine samples	286
CRP	Photoelectrochemical	p-COF	NiS and Ag NPs-p-COF-CRP aptamer/ITO	0.1 ng mL <sup>-1</sup>	0.5 to 100 ng mL <sup>-1</sup>	0.1 M PBS, pH = 7.4; selectivity over HCG, PSA, MC-LR, BSA, HCG; serum	285
Chlorogenic acid	Electrochemistry: CV, DPC	TAPB-DMTP-COF	TAPB-DMTP-COF/Au NPs/GCE	9.5 × 10 <sup>-9</sup> M	1.0 × 10 <sup>-8</sup> –4.0 × 10 <sup>-5</sup> mol L <sup>-1</sup>	PBS, pH = 7.0; Fe <sup>3+</sup> , Na <sup>+</sup> , K <sup>+</sup> , Ca <sup>2+</sup> , Cu <sup>2+</sup> , Zn <sup>2+</sup> , Mg <sup>2+</sup> , PO <sub>4</sub> <sup>3-</sup> , NH <sub>4</sub> <sup>+</sup> , Cl <sup>-</sup> , and SO <sub>4</sub> <sup>2-</sup> , uric acid, dopamine, guanine, L-dopa, glucose, hydroquinone, creatine, adenine, and catechol, AA, thymol, rutin and quercetin, caffeic acid, gallic acid, and vanillic acid; food and drink samples	281
Pd <sup>2+</sup>	Electrochemistry: CV, DPASV	APB-DMTP-COF	APB-DMTP-COF/CPE	1.9 nM	0.0050–2.0 μM	Acetate buffer solution, pH = 4.5; selectivity over Cu <sup>2+</sup> , Hg <sup>2+</sup> , Cd <sup>2+</sup> , Ni <sup>2+</sup> , Co <sup>2+</sup> , Mn <sup>2+</sup> , Fe <sup>2+</sup> , Zn <sup>2+</sup> , Cr <sup>3+</sup> , Sn <sup>2+</sup> , Ag <sup>+</sup> , Mg <sup>2+</sup> , Al <sup>3+</sup> , K <sup>+</sup> , Na <sup>+</sup> , Mg <sup>2+</sup> , Ca <sup>2+</sup> , NO <sub>3</sub> <sup>-</sup> , F <sup>-</sup> , Cl <sup>-</sup> , Br <sup>-</sup> , SCN <sup>-</sup> , SO <sub>4</sub> <sup>2-</sup> , CO <sub>3</sub> <sup>2-</sup> , PO <sub>4</sub> <sup>3-</sup> , SiO <sub>3</sub> <sup>2-</sup> ; real water samples	299
cTnI	Electrochemistry: SWV	PPy	TiO <sub>2</sub> -PPy-Au/GCE	0.17 pg mL <sup>-1</sup>	0.5 pg mL <sup>-1</sup> –10.0 ng mL <sup>-1</sup>	0.1 M PBS, pH = 7.4; selectivity over insulin, CEA, PSA, and squamous cell carcinoma antigen; human serum samples	277
miRNAs	Electrochemistry: DPV	TBAPy-MA-COF	TBAPy-MA-COF NWs/Au NPs/aptaMER/GCE	6.7 fM (miRNA 155) 1.5 fM (miRNA 122)	0.01–1000 pM	PBS, pH = 7.4; selectivity over miRNA 122, 141, 205, 21; human serum	275
Dopamine	Electrochemiluminescence	TpBD	MIP/UCNPs/CTpBD-Au/GC	2 × 10 <sup>-15</sup> M	10 <sup>-14</sup> –10 <sup>-6</sup> M	0.1 M PBS, pH = 7.4; selectivity over adrenaline, PEA, caffeic acid, UA, AA, Ca <sup>2+</sup> , NH <sub>4</sub> <sup>+</sup> , K <sup>+</sup> , Na <sup>+</sup> , SO <sub>4</sub> <sup>2-</sup> , NO <sub>3</sub> <sup>-</sup> , Cl <sup>-</sup> ; human serum	327
AMP	Electrochemistry: EIS	TPN-COF	apt/Co-MOF@TPN-COF/AE	0.217 fg mL <sup>-1</sup>	0.001–2000 pg mL <sup>-1</sup>	0.01 M PBS, pH = 7.4; ADR, TOB, RFP, Kana, BSA, Ca <sup>2+</sup> , and Na <sup>+</sup> ; human serum, river water and milk	279
Sulfamerazine	Electrochemistry: DPV	N/A	NH <sub>2</sub> -MWCNT@COF/GCE	1.1 × 10 <sup>-7</sup> M	3.0 × 10 <sup>-7</sup> –2.0 × 10 <sup>-4</sup> M	0.2 M Britton–Robinson buffer solution, pH = 5.0; selectivity over glucose, glutamic acid, ascorbic acid; meal samples	282
ENR	Electrochemistry: EIS	Py-M-COF	Apt <sub>ENR</sub> /Py-M-COF/AE	6.07 fg mL <sup>-1</sup>	0.01 pg mL <sup>-1</sup> –2 ng mL <sup>-1</sup>	0.01 M PBS, pH = 7.4; selectivity over tetracycline, Kana, TOB, Na <sup>+</sup> , K <sup>+</sup> , streptomycin, and OTC	280
AMP	Electrochemistry: EIS	Py-M-COF	Apt <sub>AMP</sub> /Py-M-COF/AE	0.04 fg mL <sup>-1</sup>	0.01 pg mL <sup>-1</sup> –2 ng mL <sup>-1</sup>	0.01 M PBS solution, pH = 7.4; selectivity over tetracycline, Kana, TOB, Na <sup>+</sup> , K <sup>+</sup> , streptomycin, and OTC	280



Table 4 (continued)

Analyte(s)	Method	SWASV	COF	Detection architecture	LOD	Detection range	Other detection parameters	Ref.
Pb <sup>2+</sup>	Electrochemistry	SWASV	TAPB-BMTTPA-COF	TAPB-BMTTPA-COF/AE	0.015 ng mL <sup>-1</sup>	0.05–20 ng mL <sup>-1</sup>	Acetic acid/sodium acetate buffer solutions, pH = 5.0; selectivity over <sup>+</sup> Ni <sup>2+</sup> , Zn <sup>2+</sup> , Cu <sup>2+</sup> , Fe <sup>3+</sup> , Cd <sup>2+</sup> , Hg <sup>2+</sup> , Ca <sup>2+</sup> , Na <sup>+</sup> and K <sup>+</sup> ; environmental waters	287
H <sub>2</sub> O <sub>2</sub>	Electrochemistry	CV, DPV	COF <sub>DHTA-TTA</sub>	COF/DHTA-TTA/GCE	1.70–2.42 μM	5.66–400 μM	0.2 M Na <sub>2</sub> -saturated PBS, pH = 7.0; selectivity over galactose, mannose, fructose, Cl <sup>-</sup> , K <sup>+</sup> , UA and AA	283
H <sup>+</sup>	Electrochemistry	CV, DPV	COF <sub>DHTA-TTA</sub>	COF/DHTA-TTA/GCE	N/A	pH 3–11	0.2 M Na <sub>2</sub> -saturated PBS	283
Glucose	Electrochemistry	CV, DPV	COF <sub>DHTA-TTA</sub>	Glucose oxidase GOD/COF/DHTA-TTA/GCE	0.18–0.38 μM	0.60 μM–6.0 mM	0.2 M Na <sub>2</sub> -saturated PBS, pH = 7.0; selectivity over galactose, mannose, fructose, Cl <sup>-</sup> , K <sup>+</sup> , UA and AA	283
EGFR	Electrochemistry	DPV, EIS	p-COF	apt/p-COF/AE	5.64 fg mL <sup>-1</sup> (DPV) 7.54 fg mL <sup>-1</sup> (EIS)	0.05–100 pg mL <sup>-1</sup>	PBS, pH = 7.4; CEA, PSA, MUC1, HER2, VEGF, IgG, PDGF-BB, and BSA	278
MCF-7 cells	Electrochemistry	EIS	p-COF	apt/p-COF/AE	61 cells mL <sup>-1</sup>	500–10 <sup>5</sup> cells mL <sup>-1</sup>	0.1 M PBS, pH = 7.4; selectivity over L929 cells	278
HCl	Chemiresistor		PBHP-TAPT	PBHP-TAPT pellet	N/A	N/A	Reversible on exposure to NH <sub>3</sub>	128
NH <sub>3</sub>	Chemiresistor		COF-DC-8	COF-DC-8/AE	56.8–70 ppb	2–80 ppm	N <sub>2</sub>	91
H <sub>2</sub> S	Chemiresistor		COF-DC-8	COF-DC-8/AE	121 ppb	2–80 ppm	N <sub>2</sub>	91
NO	Chemiresistor		COF-DC-8	COF-DC-8/AE	1–5 ppb	0.02–40 ppm	N <sub>2</sub>	91
NO <sub>2</sub>	Chemiresistor		COF-DC-8	COF-DC-8/AE	1–16 ppb	2–40 ppm	N <sub>2</sub>	91
NO <sub>2</sub>	Chemiresistor		NiPe-CoTAA	NiPe-CoTAA thin film/AE	N/A	1–40 ppm	N <sub>2</sub> , sensitivity (%) 37.6 ppm <sup>-1</sup> , selectivity over NO, NH <sub>3</sub> , H <sub>2</sub> S, and H <sub>2</sub>	288

enhanced chemical and physical-mechanical stability. Currently, there is a trend toward the exploration of crystalline and porous materials for SPE, for example, MOFs, to realize improved sensitivity, selectivity, and repeatability of sample preparation techniques. Still, many MOFs have insufficient chemical stability in solvents, which can result in a decrease of the adsorption capacity after prolonged exposure to the solution of samples, hindering their further applications in SPE.<sup>346,347</sup>

COFs, as novel porous materials, have shown their advantages in solid-phase extraction. First, covalent organic frameworks have permanent porosity, well-defined pore structures, and high surface areas, which are beneficial in analyte uptake. The programmable pore parameters (size and geometry) can be harnessed to realize the size exclusive effect for selective extraction. Second, the modular synthesis and feasible functionalization ability of COFs allow the introduction of abundant functional groups, which can further enhance the adsorption efficiency and selectivity. Third, COFs can be designed with excellent thermal and chemical stability. Compared with their analogs, such as MOFs,<sup>346,347</sup> microporous polymers,<sup>348</sup> and hypercrosslinked polymers,<sup>349</sup> COFs have been proven to be more stable in water and acidic media. Thus, COFs can be utilized in SPE under harsh conditions but still show good long-term stability. Fourth, COFs are usually made of light elements, such as H, B, C, N, and O, which endow them with processability and feasibility to be integrated with the silica or metal fiber substrate in solid-phase microextraction or to form membranes.<sup>350</sup> COFs have been utilized as absorbents in dispersive microsolid-phase extraction, MSPE, and solid-phase microextraction for the detection of industrial chemicals,<sup>351–376</sup> pesticides and insecticides,<sup>377–382</sup> chemical warfare agents,<sup>24</sup> ions,<sup>383</sup> drug molecules,<sup>384–390</sup> and biomolecules<sup>391,392</sup> in safety inspection of water and food, environmental monitoring, and analysis of biological mixtures. In most cases, the detection is performed by coupling solid-phase extraction with HPLC, GC, MS, or chromatography–mass spectrometry combinations to enable quantitative analysis.

**2.4.2 Extraction coupled with chromatography and spectrometry for detection.** Chemicals produced from industries, such as dyes, polycyclic aromatic hydrocarbons, phthalate esters, phenols, *etc.*, can be discharged into the natural world during their production and transportation to cause environmental pollution.<sup>351,374</sup> Besides, a lot of consumer products, such as coloring agents, plasticizers, preservatives, or other additives, which are widely used in building materials, clothing, medical devices, cosmetics, food packaging, and insecticides, may be present in drinking water and food, and pose health issues to human beings. Therefore, the detection and monitoring of these chemicals are practically important. However, they are usually present in trace-level concentrations in complicated environmental and biological samples. It is crucial to simultaneously isolate and enrich those analytes by efficient sample preparation methods before instrumental analysis.

*Aromatic dyes.* Dyes are coloring compounds that are widely used in the fabrication of fibers; however, their residues in food



or textiles are strictly regulated. In 2005, Zhang *et al.* demonstrated the utilization of a crystalline hydrazone linked covalent organic polymer (HL-COP) as an adsorbent in micro-solid-phase extraction for online analysis of trace Sudan dyes in food samples (Fig. 28a).<sup>351</sup> This HL-COP adsorbent contained abundant phenyl rings and imine ( $-C=N$ ) groups with rich  $\pi$  electrons. HL-COP showed remarkable preconcentration ability for six kinds of Sudan dyes with enrichment factors as high as 305–757. The adsorption mechanism may involve  $\pi$ - $\pi$  affinity, hydrophobic effect, hydrogen bonding, and donor-acceptor interaction, which contributed to its strong recognition affinity to target compounds. The adsorption amounts by HL-COP were 1.0–11.0 fold those by three commonly used commercial adsorbents, including multiwall carbon nanotubes, graphene, and C18 silica gel (Fig. 28b). When HL-COP was applied as an adsorbent of online micro-solid-phase extraction coupled with HPLC for enrichment and analysis of trace Sudan dyes in food samples, low LODs of 0.03–0.15  $\mu\text{g L}^{-1}$  could be achieved. The method was successfully applied for online analysis of chilli powder (Fig. 28c) and sausage samples with recoveries in the range of 75.8–108.2% and 73.8–112.6%, respectively. These results suggested that COFs can serve as promising sample preparation media for sampling, enrichment, and separation purpose in real sample analysis when coupled with the chromatography technique.

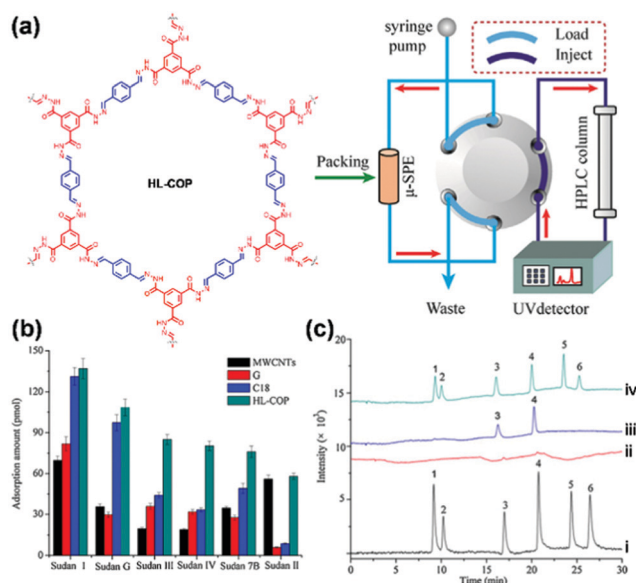


Fig. 28 (a) The HL-COP adsorbent packed online micro-solid-phase extraction-HPLC system. (b) Extraction performance of HL-COP adsorbents for six Sudan dyes compared with three commonly used commercial adsorbents. (c) Chromatograms for the analysis of the chilli powder: (i) the mixed standard solution of six Sudan dyes ( $10.0 \mu\text{g L}^{-1}$ ); (ii) direct injection of the extracted solution of chilli powder; (iii) online enrichment of extracted solution of chilli powder; (iv) online enrichment of the extracted solution for the spiked chilli powder sample with  $10.0 \mu\text{g kg}^{-1}$  of six Sudan dyes. Peaks 1–6 are Sudan Red G, Sudan I, Sudan II, Sudan III, Sudan Red 7B, and Sudan IV, respectively.<sup>351</sup> Adapted with permission from ref. 351. Copyright 2015, Elsevier.

**Polycyclic aromatic hydrocarbons (PAHs).** PAHs are well-known environmental pollutants with strong carcinogenic and endocrine-disrupting properties.<sup>393</sup> It is of great importance to monitor and control the amount of PAHs in the environment. A few detection methods that combine SPE<sup>355,372</sup> or MSPE<sup>353,358,363,365</sup> using COF-LZU1,<sup>353</sup> TpBD,<sup>358,365,372</sup> COF-SCU1,<sup>355</sup> and TpDA<sup>363</sup> with HPLC and GC have been established. The high extraction efficiency of these COFs can be usually attributed to strong  $\pi$  stacking and hydrophobic interactions between COFs and polycyclic aromatics. For example, Wang *et al.* used a COF LZU-1 based magnetic adsorbent for MSPE of PAHs.<sup>353</sup> COF LZU-1<sup>60</sup> was covalently immobilized onto polyethyleneimine-functionalized magnetic nanoparticles (COF-LZU1@PEI@Fe<sub>3</sub>O<sub>4</sub>), which allowed rapid separation from the sample solution with the help of a magnetic field. COF-LZU1@PEI@Fe<sub>3</sub>O<sub>4</sub> displayed high extraction efficiency for PAHs such as pyrene, benzo[a]pyrene, fluoranthene, benz[a]anthracene, benzo[a]fluoranthene, and dibenz[a,h]-anthracene, attributed to strong  $\pi$  stacking and hydrophobic interaction between COF-LZU-1 and polycyclic aromatics. PAHs were then quantified by HPLC after desorption with acetonitrile. The MSPE-HPLC method showed low LODs of 0.2–20  $\text{pg mL}^{-1}$ , wide linear ranges, and good reproducibility (relative standard deviations <4.4%). The method was successfully applied to determine PAHs in environmental samples with recoveries ranging from 90.9 to 107.8% for water samples and 85.1 to 105.0% for soil samples.

To realize the efficient and durable separation of the adsorbents and sample solution, Pang *et al.* reported the use of COF TpBD grown onto stainless steel wire as an SPME fiber, which was used as the solid-phase microextraction fiber to extract PAHs for subsequent GC-MS determination in grilled meat samples.<sup>372</sup> COF TpBD was grown on stainless steel wire modified by polydopamine that served as a linker to react with benzidine (Fig. 29a). The TpBD bonded fiber showed good durability, which can stand at least 200 cycles without significant loss of extraction efficiency. The TpBD bonded SPME fiber gave much larger enhancement factors than commercial SPME coatings, including PDMS fibers, PDA fibers, and etched stainless steel wire (Fig. 29b). The developed method could be successfully applied for the determination of trace PAHs in grilled meat samples with recoveries from 85.1% to 102.8%.

**Phenols.** Phenols are primarily used to produce polycarbonate plastics and resins or used as deoxidants, and have been implicated in a wide variety of problems, including endocrine disruption, carcinogenicity, and neurotoxicity.<sup>394</sup> A few COFs have been utilized as adsorbents in magnetic solid-phase extraction,<sup>356,359,360,366</sup> solid-phase microextraction,<sup>367,369,376</sup> and micro solid-phase extraction<sup>362</sup> for the analysis of phenolic species in biological, food, and water samples. For example, Lin and coworkers reported the use of core-shell structured magnetic COF (Fe<sub>3</sub>O<sub>4</sub>@COF) nanocomposites as an adsorbent for MSPE of bisphenols (BPs) from human serum samples.<sup>356</sup> The Fe<sub>3</sub>O<sub>4</sub>@COF-TAPB-PDA nanocomposites with a core-shell structure possessed a high specific surface area ( $181.36 \text{ m}^2 \text{ g}^{-1}$ ), uniform mesoporous size ( $\sim 3.6 \text{ nm}$ ), high saturation magnetization



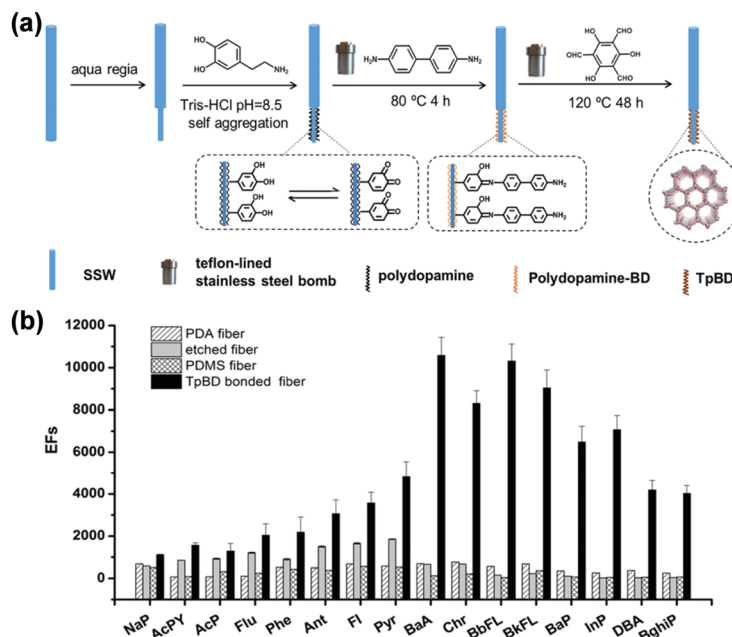


Fig. 29 (a) Schematic illustration of fabrication of the TpBD bonded SPME fiber. (b) Comparison of the PDA coated fiber, etched fiber, PDMS coated fiber and TpBD bonded fiber for the extraction of PAHs.<sup>372</sup> Adapted with permission from ref. 372. Copyright 2019, Elsevier.

(42.7 emu g<sup>-1</sup>), and good thermal and chemical stability. Using the nanocomposite as an adsorbent, MPSE coupled with HPLC-MS gave good linearity within the concentration range of 0.1–50 µg L<sup>-1</sup> of bisphenols. The method was also applicable for the analysis of trace BPs in human serum samples.<sup>356</sup> Recently, a method for rapid detection of trace tetrabromobisphenol A (TBBPA) in water media was developed by Yu and coworkers by combining COF-based solid-phase microextraction (SPME) with constant flow desorption ionization mass spectrometry.<sup>367</sup> The particles of COF TpBD were directly coated on a disposable glass fiber (Fig. 30a) for the solid-phase microextraction. The porous structure, suitable channel size, secondary amine group, carbonyl group, as well as the benzene/aromatic

ring in the framework that allows  $\pi$ - $\pi$  stacking interaction between TBBPA and TpBD enabled the use of TpBD as an effective adsorbent for organic pollutants. TBBPA was then ionized and transmitted into the linear trap quadrupole-mass spectrometer (Fig. 30b and c). An enrichment factor of 185 was achieved to result in a 3.6 to 7.2-fold increase in the peak area of the TBBPA ion compared to commercial fibers. Moreover, compared with the traditional HPLC or HPLC-MS protocols, the developed method presented significantly reduced analytical time (7 min vs. 30 min) and much lower LOD values (0.92 ng L<sup>-1</sup> vs. 23–900 ng L<sup>-1</sup>).

The selectivity and enrichment ability of COFs could be improved by their functionalization. Zhao and coworkers synthesized a boric acid-functionalized COF (B-COF) by using 2,4,6-trihydroxy-1,3,5-benzenetri-aldehyde and benzidine as ligands and 4-aminophenyl-boronic acid as a functionalization linker for the specific enrichment and direct detection of *cis*-diol-containing compounds by MALDI-TOF MS assay.<sup>368</sup> B-COF possessed boric acid groups that have selective affinity to capture *cis*-diol-containing compounds, including luteolin, riboflavin, and pyrocatechol. High selectivity against target analytes was obtained in the presence of 100 times more *anti*-interference compounds. The LODs of as low as 0.01–0.50 fg mL<sup>-1</sup> were achieved for luteolin, riboflavin, and pyrocatechol with the enrichment of B-COF.<sup>368</sup>

Solid-phase extraction was also applied for the analysis of phenolic compounds in environmental water,<sup>360</sup> drink,<sup>366</sup> food samples,<sup>359,376</sup> and others<sup>362</sup> with good recovery values. In most of the cases, the extraction efficiencies were dominantly determined by the covalent or noncovalent interactions between the analyte and COFs. Different from these examples, a recent study by Zhao and coworkers showed that the size of the pores in COFs may also play a role.<sup>369</sup> The authors fabricated a

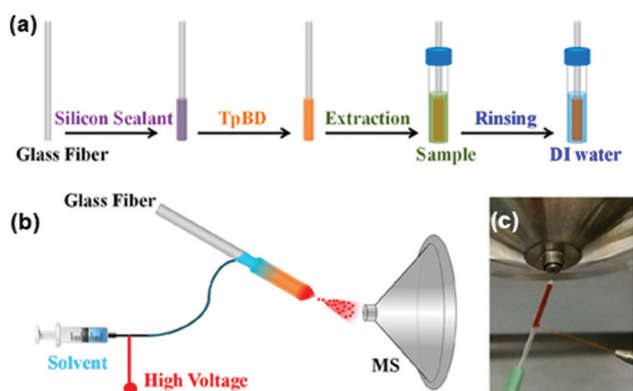


Fig. 30 (a) Schematic illustration of the preparation of the TpBD coated fiber and SPME process. (b) Schematic illustration of SPME coupled with constant flow desorption ionization MS. (c) Photograph of the Taylor cone formed between the end of the fiber and the MS inlet.<sup>367</sup> Adapted with permission from ref. 367. Copyright 2019, American Chemical Society.



spherical TPB-DMTP-COF with high acid/base stability, thermostability, and large surface area as the coating for solid-phase microextraction.<sup>369</sup> They found that the enhancement factors of TPB-DMTP-coated fibers increased with the number of chlorine or methyl substituents. Hence, the strong adsorption affinity could be derived from a size-matching effect with the combination of  $\pi$ - $\pi$  affinity, H-bonding, and van der Waals forces.

**Halogenated aromatics.** Halogenated aromatics, usually used as intermediates of industry products, are recognized as a class of highly toxic environmental contaminants.<sup>395</sup> The toxicity and bioaccumulation of these compounds make the ability to detect them at extremely low levels a necessity.<sup>396</sup> To improve the extraction efficiency and selectivity, Jiang *et al.* developed an aptamer-functionalized magnetic core-shell material for selective extraction of trace amounts of hydroxylated polychlorinated biphenyls.<sup>357</sup> The aptamer bearing amino groups was immobilized on the surface of the magnetic COF-COOH through covalent linkage with carboxyl groups (Fig. 31a). The resulting  $\text{Fe}_3\text{O}_4$ @CO-Apt material thus combined the advantages of easy separation, porous structure, high surface area, and specific affinity for hydroxylated polychlorinated biphenyls. The extraction procedure of the targets involved the dispersion of  $\text{Fe}_3\text{O}_4$ @COF-Apt in the sample solution, ultrasonication, and collecting from the solution with a magnet (Fig. 31b). The adsorbed targets on  $\text{Fe}_3\text{O}_4$ @COF-Apt were eluted with solvent and subjected to subsequent HPLC-MS determination. Compared with the nonmodified COF and  $\text{Fe}_3\text{O}_4$ ,  $\text{Fe}_3\text{O}_4$ @COF-Apt provided much higher selectivity for hydroxy-2',3',4',5,5'-pentachlorobiphenyl (2-OH-CB 124) (Fig. 31c), indicating that

the aptamer played a significant role in improving the selectivity toward 2-OH-CB 124 due to its high binding affinity to the target. The maximum adsorption capacity of  $\text{Fe}_3\text{O}_4$ @COF-Apt for 2-OH-CB 124 reached  $37.17 \mu\text{g g}^{-1}$  (Fig. 31d). This aptamer-functionalized COF provided a wide linear range of  $0.01$ – $40 \text{ ng mL}^{-1}$  and a LOD as low as  $2.1 \text{ pg mL}^{-1}$  when used for the capture and detection of 2-OH-CB 124 in human serum.

COFs are normally non-selective to molecules that are smaller than their cavities in the extractions. To develop selective, simple, and rapid extraction pretreatments for the detection of trace polychlorinated biphenyl (PCB) residues in soils, Wang *et al.* developed a mesoporous titanium dioxide and TPB-TP-COF composite coating ( $\text{Fe}_3\text{O}_4$ @ $\text{mTiO}_2$ @TPB-TP-COF) onto a Nd-Fe-B magnet for headspace sorptive extraction.<sup>364</sup> This new coating exhibited good selectivity over PAHs, like naphthalene and benzopyrene, which was hypothesized as due to a synergistic effect resulting from the unique compositional structure of the  $\text{Fe}_3\text{O}_4$ @ $\text{mTiO}_2$ @TPB-TP-COF coating.<sup>364</sup> The outer COF coating has cavities of uniform size ( $\sim 3.9 \text{ nm}$ ), which may allow PCBs to pass freely while excluding larger-sized macromolecules. The inner  $\text{mTiO}_2$  coating has a good affinity towards chlorine-containing organic compounds, which can improve the selectivity for PCBs. Under optimal conditions, the LOD was measured to be less than  $0.06 \text{ ng g}^{-1}$  with a linear range of  $0.01$ – $100 \text{ ng g}^{-1}$ . The analysis of brominated<sup>370</sup> and fluorinated aromatics<sup>373</sup> was also implemented by coupling solid-phase extraction with GC-MS and surface-assisted laser desorption/ionization time-of-flight mass spectrometry, respectively.

**Pesticides.** Pesticides have been widely applied in agriculture and their residues in the environment and food can cause acute or chronic biological poisoning. Solid-phase extractions using COFs coupled with chromatography and mass spectrometry have been proven to be effective and reliable tools for the analysis of trace pyrethroid and benzoylurea-based pesticide residues in various complex food substrates. The high adsorption capacity and good selectivity are usually from  $\pi$ -stacking and hydrophobic interactions between pesticides and COFs.<sup>377–382</sup> For example, Li and coworkers developed an analytical method for the simultaneous determination of pesticides in fruit samples by magnetic solid-phase extraction combined with ultra-high performance liquid chromatography and tandem mass spectrometry.<sup>382</sup> A composite made of triazine-imine COF TRI-TER grown on amino-functionalized  $\text{Fe}_3\text{O}_4$  was applied as the magnetic sorbent for efficient enrichment and rapid separation of pesticides. LODs ranging from  $0.4$  to  $1.2 \text{ ng L}^{-1}$  were achieved for eight pesticides which can meet the requirement for ultra-trace analysis of pesticides. The established method was successfully applied to actual fruit samples.<sup>382</sup>

**Ions.** As discussed in Section 2.2.3, C=N and C=O groups present in many COF structures can coordinate to metal ions. In addition, stronger coordination sites could also be strategically introduced into COFs. These features suggest that COFs can be used as sorbents for extraction of metal ions. Wang and

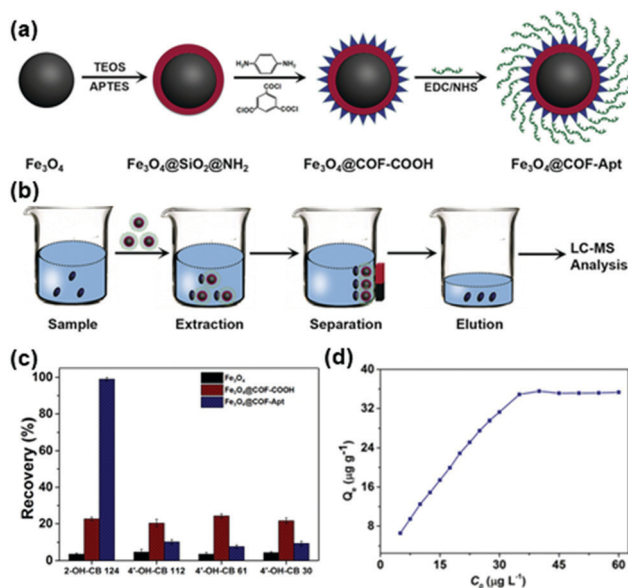


Fig. 31 (a) Synthetic scheme of  $\text{Fe}_3\text{O}_4$ @COF-Apt and (b) typical process for selective extraction of OH-PCBs with  $\text{Fe}_3\text{O}_4$ @COF-Apt. (c) Comparison of the extraction efficiency of 2-OH-CB 124, 4'-OH-CB 112, 4'-OH-CB 61, and 4'-OH-CB 30 with  $\text{Fe}_3\text{O}_4$ ,  $\text{Fe}_3\text{O}_4$ @COF-COOH, and  $\text{Fe}_3\text{O}_4$ @COF-Apt. (d) Adsorption isotherm of 2-OH-CB 124 with  $\text{Fe}_3\text{O}_4$ @COF-Apt.<sup>357</sup> Adapted with permission from ref. 357. Copyright 2018, John Wiley and Sons.





coworkers examined two COFs TpBD and CTpBD as sorbents for solid-phase extraction and analysis of trace ions *via* flow injection followed by inductively coupled plasma mass spectrometry (ICP-MS).<sup>383</sup> TpBD showed effective adsorption to only five metal ions, including  $V^{4+}$ ,  $Cu^{2+}$ ,  $As^{3+}$ ,  $Se^{4+}$ , and  $Mo^{4+}$ , while CTpBD demonstrated SPE performance to up to ten metal ions, such as  $Cr^{3+}$ ,  $Mn^{2+}$ ,  $Co^{2+}$ ,  $Ni^{2+}$ ,  $Cd^{2+}$ ,  $V^{5+}$ ,  $Cu^{2+}$ ,  $As^{3+}$ ,  $Se^{4+}$ , and  $Mo^{6+}$ , probably due to the presence of the COOH functional groups in CTpBD that provided strong coordination with metal ions. Owing to the intrinsic porous structure and metal-binding capability of CTpBD, preconcentration of the target trace elements *via* the COF-filled on-line SPE column achieved low detection limits of 2.1–21.6 ng L<sup>-1</sup> along with a wide linearity range at 0.05–25 µg L<sup>-1</sup> for all target ions. This method was successfully utilized for trace element analysis in environmental and food samples.

**Biomolecules.** Besides the utilization of COFs as absorbents for the detection of aromatics, phenols, pesticides, and ions demonstrated above, their use in the detection of a few biomolecules, including phosphopeptides, glycopeptides, and antibodies, is also reported. The selective enrichment of trace phosphopeptides from complex biological mixtures is indispensable for phosphoproteome studies. In the most common approach for phosphopeptide enrichment, immobilized metal ion affinity chromatography (IMAC) based on the chelation/coordination chemistry is adopted. However, this approach involves tedious synthetic processes due to the use of chelating ligands and solid supports. As an alternative, incorporating metal ions into the COFs with metal coordination capability can provide solid-phase matrices for the selective enrichment of the peptides. Shen and coworkers developed a novel COF-based IMAC material (TpPa-2-Ti<sup>4+</sup>) by direct immobilization of Ti<sup>4+</sup> into the TpPa-2 COF without using extra chelating ligands.<sup>385</sup> The permanent porosity, high specific surface areas, well-ordered hexagonal 2D topology, and strong chemical stability endowed TpPa-2-Ti<sup>4+</sup> composites with high metal ion loading densities as well as excellent mass transportation and enrichment performance.<sup>88</sup> The obtained Ti<sup>4+</sup>-modified COF demonstrated a low LOD of 4 fmol and satisfactory selectivity for the capture of phosphopeptides from peptide mixtures of tryptic digestion ( $\beta$ -casein:BSA = 1:100). It was also successfully applied for the enrichment of phosphopeptides from non-fat milk and HeLa cells.<sup>385</sup>

Post-synthetic modification can offer the advantage of incorporation of on-demand desired functionalities on the surface of COF backbones to improve the extraction capacity and selectivity meanwhile maintaining the structural regularity of COFs. A core-shell structured COF composite (MCNC@COF@Zr<sup>4+</sup>) with a magnetic colloid nanocrystal cluster (MCNC) as the core and Zr<sup>4+</sup> ion-functionalized two-dimensional COFs as the shell was recently reported by Lin and coworkers for efficient and selective enrichment of phosphopeptides.<sup>387</sup> A three-step sequential functionalization that involved the conversion of hydroxyl groups to carboxyl groups, the introduction of pami-dronic acid (PA) to obtain desired phosphate groups, and the

formation of Zr<sup>4+</sup>-immobilized magnetic COF composites was performed for the post-functionalization of the COF (Fig. 32a). The as-prepared MCNC@COF@Zr<sup>4+</sup> can serve as an effective adsorbent for selective enrichment of phosphopeptides attributed to its regular mesoporous structure with high surface area and the high affinity interaction between Zr<sup>4+</sup> ions and phosphate groups. Direct analysis (Fig. 32b) or treatment by MCNC@COF composites (Fig. 32c) for tryptic digests of 100 µg mL<sup>-1</sup>  $\beta$ -casein did not show obvious signals using MALDI-TOF mass spectra; in contrast, after treating  $\beta$ -casein with the MCNC@COF@Zr<sup>4+</sup> composites, three phosphopeptides ( $\beta$ 1,  $\beta$ 2, and  $\beta$ 3) possessing both the phosphorylated parts and dephosphorylated counterparts were identified with enhanced signal intensities (Fig. 32d). A low detection threshold of 10 fmol for phosphopeptides was obtained. Moreover, the unique pore structure endowed a size-exclusion effect of biomacromolecules, such as lysozyme and concanavalin A. This effectiveness of the MCNC@COF@Zr<sup>4+</sup> composites in screening biomacromolecules background was advantageous in real complex samples' analysis, which was further evidenced by selective enrichment of phosphopeptides from the tryptic digests of defatted milk (Fig. 32e) and direct capture of low-abundance 14 endogenous phosphopeptides from 10-fold diluted human serum.<sup>387</sup>

Given the regular pore sizes and controllable chemical affinities by modifications, COFs are also potential candidates for the capture of *N*-linked glycopeptides, which are a kind of biomarkers for early diagnosis of various diseases.<sup>397,398</sup> Gao and coworkers developed a COF-functionalized magnetic graphene biocomposite (MagG@COF-5) as an ultrasensitive hydrophilic matrix for recognizing *N*-linked glycopeptides.<sup>391</sup> Due to the strong  $\pi$ - $\pi$  interactions between ligands and graphene, layers of COF-5 could be successfully coated on the surface of magnetic graphene *via* a hydrothermal reaction (Fig. 33a). The coating of the COF on graphene was recognized to possess multipurpose functionalities and could be used as an extraction matrix when coupled with MALDI-TOF-MS for *N*-linked glycopeptide analysis (Fig. 33b). First, the unique  $\pi$ - $\pi$  electron structure and strong magnetic properties of magnetic graphene composites provided binding sites for targets and facilitated rapid and convenient separation by a magnet. Second, the coating of COF-5 can be used as a molecular gate to exclude large-sized proteins from complex biological samples through the size-exclusion effect. Third, the high surface area of COF-5 coating can ensure high loading capacity. For these unique characteristics, the MagG@COF-5 biocomposite showed excellent performance in *N*-linked glycopeptide analysis with a LOD of 0.5 fmol µL<sup>-1</sup>, an excellent size-exclusion effect (HRP digests/BSA selectivity, 1:600), and good recyclability and reusability. 232 *N*-linked glycopeptides from 85 glycoproteins were detected by treatment of human serum with this biocomposite, demonstrating the potential of MagG@COF-5 for use in glycoproteome and clinical diagnosis fields.

The regular arrangement of active sites and porous structure of COFs offer a suitable platform for protein immobilization with consistent orientation, which can serve as a solid matrix



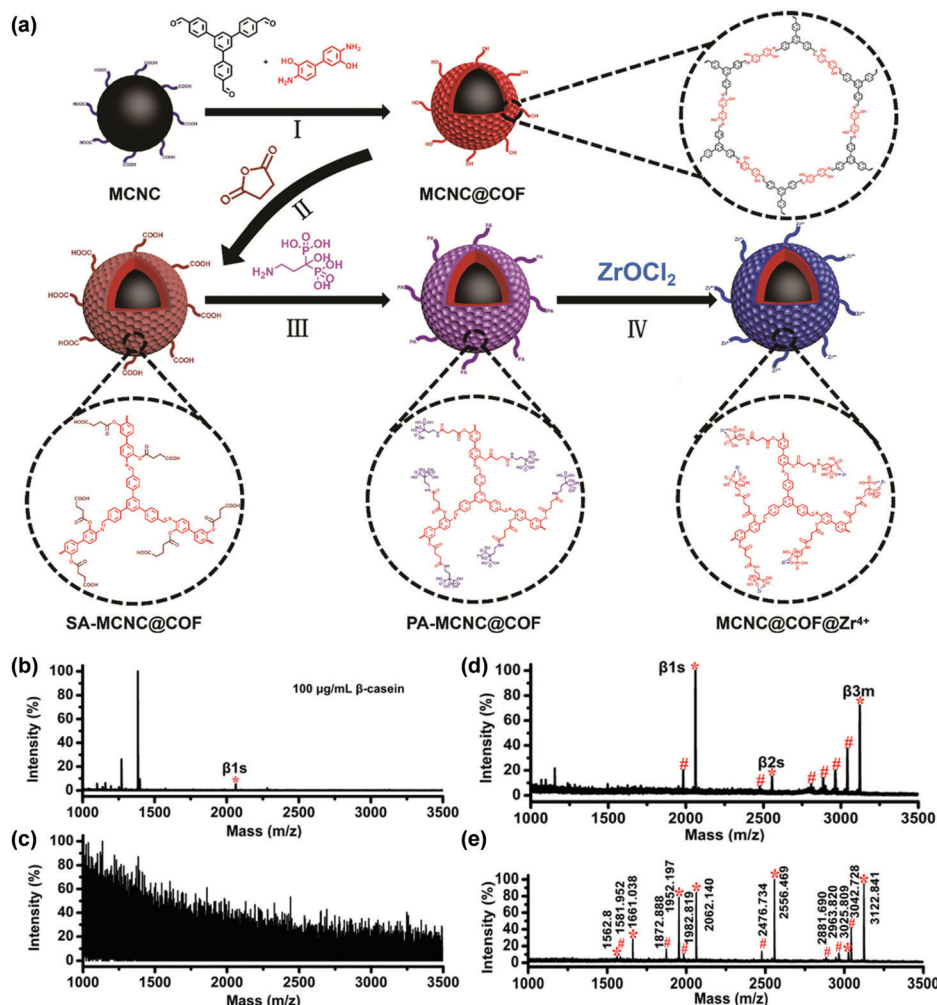


Fig. 32 (a) Representation of the strategy for preparing Zr<sup>4+</sup>-immobilized magnetic COFs through sequential post-synthetic modifications. MALDI-TOF mass spectra of the tryptic digests of β-casein from (b) direct analysis, (c) analysis after enrichment with MCNC@COF composites, and (d) analysis after enrichment with MCNC@COF@Zr<sup>4+</sup> composites. (e) MALDI-TOF mass spectra of the tryptic digests of defatted milk after enrichment with MCNC@COF@Zr<sup>4+</sup> composites.<sup>387</sup> Adapted with permission from ref. 387. Copyright 2019, American Chemical Society.

for immunoassay. Fang and coworkers developed an immunoaffinity probe, Fe<sub>3</sub>O<sub>4</sub>@TpBD-DSS-Ab-MEG, based on magnetic COFs with anchored antibodies for the detection of a cancer biomarker, heat shock protein 90α (Hsp90α).<sup>392</sup> The fabricated composites with Fe<sub>3</sub>O<sub>4</sub> as the magnetic core and COF TpBD as the shell exhibited several appealing features, including strong magnetic responses (7.96 emu g<sup>-1</sup>), ordered active groups, a large number of immobilized antibodies (111.7 µg mg<sup>-1</sup>), and good solvent and thermal stability. Attributed to these features, Fe<sub>3</sub>O<sub>4</sub>@TpBD-DSS-Ab-MEG demonstrated a low LOD of 50 pg mL<sup>-1</sup> and high selectivity over BSA. Furthermore, 2 peptides of Hsp90α were successfully observed in human plasma. This immunoassay strategy thus offered an ability for accurate analysis of low-abundant protein biomarkers in complicated biological matrices.

As adsorbents for solid-phase extraction,<sup>59,399–402</sup> COFs present good adsorption performance towards many analytes, attributed to their high surface area, regular porous channels,

abundant functional groups, and stable chemical structures. This sample preparation method, coupled with various chromatographic and spectrometric techniques, has become a powerful tool for the analysis of trace-level analytes in complex samples, ranging from various aromatic compounds, pesticides and insecticides, chemical warfare agents, ions, drug molecules, to biomolecules in environmental, food, and biological samples (Table 5). Even though a lot of reports have shown the appealing detection performance of COFs toward specific analytes in real samples, further development towards the practical use of COF materials for simple, quick, and efficient extraction techniques is still highly desired. Firstly, COFs still possess limited selectivity for analytes with similar structures, which has been seen in the detection of PAHs and ions. Because the interaction between COFs and those analytes is mainly based on weak intermolecular interactions, such as π–π stacking interactions, hydrogen bonding interactions, coordination reactions, and van der Waals force, they usually lack specificity.



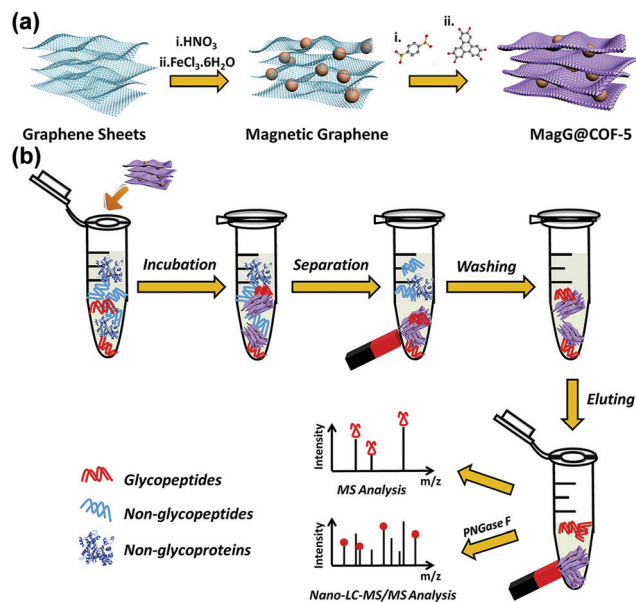


Fig. 33 (a) Synthesis of the MagG@COF-5 biocomposite. (b) Flow chart of the recognition process for *N*-linked glycopeptides by using the MagG@COF-5 biocomposite.<sup>391</sup> Adapted with permission from ref. 391. Copyright 2017, Royal Society of Chemistry.

Combining carefully engineered size-exclusion effect and binding sites introduced through functionalization can provide potential solutions for the selectivity issue. Secondly, most of the reported COFs are highly hydrophobic which can lead to weak adhesion between the sample media and COFs and slow adsorption kinetics. The development of new COFs with well-controlled surface chemistry and channel environment will lead to superior adsorption ability for hydrophilic compounds in aqueous and biological samples. Thirdly, COFs should also be chosen or designed by balancing the feasibility of adsorption and desorption during the SPE process. A COF with a strong affinity to a certain analyte may show higher extraction efficiency, but may lead to incomplete desorption in the subsequent procedure which can affect the accuracy of quantitative analysis. Furthermore, the combination of COFs with other functional materials and substrates may further enhance their adsorption capacity and chemical stability and reduce the cost, and eventually expand the application of COFs as effective adsorbents in sample treatment for analyte detection.

## 2.5 Detection based on other mechanisms

**2.5.1 Surface-enhanced Raman scattering.** Surface-enhanced Raman spectroscopy (SERS) is a surface-sensitive technique that enhances Raman scattering by molecules adsorbed on rough metal surfaces or by nanostructures.<sup>403</sup> As the enhancement factors can be up to  $10^{10}$  to  $10^{11}$ , SERS could be used as a powerful tool for detection with rapid response and highly informative fingerprints.<sup>404,405</sup> Although the exact mechanism of the enhancement effect of SERS is still under debate, it is generally believed that the enhanced Raman scattering is due to the plasmonic electromagnetic fields generated at or near the nanostructured

surface and charge-transfer states produced between the metal and adsorbents.<sup>406,407</sup> The SPR enhancement effect decays exponentially as a function of distance from the nanoparticles. A close proximity of target analytes to the metal surface is mandatory for analysis by SERS. However, the poor affinity of the target analyte to the metallic nanostructures is a matter of concern. The functionalization of metal surfaces has become a potential way to improve the affinity of a specific analyte to the metal surface.

COFs can be rationally designed to exhibit excellent adsorption capability and high affinity to a series of targets, making them potential candidates for composing hybrid substrates for SERS-based detection. Long and coworkers developed a SERS substrate for the recognition of polycyclic aromatic hydrocarbons with high sensitivity by using COF SNW-1 (Fig. 34a).<sup>408</sup> Unlike most SERS substrates made of metal NP decorated hybrids, the Au NPs/SNW-1 nanocomposite with well-controlled particle size and fine-tuned morphology could be fabricated based on rapid physisorption of Au NPs to abundant nitrogen atoms present in SNW-1. Diverse PAHs and their mixtures, including acenaphthene, phenanthrene, anthracene, fluoranthene, pyrene, benzo[*a*]anthracene, 3,4-benzopyrene, and coronene, could be analyzed by using the developed substrate with high sensitivity and reproducibility. The characteristic Raman signature could be obtained from the PAHs even down to a concentration of tens of nM, and the corresponding LOD for each of the eight target PAHs was down to  $10^{-7}$  to  $10^{-8}$  M (Fig. 34b and c). The developed substrate of Au NPs/SNW-1 could be further applied in the SERS analysis of real samples of local tap and pond water with recovery for all the spiked PAHs ranging from 80 to 114%.<sup>408</sup>

**2.5.2 Laser desorption/ionization mass spectrometry.** Laser desorption/ionization time-of-flight mass spectrometry (LDI-TOF MS) is widely used for the analysis of proteins and other biological macromolecules because of its advantages such as rapid analysis, ease of use, and soft ionization.<sup>409</sup> However, it is still challenging to use LDI-TOF-MS for the analysis of small molecules, because of the significant suppression and overlap of the analyte signal by the commonly used matrix and crystallization of analytes in matrices that interfere with the quantitative analysis.<sup>410–412</sup> Nanomaterials, like porous silicon,<sup>412</sup> metal/metal oxide nanoparticles,<sup>413</sup> and graphene,<sup>414</sup> have been applied as the matrix in LDI-TOF MS analysis to realize low interference background and high desorption/ionization efficiency, because they usually possess aromatic rings or oxygenated functional groups that can promote the ionization process between analytes and matrices and prevent aggregation of target molecules. Considering that plenty of aromatic systems and hydroxyl or amino groups also generally exist in COFs, it is anticipated that COFs can serve as promising alternative matrices for LDI-TOF MS for small molecule detection.

Xia and coworkers reported the first example of using a COF as a matrix for LDI-TOF MS,<sup>415</sup> in which COF TpBD was used to demonstrate the proof-of-concept.<sup>416</sup> Biological molecules, such as amino acids and fatty acids, as well as environmental pollutants, like bisphenol S (BPS) and pyrene, were successfully detected. This method achieved higher desorption/ionization







Table 5 Summary of detection based on extraction coupled with chromatography and spectrometry using COFs

Analyte(s)	Method	COF	Detection architecture	LOD	Detection range	Other detection parameters	Ref.
Sudan dyes	Micro-solid-phase extraction (MSPE)/HPLC	HL-COP	HL-COP/SSF column	0.03–0.15 $\mu\text{g L}^{-1}$	0.5–100 $\mu\text{g L}^{-1}$	pH = 7.0, extraction flow rate of 300 $\mu\text{L min}^{-1}$ , desorption flow rate of 200 $\mu\text{L min}^{-1}$ and desorption flow volume of 600 $\mu\text{L}$ ; chili powder, sausage samples, recoveries 73.8–112.6%	351
Pyrethroids	SPME/GC	A hydrazone COF	COF/PDA-SSF	0.11 to 0.23 $\mu\text{g kg}^{-1}$	1–1000 $\mu\text{g kg}^{-1}$	Extraction temperature of 50 $^{\circ}\text{C}$ , extraction time of 30 min, and desorption time of 2 min; vegetables and fruits, recoveries 75.6–106.3%	377
Paclitaxel	Magnetic SPME/HPLC	COF-1	$\text{Fe}_3\text{O}_4/\text{COF-1}$	0.02 $\text{ng mL}^{-1}$	0.1–200 $\text{mL}^{-1}$	pH = 9, acetonitrile content of 0.5% (v/v), extraction time of 1 h, sample volume of 20 mL; rat plasma sample, recovery 99.4–103.7%	384
Phosphopeptides	SPE/MALDI-TOF	TpPa-2	TpPa-2- $\text{Ti}^{4+}$	4 fmol	N/A	200 $\mu\text{L}$ of buffer (50% extraction- $\text{H}_2\text{O}$ , 1% TFA) for 30 min, eluted with 5% $\text{NH}_4\text{OH}$ for 5 min; $\beta$ -casein : BSA = 1 : 100; non-fat milk and HeLa cells	385
Benzophenones	SPME/HPLC	COF-SH	COF-SH@poly(GMA-EDMA)	0.4–0.7 $\text{ng mL}^{-1}$	1–500 $\text{ng mL}^{-1}$	pH = 3.0, eluent MeOH flow rate 0.03 $\text{mL min}^{-1}$ ; urine and serum specimens	352
N-Linked glycopeptide	Magnetic SPE/LC-MS	COF-5	Magnetic graphene (MagG)@COF-5	0.5 fmol $\mu\text{L}^{-1}$	0.5–100 fmol $\mu\text{L}^{-1}$	Extraction solvent $\text{H}_2\text{O}/\text{TFA}$ (95 : 4 : 1, v/v/v), extraction time 15 min; digests/BSA, 1 : 600; human serum	391
PAHs	Magnetic SPE/HPLC	COF-LZU1	COF-LZU1@PEI@ $\text{Fe}_3\text{O}_4$	0.2–20 $\text{pg mL}^{-1}$	2–2000 $\text{pg mL}^{-1}$	pH = 9.0, acetonitrile content of 1%, extraction time 30 min, sample volume 20 mL; environmental samples, recoveries 85.1–107.8%	353
Phthalate esters	Magnetic SPE/GC	CTF	CTFs/Ni	0.024–0.085 $\text{mg kg}^{-1}$	0.08–80 $\text{mg kg}^{-1}$	pH = 7, NaCl (3%, m/v), desorption time 5 min; extraction time 5 min, desorption time 5 min; plastic cup and mineral water bottle	354
Volatile benzene homologues	SPME/GC	COF-SCU1	COF-SCU1/SSW	0.03–0.15 $\text{ng L}^{-1}$	0.1 to 100 $\text{ng L}^{-1}$	Extraction time 20 min, temperature 40 $^{\circ}\text{C}$ , desorption temperature 250 $^{\circ}\text{C}$ for 3 min; indoor air samples, recoveries 87.9–103.4%	355
Bisphenols	Magnetic SPE/LC-MS	TAPB-TPA	$\text{Fe}_3\text{O}_4/\text{TAPB-TPA}$	1.0–78.1 $\text{ng L}^{-1}$	0.1–50 $\text{ng L}^{-1}$	Extraction time 10 min, desorption solvent i-propanol; human serum sample, recoveries 93.0–107.8%	356
Cyano pyrethroids	SPE-HPLC	TAPB-TP	Molecularly imprinted TAPB-TP	0.011–0.018 $\text{ng g}^{-1}$	0.1–200 $\text{ng g}^{-1}$	Desorption solvent 4% acetic acid in methanol; fruit, vegetable, and medicine samples, recoveries 4.3–102.7%	378
OH-PCBs	Magnetic SPE/LC-MS	COF-COOH	$\text{Fe}_3\text{O}_4/\text{COF-apartamers}$	2.1 $\text{pg mL}^{-1}$	0.01–40 $\text{ng mL}^{-1}$	pH = 11, extraction time 30 min, human serum, recoveries > 90%	357
PAHs	Magnetic SPE/HPLC	TpBD	$\text{Fe}_3\text{O}_4/\text{TpBD}$	0.83–11.7 $\text{ng L}^{-1}$	1–100 $\text{ng mL}^{-1}$	Extraction time 12 min, eluent acetonitrile, desorption time 15 min; food samples, recoveries 84–99%	358
Endocrine disruptors	Magnetic SPE/HPLC	TpBD	$\text{Fe}_3\text{O}_4/\text{TpBD}$	1.4–8.7 $\mu\text{g L}^{-1}$	10–1000 $\mu\text{g L}^{-1}$	Eluent acetonitrile, adsorption time 5 min, desorption time 10 min; food samples, recoveries 89.6–108.9%	359
Metal ions	SPE/ICP-MS	TpBD	TpBD	2.1–21.6 $\text{ng L}^{-1}$	0.05–25 $\mu\text{g L}^{-1}$	pH = 5.0, eluent 0.7 M $\text{HNO}_3$ ; environmental and food samples, recoveries over 85%	383
Phenolic pollutants	Magnetic SPE/LC	CTF	CTFs/ $\text{Fe}_2\text{O}_3$	0.09–0.53 $\text{ng mL}^{-1}$	25–2000 $\text{ng mL}^{-1}$	pH = 2, eluent acetonitrile, extraction time 30 min; real water samples, recoveries 85.5–97.7%	360
Perfluorinated compounds	Magnetic SPE/LC	CTF	CTFs/ $\text{Fe}_2\text{O}_3$	0.62–1.39 $\text{ng L}^{-1}$	5–4000 $\text{ng L}^{-1}$	Eluent acetone; environmental water samples, recoveries 87–106%	361
Parabens	Magnetic SPE/HPLC	CTF	$\text{Fe}_3\text{O}_4/\text{CTF}$	0.02 $\mu\text{g L}^{-1}$	0.1–500 $\mu\text{g L}^{-1}$	pH = 7.0, eluent methanol-acetonitrile (v/v = 1 : 1), desorption time 30 s; milk and water samples, recoveries 86–102%	362



Table 5 (continued)

Analyte(s)	Method	COF	Detection architecture	LOD	Detection range	Other detection parameters	Ref.
PAHs	Magnetic SPE/HPLC	TpDA	Fe <sub>3</sub> O <sub>4</sub> @TpDA	0.03–0.73 mg L <sup>-1</sup>	5–100 µg L <sup>-1</sup>	Extraction solvent acetonitrile, adsorption time 10 min, desorption time 15 min; oil and meat sample, recoveries 85.5–104.2%	363
Pesticides	SPE/HPLC	DAAQ-TFP	DAAQ-TFP	0.02–0.08 ng mL <sup>-1</sup>	0.1–160 ng mL <sup>-1</sup>	pH = 2–8, 0.2 mL acetonitrile as the eluent with a pre-soaking time of 1 min; water and drink sample, recoveries 85.5–112.7%	379
Pesticides	SPME/GC	TpPaNO <sub>2</sub>	TpPaNO <sub>2</sub> /stainless steel wire	0.04–0.25 µg kg <sup>-1</sup>	0.5–225 µg kg <sup>-1</sup>	Extraction time 45 min, pH = 6–7, desorption at 260 °C for 6 min; vegetable and fruit samples, recoveries 81.5–111%	380
Polychlorinated biphenyls	Headspace sorptive extraction/GC-MS	TAPB-PDA	Fe <sub>3</sub> O <sub>4</sub> @mTiO <sub>2</sub> @TAPB-PDA	< 0.06 ng g <sup>-1</sup>	0.01–100 ng g <sup>-1</sup>	Soil samples, recoveries 94.6–97.2%	364
Benzoylurea insecticides	SPE/HPLC	TpAzo	TpAzo	0.1–0.2 ng mL <sup>-1</sup>	1.0–160.0 ng mL <sup>-1</sup>	pH = 3–6, eluent acetonitrile; drink and vegetable sample, recoveries 84–108%	381
Sulfonamide antibiotics	SPE/HPLC	COF made of melamine and phthalaldehyde	COF/polyurethanes	0.004–1.050 µg kg <sup>-1</sup>	0.25–1000 ng kg <sup>-1</sup>	pH = 4, eluent methanol; recoveries 82.7–100.8%	386
Chlorophenols	SPME/GC-MS	TpBD	TpBD/stainless steel wire	0.3–1.8 µg kg <sup>-1</sup>	3–300 µg kg <sup>-1</sup>	pH = 11, extraction temperature 40 °C, extraction time 35 min, desorption temperature of 250 °C; food samples, recoveries 70.2–113%	376
Fluorescent whitening agents	SPE/HPLC	COP	Fe <sub>3</sub> O <sub>4</sub> /COF	0.1 ng L <sup>-1</sup>	0.5–100 ng L <sup>-1</sup>	Extraction time 50 min, eluent acetone, elution time 60 min; cosmetic samples, recoveries 8.2–105%	365
Phthalate ester	Magnetic SPE/GC-MS	TpBD	Fe <sub>3</sub> O <sub>4</sub> @PDA@TpBD	0.0025–0.01 ng mL <sup>-1</sup>	50–8000 ng mL <sup>-1</sup>	pH = 7, extraction time 30 min, eluent acetone, desorption time 10 min; human plasma sample, recoveries 92.3–98.9%	375
Phenols	SPE/HPLC	TpBD	Fe <sub>3</sub> O <sub>4</sub> @TpBD	0.08–0.21 ng mL <sup>-1</sup>	0.5–1000 ng mL <sup>-1</sup>	pH = 6, extraction time, 30 min; drink samples, recoveries 81.3–118.0%	366
Phosphopeptides	SPE/MS	TPb-DHBD	Magnetic colloid nano-crystal cluster@TPb-DHBD@Zr <sup>4+</sup>	10 fmol	N/A	Milk and human serum	387
Tetrabromobisphenol A	SPME/MS	TpBD	TpBD/glass fiber	0.92 ng L <sup>-1</sup>	0.01–10 µg L <sup>-1</sup>	Water samples, recoveries 83.9–113.1%	367
cis-Diol-containing compounds	SPE/MALDI-TOF	TpBD	Boric-acid functionalized TpBD	0.01–0.5 pg mL <sup>-1</sup>	0.1–200 pg mL <sup>-1</sup>	pH = 8.0, extraction time 80 min; human serum samples, recoveries 85.3–109%	368
Nonsteroidal anti-inflammatory drugs	SPE/HPLC	TpBD	TpBD@SiO <sub>2</sub>	0.38–2.92 µg L <sup>-1</sup>	0.002–1.0 µg mL <sup>-1</sup>	pH = 2, eluent methanol (1% NH <sub>3</sub> ·H <sub>2</sub> O), desorption time 10 min; water samples, recoveries 77.3–111.6%	388
Pesticides	Magnetic SPE/HPLC	TRI-TER	TRI-TER@Fe <sub>3</sub> O <sub>4</sub>	0.4–1.2 ng L <sup>-1</sup>	5–20 000 ng L <sup>-1</sup>	Extraction time 40 min, eluent acetone, desorption time 5 min; fruit samples, recoveries 73–103%	382
Sulfonamide	Magnetic SPE/HPLC	TpBD	Fe <sub>3</sub> O <sub>4</sub> @TpBD	0.28–1.45 mg L <sup>-1</sup>	1–80 µg L <sup>-1</sup>	Eluent acetone; food samples, recoveries 82–94%	389
Phenols	SPME/GC-MS	PB-DMTP-COF	PB-DMTP-COF-coated fiber	0.0048–0.015 ng L <sup>-1</sup>	0.05–1000 ng L <sup>-1</sup>	Extraction time 60 min, 50 °C, pH = 6, desorption temperature 280 °C; water samples, recoveries 81.3–116.3%	369
Polybrominated diphenyl ethers	SPME/GC-MS	TpPa-1	TpPa-1 coated fiber	0.0058–0.022 ng L <sup>-1</sup>	0.01–100 ng L <sup>-1</sup>	Extraction time 40 min, extraction temperature 70 °C, desorption temperature 300 °C; water samples, recoveries 71.9–125.4%	370
Phthalate esters	Magnetic SPE/GC-MS	TbBd	magG@PDA@TbBd	0.004–0.02 ng mL <sup>-1</sup>	50–8000 ng mL <sup>-1</sup>	pH = 7, extraction time 10 min, eluent dichloromethane, desorption time 10 min; milk samples, recoveries 91.4–108.5%	371

Table 5 (continued)

Analyte(s)	Method	COF	Detection architecture	LOD	Detection range	Other detection parameters	Ref.
PAHs	SPME/GC-MS/MS	TpBD	TpBD/stainless steel wire	0.02–1.66 ng L <sup>-1</sup>	2–200 ng L <sup>-1</sup>	Extraction time, 30 min; desorption time, 5 min; extraction temperature, 40 °C; meat sample, recoveries 85.1–102.8%	372
Chemical warfare agents	SPE/GC-MS and NMR	CTF	CTF	0.010–0.100 µg mL <sup>-1</sup>	0.040–20.0 µg mL <sup>-1</sup>	Eluent DCM, CHCl <sub>3</sub> , and EtOAc; recoveries 87–100%	24
Fluorochemicals	SPE/SALDI-TOF MS	COF-LZU1	COF-LZU1	0.016–0.67 ng mL <sup>-1</sup>	10–2000 pg mL <sup>-1</sup>	pH = 3; selectivity over humic acid; real water samples, recoveries 77.1–123%	373
Allergenic disperse dyes	Magnetic SPE/LC-MS/MS	N-Mag-COF	N-Mag-COF	0.021–0.58 µg kg <sup>-1</sup>	0.5–50 µg kg <sup>-1</sup>	Extraction solvent methanol, extraction time 10 min; textile samples, recoveries 72.2–107%	374
Sulfonamides	SPE/HPLC	SNW-1	SNW-1@PAN	1.7–2.7 ng mL <sup>-1</sup>	5–125 ng mL <sup>-1</sup>	pH = 5–7, eluent 5% ammonia-methanol; metal samples, recoveries 86–111%	390
Hsp90α	Magnetic SPE/MS	TpBD	Fe <sub>3</sub> O <sub>4</sub> @TpBD-DSS-Ab-ME	50 pg mL <sup>-1</sup>	N/A	pH = 6.0; human plasma samples, selectivity: Hsp90α : BSA = 1 : 1000	392

efficiency and less background interference than when using the conventional organic matrices. It exhibited good salt tolerance (500 mM NaCl) and repeatability, and the detection limit of amino acids reached 90 fmol. When this COF matrix was used for amino acid analysis in the honey sample, a recovery of  $97 \pm 3\%$  was achieved.<sup>415</sup> The authors hypothesized that the good performance of COF TpBD as the matrix for LDI-TOF MS originated from its unique structure. The  $\pi$ -conjugated structure may play an important role in assisting the desorption/ionization process because laser adsorption and energy transfer strongly depend on the continuous  $\pi$ -stacking structure. Moreover, the hydroxyl groups of TpBD can enhance the desorption/ionization effects. The conjugated and nanoporous structure of TpBD can also inhibit the production of matrix fragment peaks and prevent target molecules from aggregation, which may effectively accelerate the desorption process from TpBD. Therefore, the unique structure of TpBD resulted in highly efficient transfer of laser energy to small molecules, leading to productive and stable ion intensities.<sup>415</sup>

**2.5.3 Quartz crystal microbalance.** Quartz crystal microbalance (QCM)-based detection is a powerful and well-established noninvasive tool for quantification and online monitoring of chemicals and biomolecules in gas phase and liquid phase. In QCM-based detection, the change in the oscillating frequency of the crystal is directly related to the change of mass on the recognition layer of the quartz.<sup>418,419</sup> Therefore, the sensitivity and selectivity of QCM-based sensors depend on the immobilization of the recognition layer. Molecularly imprinted polymers have long been employed to combine with QCM to construct sensing platforms; however, they may lack

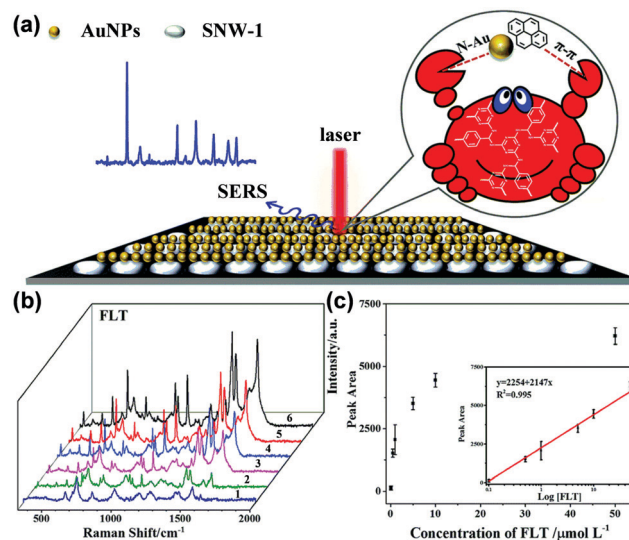


Fig. 34 (a) PAHs in close proximity to Au NPs in the nanohybrids of Au NPs/SNW-1. (b) Raman spectra by using Au NPs/SNW-1 as the SERS substrate obtained from FLT at 0.1, 0.5, 1.0, 5.0, 10.0 and 50.0 mM (1–6), respectively. (c) Scatter plots of peak areas of SERS spectra at 1100 cm<sup>-1</sup> versus the concentrations of FLT. Inset: Calibration curve of the peak areas of Raman spectra versus the logarithm of the concentration of FLT.<sup>408</sup> Adapted with permission from ref. 408. Copyright 2017, Royal Society of Chemistry.



enough valid recognition sites due to their very dense structure.<sup>420</sup> To overcome this limitation, Wang *et al.* demonstrated the use of a QCM sensor based on the gold nanoparticle (Au NP) doped molecularly imprinted layer and COF composite (COFs-Au NPs) for the detection of aflatoxin B1.<sup>421</sup> The three-dimensional Au NP doped molecularly imprinted layer possessed specific recognition ability towards aflatoxin B1. COF CTpBD and Au NPs were employed jointly to yield the COFs-Au NPs composite, in which the COF was used as a scaffold for providing a large surface area for *o*-ATP@Au NPs crosslinking. The introduction of the COFs-Au NPs substrate and the three-dimensional structure of the imprinted matrix endowed the sensor with more accessible recognition sites than that with the molecularly imprinted layer alone. Under optimal conditions, the sensor showed a wide linear range from 0.05 to 75 ng mL<sup>-1</sup>, a low LOD of 2.8 pg mL<sup>-1</sup>, and acceptable recoveries of 87.0–101.7% for real sample analysis.

To enhance the sensitivity and selectivity of the detection, Zhang and coworkers utilized COF BABE-TFPy which contains abundant and accessible –NH and –OH functionalities in channels (Fig. 35a) as the coating layer of a QCM sensor for various VOCs and a mustard gas simulant, 2-chloroethyl ethyl sulfide (CEES).<sup>417</sup> The functional groups in the COF can

facilitate the interaction with guest molecules through hydrogen bonding. The frequency changes of the COF coated QCM sensor were linearly related to the concentrations of CEES vapor within the range of 5.6–19.7 ppm, and the sensor could achieve a low LOD of 0.96 ppm (Fig. 35b). The BABE-TFPy coated QCM sensor displayed significantly higher sensitivity to CEES vapor compared to other common VOCs, even when the concentration of the CEES vapor was much lower than that of the other vapors (Fig. 35c). Theoretical calculations further showed that this good selectivity and sensitivity may be ascribed to the formation of dual-hydrogen bonding interactions between the CEES molecule and the backbone of the BABE-TFPy COF (Fig. 35d).<sup>417</sup>

Constructing heterostructures with advanced architecture is an effective strategy for enhancing the crystallinity and functional performance of COFs. Xu and coworkers reported MOF/COF heterostructure MOF-GC@COF with ZIF-67 derived graphitic carbon (MOF-GC) as the core and COF-TFP-DMPA as the shell for highly sensitive and selective sensing of formaldehyde vapor.<sup>422</sup> The pristine MOF-GC exhibited poor adsorption selectivity toward HCHO vapor. The pristine COF-TFP-DMPA showed high selectivity to HCHO compared to other vapors;

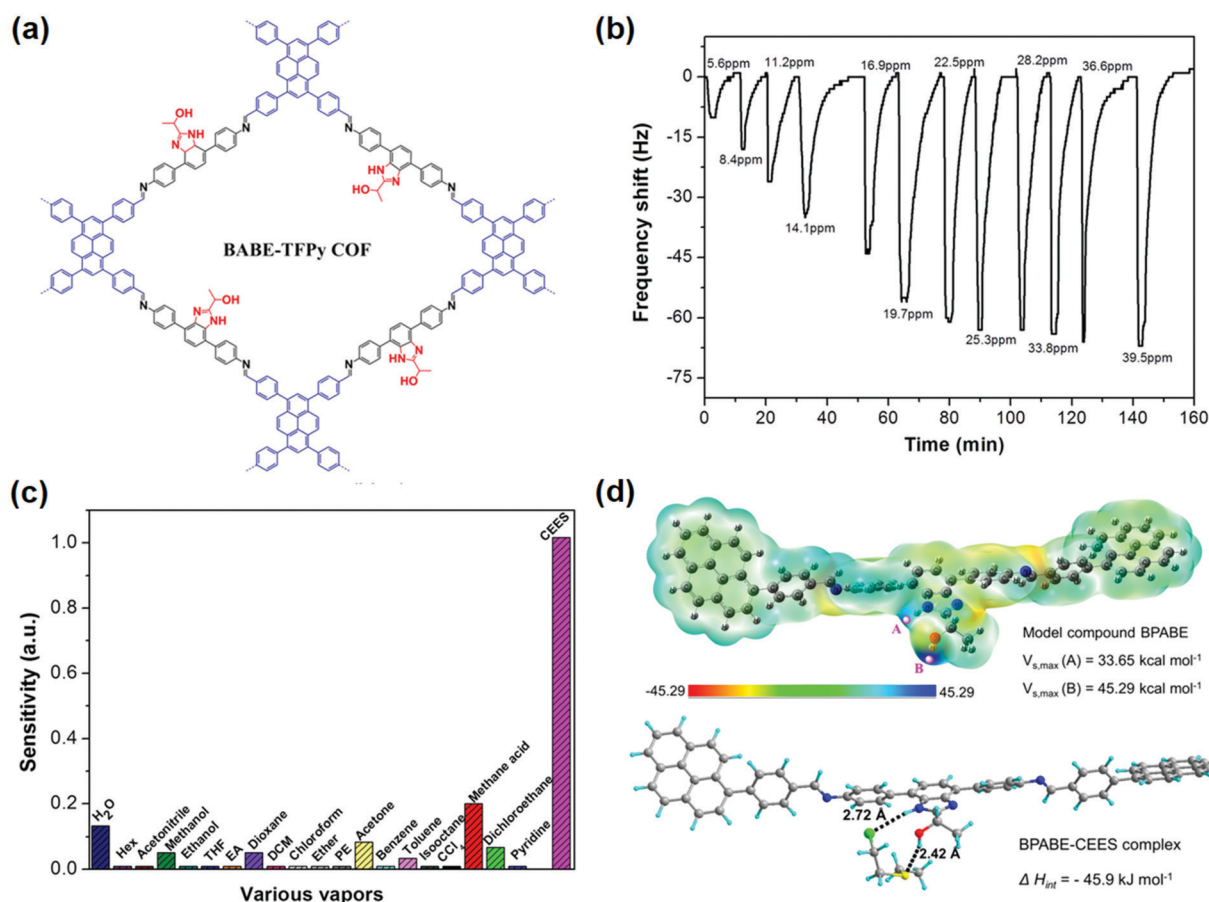


**Fig. 35** (a) Chemical structure of the BABE-TFPy COF. (b) The dynamic response curve of the BABE-TFPy coated QCM sensor exposed to CEES vapor with increasing concentration at 40 °C. (c) Frequency change of the BABE-TFPy coated QCM sensor in response to various vapors. (d) Electrostatic potential of the model compound BPABE for the BABE-TFPy COF and optimized geometries of the dual-hydrogen bonding between the model compound BPABE and the CEES molecule.<sup>417</sup> Adapted with permission from ref. 417. Copyright 2019, American Chemical Society.



however, it suffered from low sensing dynamics. The response dynamics and sensitivity of the heterostructure can be balanced through the tuning of the core/shell ratio. The authors hypothesized that MOF-GC possessing excellent electrical properties and ultrahigh carrier mobility was favorable to promote the free transfer of electrons and for rapid adsorption kinetics, while the COF shell with abundant  $-NH-$  functional groups provided selective hydrogen bonding interactions with the aldehyde groups present in HCHO. In addition, the core-shell motif can help prevent the aggregation of MOF-GC cores and promote the formation of hierarchical porosity, which may facilitate effective adsorption and diffusion of gas molecules. Therefore, the MOF-GC@COF heterostructure with the optimized ratio showed a high QCM sensing response toward HCHO, with a pseudo-first-order rate constant of  $1.026 \text{ min}^{-1}$ , a remarkable detection sensitivity of  $151.8 \text{ Hz ppm}^{-1}$ , and a superior selectivity over a few other vapors, including formic acid, water, ammonia, *etc.*<sup>422</sup>

### 3. Conclusion and perspectives

Recent efforts dedicated to the design and synthesis of robust, stable, ordered and highly accessible porous COFs, the chemical modifications of COFs,<sup>47,80</sup> as well as the fundamental understanding of their physical and chemical properties have paved the way for their applications in chemical detection.<sup>68,69,97,125,400,402</sup> COFs as an emerging group of multifunctional materials have been utilized in advancing chemical detection of a relatively broad range of analytes in various media and scenarios. In the demonstrated examples of chemical detection, COFs have played multifaceted roles, including as recognition units for analyte binding, as transducers for transforming the analyte binding event to optical or electrical signals, as scaffolds for supporting other responsive materials, and/or as selective and efficient adsorbents for preconcentration prior to instrumental analysis. These properties are attributed to the unique features of COFs, including an ordered and porous structure, large surface areas, abundant functional groups, a stable skeleton, high structural tunability and functionalization capability, and engineerable optical and electronic properties.

In this review, we have summarized the progress in the use of COFs, including COFs with post-synthetic modifications and COF-based composites (*e.g.*, COFs-metal nanoparticles, COFs-polymers, COFs-MOFs, and COFs-enzyme composites) for the detection of volatiles and gases, ions, and biomolecules, the selective and sensitive detection, which is of importance in public safety, health care, disease diagnosis, and environmental monitoring and protection. We have discussed the key advances in the application of COFs in chemical detection based on different analytical mechanisms that have been divided into detection based on chromism, fluorescence, electrochemistry, extraction coupled with chromatography and spectrometry, and other detection modes. We have also described each detection mechanism and correlated the role of COFs in these distinct

detection modes with their unique structural features by the analysis and comparison of their structure-property-performance relationships. In doing so, we have aimed to demonstrate how the structural and compositional features of COF-based materials endow them with different optical, electrochemical, electronic, and other chemical and physical properties, and ultimately lead to fascinating and featured applications in the development of chemical detection.

The detection of specific analytes using COFs under different detection methods is summarized in Tables 2–5 by giving the key detection parameters. From these summaries, it is apparent that optical detection, including using chromism and fluorescence change, is the most studied detection mode for volatiles, gases, and ions. Especially, fluorescence-based detection has been proven to be useful in detecting nitro-aromatic explosives with reasonable sensitivity. The optical method can usually provide the advantages of signal visibility, fast response, and good sensitivity for on-site detection. Compared with the optical method, the electrochemical method is currently a powerful tool employed in the detection of biologically important analytes. Electrodes modified with COFs and COF-based nanocomposites have achieved sensitivity with LODs down to the level of nmol to fmol  $\text{L}^{-1}$ , selectivity over a wide range of interferents, and excellent reliability, which is poised for accurate biological analysis and disease diagnostics. SPE coupled with chromatography and spectrometry exhibited capability and robustness for the detection of a broader range of chemicals, ranging from industrial chemicals, ions, drug molecules, to biomolecules. This approach has been successfully applied in real sample analysis, including various food, water, environmental, and biological samples. Some new detection methods, such as SERS, QCM, and chemiresistive detection, have also emerged. The application of these techniques to COF-based analysis brings about the advantages of ultra-low detection limits, high selectivity, and simple and easy detection configurations, and provides on-demand choices for the analysis of specific detection scenarios.

There are several general conceptual and experimental approaches we can learn from these advances that have been proven to be effective for improving the sensitivity, selectivity, response time, and durability of the devices. First, the designability and bottom-up access of COFs can be fully harnessed to introduce specific functional active sites that can interact with target analytes effectively and specifically to realize desired sensitivity and selectivity. As a supplementary strategy, post-synthetic modification has also been proven to be useful in incorporating active sites necessary for host-guest interactions. Second, the engineering of pore size and geometry is an important way of achieving selectivity. Size exclusivity is perhaps the most intuitive selection rule for the recognition of small molecules/ions from biomacromolecular interferents. Thus, the pore size is an important parameter to consider when designing COFs for electrochemical detection or as adsorbents for the preconcentration of analytes. Third, COFs can combine with other nanomaterials (*e.g.*, nanoparticles, SWCNT, and QDs) to form synergistic composites to significantly



enhance the analyte recognition, catalytic ability, redox activity, and/or conductivity of the detection system, leading to improved detection capability and performance. Fourth, compared with bulk forms of COFs, thin sheets of COFs have an enhanced surface-to-volume ratio, more accessible surface functional groups, and superior optical and electronic properties. The use of COFs in the form of thin sheets can, therefore, improve the detection performance.

Although some intriguing developments have been made, the application of COFs in the field of chemical detection is still in early stages of development and critical challenges remain to be addressed to implement COFs in analytical applications. Fluorescence-based detection is currently the most investigated method that is based on the fluorescence change of COFs. Even though various fluorescent building blocks can be integrated into the skeletons of COFs, most of the COF-based materials show weak or no emission in their bulk state due to the so-called ACQ effect. Therefore, current approaches to fluorescence detection rely heavily on the measurement of the emission in the solution phase by preparing a COF suspension or colloid, making it very challenging to be used in real-time analysis. This shortcoming limits their use for direct gas and vapor detection in the gaseous environment by using COFs in their solid-state. Utilizing the AIE mechanism to develop COFs with high emissive ability in their solid-state form may provide an opportunity for easy and on-spot detection. In addition, the turn-on type fluorescence detection is still highly desirable for highly sensitive detection. The progress could be built upon a new level of understanding of emission characteristics of COFs and the interaction mechanism between COFs and analytes, which can be prudently assessed with the assistance of fundamental photophysical mechanisms and principles of supramolecular chemistry coupled with computational calculations<sup>185,187,423,424</sup> and *in situ* spectroscopic techniques.<sup>108</sup>

Electrically transduced detection holds a great opportunity for device miniaturization and integration. COFs have exhibited their potential in the electrically transduced detection of biology-related and gaseous analytes. However, because of limited electrochemical activity and low conductivity, the applications of COFs as sole active electrode materials for electrically transduced detection have been limited. In many cases, COFs are used as scaffolds to combine with metal nanoparticles, conductive matrices, or selectors, to ensure satisfactory detection performance. The dependence on the complex composite structure can bring difficulty in device fabrication and also lead to unpredictable stability issues in the detection process. Fortunately, the great tunability and designability of COFs make it possible to construct COFs that harmoniously integrate the feature of high electrical conductivity, specific active binding sites, and redox-active units, ideally leading to more advanced applications in electrically transduced detection.<sup>78,91,125,309–311,320,323</sup> Moreover, the utilization of conductive COFs for chemiresistive detection has emerged,<sup>91,128</sup> paving the way for the development of other electronic configurations for electrically transduced detection platforms.

As another important aspect of COFs in chemical detection, COFs have acted as effective adsorbents in solid-phase extraction

for complex and trace sample analysis. The experimental parameters for the extraction, including adsorbent dosage, extraction time, pH and ion strength, desorption solvent, and time, can affect the extraction efficiency, and thus need to be examined thoroughly before chromatography and spectrometry analysis. Some of the above procedures can be time-consuming and solvent intensive, and unsuitable for online microfluidic analysis. In this regard, the development of simple, quick, and efficient extraction techniques is urgently needed. Furthermore, the construction of novel COFs with different dimensions, pore geometry, and functional groups could be the key to increase their extraction efficiency and selectivity.

In addition to these challenges for specific detection modes, future directions for chemical detection using COFs also include the development of new strategies to increase the sensitivity and selectivity, the exploration of appropriate methods for the seamless integration of COFs on the substrate or electrode, and the discovery and synthetic access of new COFs with desired properties that can meet the needs of specific detection tasks. The advances of these directions ask for innovations of material design and synthesis, morphological control, and device fabrication by harnessing the useful concepts from reticular chemistry, materials chemistry, supramolecular chemistry, and biochemistry.

Sensitivity and selectivity can be achieved by the combination of the porous structure of COFs and other active components to form stable composite structures. It is known that enzymes have high efficiency and specificity in catalyzing biochemical reactions because of the specific molecular recognition of substrates by enzymes. MOFs have been gaining popularity as platforms for enzyme immobilization for catalysis and sensing,<sup>425</sup> due to flexibility in their structural/chemical design and great surface tunability. Likewise, as the counterpart of MOFs, COFs with ordered structure and tunable pore parameters can provide excellent platforms for enzyme immobilization that can retain the integrity and activity of enzymes and enhance their stability and recyclability.<sup>425,426</sup> Even though most COFs are microporous with pores not large enough to accommodate enzymes, mesoporous COFs with large pores up to a few nanometers have been reported,<sup>427–434</sup> paving the way for the storage of large molecules. Initial investigations on the immobilization of enzymes in mesoporous COFs have revealed excellent enzymatic activity and durability for catalytic reactions.<sup>431–433</sup> Transducing these interactions into the changes in physical and electronic properties of COFs may allow the detection of the participating molecules in these interactions. Therefore, we anticipate that the immobilization of enzymes in mesoporous materials is potentially useful for detection, such as sensing of biologically related analytes, by utilizing the greater number of interaction sites for the analyte molecules provided by encapsulated enzymes.

Reliable methods for interfacing COFs with electrodes or incorporating them into the substrate to generate high-quality electronic devices still need to be developed. Studies on relevant MOF-based materials have shown that thin films can offer the features of fast mass and electron transport, maximized





exposed surface area, and desired mechanical properties. The exploitation of MOF thin films has realized the fabrication of devices with rapid response, ultrasensitivity, transparency, and flexibility for electronic,<sup>435,436</sup> electrochemical, and electromechanical detection.<sup>437</sup> Analogously, the growth of thin COF films with control over the film thickness, morphology, and crystallinity is highly desirable for the fabrication of functional, miniaturized, and portable electronic devices for chemical detection in a low-cost and scalable way.<sup>98</sup> However, COFs are typically synthesized under solvothermal conditions with monomers and intermediate oligomers partially soluble in the reaction solvent.<sup>48</sup> This heterogeneity provides insoluble and unprocessable microcrystalline powder aggregates and usually leads to poor control over the morphology of COFs, as compared to MOFs. Strategic use of the bottom-up principle of COF synthesis and template strategies can offer the opportunity to organize and orient functional  $\pi$ -electron systems into robust periodic structures.<sup>100</sup> Pioneering work by Dichtel and co-workers has enabled the growth of oriented 2D layered COF films on substrate-supported single-layer graphene. Recently, the interface synthesis with the aid of surfactants has been utilized to produce ultrathin COF nanosheets with atomic thickness.<sup>438,439</sup> In addition to growing thin films, a surface deposition strategy has also been used for integrating COFs with other substrates such as melamine foam<sup>440</sup> and capillary columns.<sup>57</sup> The terracotta process<sup>81</sup> and 3D printing technology<sup>441</sup> have also recently been developed for the rapid and facile fabrication of COFs with controlled shape, size, and composition. These advances provide great opportunities for optimizing the procedures from COF synthesis to device fabrication for further exploration in fluorescence, electrochemical, chemiresistive, and chromatography detection.<sup>442</sup>

Continuous efforts towards making full use of the principles of reticular chemistry to precisely integrate functional building blocks to achieve predesigned compositions, components, and properties of COFs are still highly desired.<sup>96</sup> Since the first report of COFs in 2005, the synthesis of the COFs has been rapidly developed and the structural diversity of COFs has greatly expanded, alongside a broadening of the scope of applications of COFs. Nevertheless, control over the growth, defect sites, stacking, and morphology of COFs is still important for establishing precise structure–function correlations. Additionally, computational assessment of COF materials can provide valuable guidance and information for the design, characterization, and property evaluation of COFs.<sup>443,444</sup> The development of new COFs with unprecedented optical, electronic, and magnetic properties, as well as stable chemical structures,<sup>47,97</sup> is expected to provide opportunities for the advancement of currently existing detection modes and give insights into exploring novel mechanisms for chemical detection.<sup>68,69</sup>

## Abbreviation

MEG	2-(2-(2-Methoxyethoxy)ethoxy)ethanamine
CEES	2-Chloroethyl ethyl sulfide

Tetryl	2,4,6-Trinitrophenylmethylnitramine
TNP	2,4,6-Trinitrophenol
TMB	3,3',5,5'-Tetramethylbenzidine
MQCA	3-Methylquinoline-2-carboxylic acid
PEA	$\beta$ -Phenylethylamine
AF	Aflatoxin
ACQ	Aggregation caused quenching
AIE	Aggregation induced emission
AMP	Ampicillin
Ab	Antibody
AA	Ascorbic acid
AB	Aniline
BET	Brunauer–Emmett–Teller
BHb	Bovine hemoglobin
BSA	Bovine serum albumin
CRP	C-Reactive protein
CND	Carbon nanodot
FAM	Carboxyfluorescein
CBX	Carbadox
CEA	Carcinoembryonic antigen
cTnI	Cardiac troponin I
CT	Charge transfer
COF	Covalent organic framework
CONs	Covalent organic nanosheets
COPs	Covalent organic polymers
CV	Cyclic voltammetry
Cys	Cysteine
DON	Deoxynivalenol
DCM	Dichloromethane
DPV	Differential pulse voltammetry
DNP	Dinitrophenol
DNB	Dinitrobenzene
DNT	Dinitrotoluene
ADR	Doxorubicin hydrochloride
EIS	Electrochemical impedance spectroscopy
EET	Electronic energy transfer
ET	Energy transfer
ENR	Enrofloxacin
EtOAc	Ethyl acetate
EGFR	Epidermal growth factor receptor
ESIPT	Excited-state intramolecular proton transfer
FRET	Fluorescence resonance energy transfer
GC	Gas chromatography
Glu	Glutamic acid
GSH	Glutathione
GMA–EDMA	Glycidyl methacrylate–ethylene dimethacrylate
Gly	Glycine
AE	Gold electrode
GO	Graphene oxide
Hsp90 $\alpha$	Heat shock protein 90 $\alpha$
HIS	Histidine
HOMO	Highest occupied molecular orbital
HPLC	High performance liquid chromatography
Hcy	Homocysteine
HCG	Human chorionic gonadotropin
HER2	Human epidermal growth factor receptor 2



HSA	Human serum albumin
HCR	Hybridization chain reaction
HQ	Hydroquinone
OH-PCBs	Hydroxylated polychlorinated biphenyls
IgG	Immunoglobulin G
ICT	Intramolecular charge transfer
IPA	Isopropyl alcohol
Kana	Kanamycin
LOD	Limit of detection
LSV	Linear sweep voltammetry
LUMO	Lowest occupied molecular orbital
MS	Mass spectrometry
MEQ	Mequinox
MLCT	Metal–ligand charge transfer
MOF	Metal–organic framework
MC–LR	Microcystin-LR
MSPE	Micro-solid-phase extraction
MIP	Molecularly imprinted polymer
MUC1	Mucin 1
DMF	<i>N,N</i> -Dimethylmethanamide
NS	Nanosheet
NP	Nanoparticle
NB	Nitrobenzene
Np	Nitrophenol
NT	Nitrotoluene
OTA	Ochratoxin A
OLA	Olaquinox
OTC	Oxytetracycline
PBS	Phosphate-buffered saline
PET	Photo-induced electron transfer
PDGF-BB	Platelet-derived growth factor with two B subunits
PPD	<i>p</i> -Phenylenediamine
PAHs	Polycyclic aromatic hydrocarbons
PDA	Polydopamine
PI	Polyimide
PSA	Prostate specific antigen
QCM	Quartz crystal microbalance
NaAc	Sodium acetate
SPME	Solid-phase microextraction
SWV	Square wave voltammetry
SSF	Stainless steel fiber
SSW	Stainless steel wire
RFP	Streptomycin
SERS	Surface enhanced Raman scattering
SWCNT	Single walled carbon nanotube
DSS	Suberic acid bis( <i>N</i> -hydroxy succinimide ester)
TCNQ	Tetracyanoquinodimethane
Thi	Thionine
3D	Three-dimensional
TOF	Time-of-flight
TOB	Tobramycin
2D	Two-dimensional
TICT	Twisted intramolecular charge transfer
UA	Uric acid
VEGF	Vascular endothelial growth factor
ZEN	Zearalenone

## Conflicts of interest

There are no conflicts to declare.

## Acknowledgements

The authors acknowledge support from startup funds provided by Dartmouth College, Irving Institute for Energy and Society, Army Research Office Young Investigator Program (W911NF-17-1-0398), Sloan Research Fellowship (FG-2018-10561), Camille Dreyfus Teacher-Scholar Award, NSF CAREER Award (#1945218), Maximizing Investigators' Research Award from the National Institutes of Health (R35GM138318), 3M Non-Tenured Faculty Award, and US Army Cold Regions Research & Engineering Lab (W913E519C0008), National Science Foundation EPSCoR award (#1757371).

## Notes and references

- 1 R. A. Potyrailo, *Chem. Rev.*, 2016, **116**, 11877.
- 2 Y. Y. Broza, X. Zhou, M. Yuan, D. Qu, Y. Zheng, R. Vishinkin, M. Khatib, W. Wu and H. Haick, *Chem. Rev.*, 2019, **119**, 11761.
- 3 M. Mayer and A. J. Baeumner, *Chem. Rev.*, 2019, **119**, 7996.
- 4 K. Mitsubayashi, O. Niwa and U. Yuko, *Chemical, Gas, and Biosensors for Internet of Things and Related Applications*, Elsevier Inc, 2019.
- 5 W. Zhang, Y. Tang, A. Shi, L. Bao, Y. Shen, R. Shen and Y. Ye, *Materials*, 2018, **11**, 1364.
- 6 P. R. Haddad, *Ion chromatography-principles and applications*, Elsevier, 1990, pp. 343–385, DOI: 10.1016/s0301-4770(08)61144-6.
- 7 L. A. Ellis and D. J. Roberts, *J. Chromatogr. A*, 1997, **774**, 3.
- 8 G. Guetens, G. De Boeck, M. S. Highley, M. Wood, R. A. A. Maes, A. A. M. Eggermont, A. Hanauske, E. A. de Bruijn and U. R. Tjaden, *J. Chromatogr. A*, 2002, **976**, 239.
- 9 C. L. Wilkins, *Science*, 1983, **222**, 291.
- 10 A. J. Bard and L. R. Faulkner, *Electrochemical Methods: Fundamentals and Applications*, Wiley, 2000.
- 11 D. A. Skoog, F. J. Holler and S. R. Crouch, *Principles of Instrumental Analysis*, Cengage Learning, 2017.
- 12 D. Diamond, S. Coyle, S. Scarmagnani and J. Hayes, *Chem. Rev.*, 2008, **108**, 652.
- 13 S. Joo and R. B. Brown, *Chem. Rev.*, 2008, **108**, 638.
- 14 D. Xiang, X. Wang, C. Jia, T. Lee and X. Guo, *Chem. Rev.*, 2016, **116**, 4318.
- 15 F. Yi, H. Ren, J. Shan, X. Sun, D. Wei and Z. Liu, *Chem. Soc. Rev.*, 2018, **47**, 3152.
- 16 V. A. Aksyuk, *Nat. Nanotechnol.*, 2017, **12**, 940.
- 17 Z. Meng, R. M. Stolz, L. Mendecki and K. A. Mirica, *Chem. Rev.*, 2019, **119**, 478.
- 18 F. Valentini and G. Palleschi, *Anal. Lett.*, 2008, **41**, 479.
- 19 R. Murray, *Anal. Chem.*, 2009, **63**, 493a.
- 20 F. S. Ligler and H. S. White, *Anal. Chem.*, 2013, **85**, 11161.



- 21 F. Schedin, A. K. Geim, S. V. Morozov, E. W. Hill, P. Blake, M. I. Katsnelson and K. S. Novoselov, *Nat. Mater.*, 2007, **6**, 652.
- 22 F.-G. Bănică, *Chemical Sensors and Biosensors*, John Wiley & Sons, Ltd, 2012.
- 23 J. Janata and A. Bezegh, *Anal. Chem.*, 1988, **60**, 62R.
- 24 K. Sinha Roy, D. R. Goud, A. Mazumder, B. Chandra, A. K. Purohit, M. Palit and D. K. Dubey, *ACS Appl. Mater. Interfaces*, 2019, **11**, 16027.
- 25 N. Negreira, M. Lopez de Alda and D. Barcelo, *J. Chromatogr. A*, 2013, **1280**, 64.
- 26 J. Zhang and Z. Chen, *J. Chromatogr. A*, 2017, **1530**, 1.
- 27 D. W. Breck, *Zeolite molecular sieves: structure, chemistry, and use*, Wiley, 1973.
- 28 H. Shirakawa, E. J. Louis, A. G. MacDiarmid, C. K. Chiang and A. J. Heeger, *J. Chem. Soc., Chem. Commun.*, 1977, 578, DOI: 10.1039/c39770000578.
- 29 K. S. Novoselov, A. K. Geim, S. V. Morozov, D. Jiang, Y. Zhang, S. V. Dubonos, I. V. Grigorieva and A. A. Firsov, *Science*, 2004, **306**, 666.
- 30 S. Iijima, *Nature*, 1991, **354**, 56.
- 31 B. F. Hoskins and R. Robson, *J. Am. Chem. Soc.*, 1990, **112**, 1546.
- 32 M. Fujita, Y. J. Kwon, S. Washizu and K. Ogura, *J. Am. Chem. Soc.*, 1994, **116**, 1151.
- 33 O. M. Yaghi and H. Li, *J. Am. Chem. Soc.*, 1995, **117**, 10401.
- 34 F. Yavari and N. Koratkar, *J. Phys. Chem. Lett.*, 2012, **3**, 1746.
- 35 M. Pumera, A. Ambrosi, A. Bonanni, E. L. K. Chng and H. L. Poh, *Trends Anal. Chem.*, 2010, **29**, 954.
- 36 E. Singh, M. Meyyappan and H. S. Nalwa, *ACS Appl. Mater. Interfaces*, 2017, **9**, 34544.
- 37 D. T. McQuade, A. E. Pullen and T. M. Swager, *Chem. Rev.*, 2000, **100**, 2537.
- 38 J. Janata and M. Josowicz, *Nat. Mater.*, 2003, **2**, 19.
- 39 J.-S. Yang and T. M. Swager, *J. Am. Chem. Soc.*, 1998, **120**, 11864.
- 40 J. L. Novotney and W. R. Dichtel, *ACS Macro Lett.*, 2013, **2**, 423.
- 41 J. F. Fennell, Jr., S. F. Liu, J. M. Azzarelli, J. G. Weis, S. Rochat, K. A. Mirica, J. B. Ravensbaek and T. M. Swager, *Angew. Chem., Int. Ed.*, 2016, **55**, 1266.
- 42 D. R. Kauffman and A. Star, *Angew. Chem., Int. Ed.*, 2008, **47**, 6550.
- 43 K. A. Mirica, J. G. Weis, J. M. Schnorr, B. Esser and T. M. Swager, *Angew. Chem., Int. Ed.*, 2012, **51**, 10740.
- 44 J. M. Azzarelli, K. A. Mirica, J. B. Ravensbaek and T. M. Swager, *Proc. Natl. Acad. Sci. U. S. A.*, 2014, **111**, 18162.
- 45 A. P. Cote, A. I. Benin, N. W. Ockwig, M. O'Keeffe, A. J. Matzger and O. M. Yaghi, *Science*, 2005, **310**, 1166.
- 46 K. Geng, T. He, R. Liu, S. Dalapati, K. T. Tan, Z. Li, S. Tao, Y. Gong, Q. Jiang and D. Jiang, *Chem. Rev.*, 2020, **120**, 8814.
- 47 S. Y. Ding and W. Wang, *Chem. Soc. Rev.*, 2013, **42**, 548.
- 48 D. Rodriguez-San-Miguel and F. Zamora, *Chem. Soc. Rev.*, 2019, **48**, 4375.
- 49 G. Garberoglio, *Langmuir*, 2007, **23**, 12154.
- 50 S. S. Han, H. Furukawa, O. M. Yaghi and W. A. Goddard, 3rd, *J. Am. Chem. Soc.*, 2008, **130**, 11580.
- 51 H. Furukawa and O. M. Yaghi, *J. Am. Chem. Soc.*, 2009, **131**, 8875.
- 52 J. L. Mendoza-Cortes, S. S. Han, H. Furukawa, O. M. Yaghi and W. A. Goddard, 3rd, *J. Phys. Chem. A*, 2010, **114**, 10824.
- 53 L. Zhu and Y. B. Zhang, *Molecules*, 2017, **22**, 1149.
- 54 C. X. Yang, C. Liu, Y. M. Cao and X. P. Yan, *Chem. Commun.*, 2015, **51**, 12254.
- 55 H. Xu, X. Chen, J. Gao, J. Lin, M. Addicoat, S. Irle and D. Jiang, *Chem. Commun.*, 2014, **50**, 1292.
- 56 Z. Kang, Y. Peng, Y. Qian, D. Yuan, M. A. Addicoat, T. Heine, Z. Hu, L. Tee, Z. Guo and D. Zhao, *Chem. Mater.*, 2016, **28**, 1277.
- 57 H. L. Qian, C. X. Yang and X. P. Yan, *Nat. Commun.*, 2016, **7**, 12104.
- 58 S. Yuan, X. Li, J. Zhu, G. Zhang, P. Van Puyvelde and B. Van der Bruggen, *Chem. Soc. Rev.*, 2019, **48**, 2665.
- 59 C. Zhang, B. H. Wu, M. Q. Ma, Z. Wang and Z. K. Xu, *Chem. Soc. Rev.*, 2019, **48**, 3811.
- 60 S. Y. Ding, J. Gao, Q. Wang, Y. Zhang, W. G. Song, C. Y. Su and W. Wang, *J. Am. Chem. Soc.*, 2011, **133**, 19816.
- 61 H. Xu, J. Gao and D. Jiang, *Nat. Chem.*, 2015, **7**, 905.
- 62 S. Lin, C. S. Diercks, Y. B. Zhang, N. Kornienko, E. M. Nichols, Y. Zhao, A. R. Paris, D. Kim, P. Yang, O. M. Yaghi and C. J. Chang, *Science*, 2015, **349**, 1208.
- 63 V. S. Vyas, F. Haase, L. Stegbauer, G. Savasci, F. Podjaski, C. Ochsenfeld and B. V. Lotsch, *Nat. Commun.*, 2015, **6**, 8508.
- 64 Q. Fang, S. Gu, J. Zheng, Z. Zhuang, S. Qiu and Y. Yan, *Angew. Chem., Int. Ed.*, 2014, **53**, 2878.
- 65 R. K. Sharma, P. Yadav, M. Yadav, R. Gupta, P. Rana, A. Srivastava, R. Zbořil, R. S. Varma, M. Antonietti and M. B. Gawande, *Mater. Horiz.*, 2019, **7**, 411.
- 66 T. Yang, Y. N. Cui, H. Y. Chen and W. H. Li, *Acta Chim. Sin.*, 2017, **75**, 339.
- 67 T. Wang, R. Xue, Y. L. Wei, M. Y. Wang, H. Guo and W. Yang, *Prog. Chem.*, 2018, **30**, 753.
- 68 X. Liu, D. Huang, C. Lai, G. Zeng, L. Qin, H. Wang, H. Yi, B. Li, S. Liu, M. Zhang, R. Deng, Y. Fu, L. Li, W. Xue and S. Chen, *Chem. Soc. Rev.*, 2019, **48**, 5266.
- 69 X. Zhang, G. Li, D. Wu, B. Zhang, N. Hu, H. Wang, J. Liu and Y. Wu, *Biosens. Bioelectron.*, 2019, **145**, 111699.
- 70 S. Mitra, H. S. Sasmal, T. Kundu, S. Kandambeth, K. Illath, D. Díaz Díaz and R. Banerjee, *J. Am. Chem. Soc.*, 2017, **139**, 4513.
- 71 S. Wan, J. Guo, J. Kim, H. Ihee and D. Jiang, *Angew. Chem., Int. Ed.*, 2008, **47**, 8826.
- 72 M. Dogru and T. Bein, *Chem. Commun.*, 2014, **50**, 5531.
- 73 A. K. Mandal, J. Mahmood and J.-B. Baek, *ChemNanoMat*, 2017, **3**, 373.
- 74 S. Wang, Q. Wang, P. Shao, Y. Han, X. Gao, L. Ma, S. Yuan, X. Ma, J. Zhou, X. Feng and B. Wang, *J. Am. Chem. Soc.*, 2017, **139**, 4258.
- 75 F. Xu, S. Yang, X. Chen, Q. Liu, H. Li, H. Wang, B. Wei and D. Jiang, *Chem. Sci.*, 2019, **10**, 6001.





- 76 S. B. Alahakoon, C. M. Thompson, G. Occhialini and R. A. Smaldone, *ChemSusChem*, 2017, **10**, 2116.
- 77 Z. Lei, Q. Yang, Y. Xu, S. Guo, W. Sun, H. Liu, L. P. Lv, Y. Zhang and Y. Wang, *Nat. Commun.*, 2018, **9**, 576.
- 78 Y. Wu, D. Yan, Z. Zhang, M. M. Matsushita and K. Awaga, *ACS Appl. Mater. Interfaces*, 2019, **11**, 7661.
- 79 Y. Song, Q. Sun, B. Aguila and S. Ma, *Adv. Sci.*, 2019, **6**, 1801410.
- 80 J. L. Segura, S. Royuela and M. Mar Ramos, *Chem. Soc. Rev.*, 2019, **48**, 3903.
- 81 S. Karak, S. Kandambeth, B. P. Biswal, H. S. Sasmal, S. Kumar, P. Pachfule and R. Banerjee, *J. Am. Chem. Soc.*, 2017, **139**, 1856.
- 82 L. A. Baldwin, J. W. Crowe, D. A. Pyles and P. L. McGrier, *J. Am. Chem. Soc.*, 2016, **138**, 15134.
- 83 J. L. C. Rowsell and O. M. Yaghi, *Microporous Mesoporous Mater.*, 2004, **73**, 3.
- 84 N. Stock and S. Biswas, *Chem. Rev.*, 2012, **112**, 933.
- 85 S. Kandambeth, D. B. Shinde, M. K. Panda, B. Lukose, T. Heine and R. Banerjee, *Angew. Chem., Int. Ed.*, 2013, **52**, 13052.
- 86 F. J. Uribe-Romo, C. J. Doonan, H. Furukawa, K. Oisaki and O. M. Yaghi, *J. Am. Chem. Soc.*, 2011, **133**, 11478.
- 87 D. Stewart, D. Antypov, M. S. Dyer, M. J. Pitcher, A. P. Katsoulidis, P. A. Chater, F. Blanc and M. J. Rosseinsky, *Nat. Commun.*, 2017, **8**, 1102.
- 88 S. Kandambeth, A. Mallick, B. Lukose, M. V. Mane, T. Heine and R. Banerjee, *J. Am. Chem. Soc.*, 2012, **134**, 19524.
- 89 X. Li, C. Zhang, S. Cai, X. Lei, V. Altoe, F. Hong, J. J. Urban, J. Ciston, E. M. Chan and Y. Liu, *Nat. Commun.*, 2018, **9**, 2998.
- 90 X. Guan, H. Li, Y. Ma, M. Xue, Q. Fang, Y. Yan, V. Valtchev and S. Qiu, *Nat. Chem.*, 2019, **11**, 587.
- 91 Z. Meng, R. M. Stolz and K. A. Mirica, *J. Am. Chem. Soc.*, 2019, **141**, 11929.
- 92 N. Huang, K. H. Lee, Y. Yue, X. Xu, S. Irle, Q. Jiang and D. Jiang, *Angew. Chem., Int. Ed.*, 2020, **59**, 16587.
- 93 J. Guo, Y. Xu, S. Jin, L. Chen, T. Kaji, Y. Honsho, M. A. Addicoat, J. Kim, A. Saeki, H. Ihee, S. Seki, S. Irle, M. Hiramoto, J. Gao and D. Jiang, *Nat. Commun.*, 2013, **4**, 2736.
- 94 J. R. Hunt, C. J. Doonan, J. D. LeVangie, A. P. Cote and O. M. Yaghi, *J. Am. Chem. Soc.*, 2008, **130**, 11872.
- 95 A. P. Cote, H. M. El-Kaderi, H. Furukawa, J. R. Hunt and O. M. Yaghi, *J. Am. Chem. Soc.*, 2007, **129**, 12914.
- 96 N. Huang, P. Wang and D. Jiang, *Nat. Rev. Mater.*, 2016, **1**, 16068.
- 97 M. S. Lohse and T. Bein, *Adv. Funct. Mater.*, 2018, **28**, 1705553.
- 98 H. Wang, Z. Zeng, P. Xu, L. Li, G. Zeng, R. Xiao, Z. Tang, D. Huang, L. Tang, C. Lai, D. Jiang, Y. Liu, H. Yi, L. Qin, S. Ye, X. Ren and W. Tang, *Chem. Soc. Rev.*, 2019, **48**, 488.
- 99 S. Cao, B. Li, R. Zhu and H. Pang, *Chem. Eng. J.*, 2019, **355**, 602.
- 100 S. Kandambeth, K. Dey and R. Banerjee, *J. Am. Chem. Soc.*, 2019, **141**, 1807.
- 101 X. Deng, Y. S. Fang, S. Lin, Q. Cheng, Q. Y. Liu and X. M. Zhang, *ACS Appl. Mater. Interfaces*, 2017, **9**, 3514.
- 102 T. Skorjanc, D. Shetty, M. A. Olson and A. Trabolsi, *ACS Appl. Mater. Interfaces*, 2019, **11**, 6705.
- 103 D. Gopalakrishnan and W. R. Dichtel, *J. Am. Chem. Soc.*, 2013, **135**, 8357.
- 104 N. N. Sang, C. X. Zhan and D. P. Cao, *J. Mater. Chem. A*, 2015, **3**, 92.
- 105 E. Oezdemir, D. Thirion and C. T. Yavuz, *RSC Adv.*, 2015, **5**, 69010.
- 106 L. Guo, X. F. Zeng and D. P. Cao, *Sens. Actuators, B*, 2016, **226**, 273.
- 107 L. E. Kreno, K. Leong, O. K. Farha, M. Allendorf, R. P. Van Duyne and J. T. Hupp, *Chem. Rev.*, 2012, **112**, 1105.
- 108 Z. Hu, B. J. Deibert and J. Li, *Chem. Soc. Rev.*, 2014, **43**, 5815.
- 109 P. Kumar, A. Deep and K.-H. Kim, *Trends Anal. Chem.*, 2015, **73**, 39.
- 110 W.-T. Koo, J.-S. Jang and I.-D. Kim, *Chem*, 2019, **5**, 1938.
- 111 H.-Y. Li, S.-N. Zhao, S.-Q. Zang and J. Li, *Chem. Soc. Rev.*, 2020, **49**, 6364.
- 112 A. Amini, S. Kazemi and V. Safarifard, *Polyhedron*, 2020, **177**, 114260.
- 113 Ü. Anik, S. Timur and Z. Dursun, *Microchim. Acta*, 2019, **186**, 196.
- 114 Y. Shu, Q. Ye, T. Dai, Q. Xu and X. Hu, *ACS Sens.*, 2021, **6**, 641.
- 115 Y. Cui, Y. Yue, G. Qian and B. Chen, *Chem. Rev.*, 2012, **112**, 1126.
- 116 V. Schroeder, S. Savagatrup, M. He, S. Lin and T. M. Swager, *Chem. Rev.*, 2018, **119**, 599.
- 117 Y. Liu, X. Dong and P. Chen, *Chem. Soc. Rev.*, 2012, **41**, 2283.
- 118 M. A. Carpenter, S. Mathur and A. Kolmakov, *Metal Oxide Nanomaterials for Chemical Sensors*, Springer, New York, NY, 2013.
- 119 C. Wang, L. Yin, L. Zhang, D. Xiang and R. Gao, *Sensors*, 2010, **10**, 2088.
- 120 S. W. Thomas, 3rd, G. D. Joly and T. M. Swager, *Chem. Rev.*, 2007, **107**, 1339.
- 121 P. Bamfield, *Chromic Phenomena*, Royal Society of Chemistry, 2010.
- 122 K. Dimroth, C. Reichardt, T. Siepmann and F. Bohlmann, *Justus Liebigs Ann. Chem.*, 1963, **661**, 1.
- 123 W. Huang, Y. Jiang, X. Li, X. J. Li, J. Y. Wang, Q. Wu and X. K. Liu, *ACS Appl. Mater. Interfaces*, 2013, **5**, 8845.
- 124 S. Jhulki, A. M. Evans, X. L. Hao, M. W. Cooper, C. H. Feriante, J. Leisen, H. Li, D. Lam, M. C. Hersam, S. Barlow, J. L. Bredas, W. R. Dichtel and S. R. Marder, *J. Am. Chem. Soc.*, 2020, **142**, 783.
- 125 H. V. Babu, M. G. M. Bai and M. Rajeswara Rao, *ACS Appl. Mater. Interfaces*, 2019, **11**, 11029.
- 126 L. Ascherl, E. W. Evans, M. Hennemann, D. Di Nuzzo, A. G. Hufnagel, M. Beetz, R. H. Friend, T. Clark, T. Bein and F. Auras, *Nat. Commun.*, 2018, **9**, 3802.
- 127 X. Li, Q. Gao, J. Aneesh, H.-S. Xu, Z. Chen, W. Tang, C. Liu, X. Shi, K. V. Adarsh, Y. Lu and K. P. Loh, *Chem. Mater.*, 2018, **30**, 5743.



- 128 R. Kulkarni, Y. Noda, D. Kumar Barange, Y. S. Kochergin, P. Lyu, B. Balcarova, P. Nachtigall and M. J. Bojdys, *Nat. Commun.*, 2019, **10**, 3228.
- 129 L. Ascherl, E. W. Evans, J. Gorman, S. Orsborne, D. Bessinger, T. Bein, R. H. Friend and F. Auras, *J. Am. Chem. Soc.*, 2019, **141**, 15693.
- 130 J. He, F. J. Xu, J. Hu, S. L. Wang, X. D. Hou and Z. Long, *Microchem. J.*, 2017, **135**, 91.
- 131 J. Wang, X. Yang, T. Wei, J. Bao, Q. Zhu and Z. Dai, *ACS Appl. Bio Mater.*, 2018, **1**, 382.
- 132 Y. Xiong, L. Su, X. He, Z. Duan, Z. Zhang, Z. Chen, W. Xie, D. Zhu and Y. Luo, *Sens. Actuators, B*, 2017, **253**, 384.
- 133 L. J. Su, Z. Zhang and Y. H. Xiong, *Nanoscale*, 2018, **10**, 20120.
- 134 W. R. Cui, C. R. Zhang, W. Jiang, R. P. Liang, S. H. Wen, D. Peng and J. D. Qiu, *ACS Sustainable Chem. Eng.*, 2019, **7**, 9408.
- 135 W. Li, Y. Li, H. L. Qian, X. Zhao, C. X. Yang and X. P. Yan, *Talanta*, 2019, **204**, 224.
- 136 M. Ziolek, J. Kubicki, A. Maciejewski, R. Naskrecki and A. Grabowska, *J. Chem. Phys.*, 2006, **124**, 124518.
- 137 N. Xu, R.-L. Wang, D.-P. Li, Z.-Y. Zhou, T. Zhang, Y.-Z. Xie and Z.-M. Su, *New J. Chem.*, 2018, **42**, 13367.
- 138 N. Popp, T. Homburg, N. Stock and J. Senker, *J. Mater. Chem. A*, 2015, **3**, 18492.
- 139 R. S. Li, H. Z. Zhang, J. Ling, C. Z. Huang and J. Wang, *Appl. Spectrosc. Rev.*, 2015, **51**, 129.
- 140 M. I. Kim, M. S. Kim, M. A. Woo, Y. Ye, K. S. Kang, J. Lee and H. G. Park, *Nanoscale*, 2014, **6**, 1529.
- 141 F. Z. Cui, J. J. Xie, S. Y. Jiang, S. X. Gan, D. L. Ma, R. R. Liang, G. F. Jiang and X. Zhao, *Chem. Commun.*, 2019, **55**, 4550.
- 142 Y. H. Xiong, Y. M. Qin, L. J. Su and F. G. Ye, *Chem. – Eur. J.*, 2017, **23**, 11037.
- 143 B. Valeur and M. r. N. Berberan-Santos, *J. Chem. Educ.*, 2011, **88**, 731.
- 144 M. D. Allendorf, C. A. Bauer, R. K. Bhakta and R. J. Houk, *Chem. Soc. Rev.*, 2009, **38**, 1330.
- 145 G. Blasse and B. C. Grabmaier, *Luminescent Materials*, Springer-Verlag Berlin Heidelberg, 1994.
- 146 G. Feng, G. Q. Zhang and D. Ding, *Chem. Soc. Rev.*, 2020, **49**, 8179.
- 147 J. V. Goodpaster and V. L. McGuffin, *Anal. Chem.*, 2001, **73**, 2004.
- 148 T. M. Swager, *Acc. Chem. Res.*, 1998, **31**, 201.
- 149 S. Singh, *J. Hazard. Mater.*, 2007, **144**, 15.
- 150 J. Li, C. E. Kendig and E. E. Nesterov, *J. Am. Chem. Soc.*, 2007, **129**, 15911.
- 151 J. Wu, W. Liu, J. Ge, H. Zhang and P. Wang, *Chem. Soc. Rev.*, 2011, **40**, 3483.
- 152 A. P. de Silva, T. S. Moody and G. D. Wright, *Analyst*, 2009, **134**, 2385.
- 153 Z. Xu, Y. Xiao, X. Qian, J. Cui and D. Cui, *Org. Lett.*, 2005, **7**, 889.
- 154 L. Fabbri, M. Licchelli, P. Pallavicini, A. Perotti, A. Taglietti and D. Sacchi, *Chem. – Eur. J.*, 1996, **2**, 75.
- 155 S. Sasaki, G. P. C. Drummen and G.-i. Konishi, *J. Mater. Chem. C*, 2016, **4**, 2731.
- 156 G. A. Jones and D. S. Bradshaw, *Front. Phys.*, 2019, **7**, 100.
- 157 J. Liang, Q. L. Nguyen and S. Matsika, *Photochem. Photobiol. Sci.*, 2013, **12**, 1387.
- 158 J. S. Wu, J. H. Zhou, P. F. Wang, X. H. Zhang and S. K. Wu, *Org. Lett.*, 2005, **7**, 2133.
- 159 S. Wan, J. Guo, J. Kim, H. Ihee and D. Jiang, *Angew. Chem., Int. Ed.*, 2009, **48**, 5439.
- 160 S. Dalapati, S. Jin, J. Gao, Y. Xu, A. Nagai and D. Jiang, *J. Am. Chem. Soc.*, 2013, **135**, 17310.
- 161 M. Gao and B. Z. Tang, *ACS Sens.*, 2017, **2**, 1382.
- 162 J. Dong, X. Li, K. Zhang, Y. Di Yuan, Y. Wang, L. Zhai, G. Liu, D. Yuan, J. Jiang and D. Zhao, *J. Am. Chem. Soc.*, 2018, **140**, 19816.
- 163 N. Agmon, *J. Phys. Chem. A*, 2005, **109**, 13.
- 164 S. J. Lim, J. Seo and S. Y. Park, *J. Am. Chem. Soc.*, 2006, **128**, 14542.
- 165 J. Zhao, S. Ji, Y. Chen, H. Guo and P. Yang, *Phys. Chem. Chem. Phys.*, 2012, **14**, 8803.
- 166 J. W. Crowe, L. A. Baldwin and P. L. McGrier, *J. Am. Chem. Soc.*, 2016, **138**, 10120.
- 167 E. L. Spitler, B. T. Koo, J. L. Novotney, J. W. Colson, F. J. Uribe-Romo, G. D. Gutierrez, P. Clancy and W. R. Dichtel, *J. Am. Chem. Soc.*, 2011, **133**, 19416.
- 168 S. Dalapati, C. Gu and D. Jiang, *Small*, 2016, **12**, 6513.
- 169 R. Xue, H. Guo, T. Wang, L. Gong, Y. N. Wang, J. B. Ai, D. D. Huang, H. Q. Chen and W. Yang, *Anal. Methods*, 2017, **9**, 3737.
- 170 D. Y. Chen, C. Liu, J. T. Tang, L. F. Luo and G. P. Yu, *Polym. Chem.*, 2019, **10**, 1168.
- 171 T. Y. Zhou, S. Q. Xu, Q. Wen, Z. F. Pang and X. Zhao, *J. Am. Chem. Soc.*, 2014, **136**, 15885.
- 172 X. Feng, L. Chen, Y. Honsho, O. Saengsawang, L. Liu, L. Wang, A. Saeki, S. Irle, S. Seki, Y. Dong and D. Jiang, *Adv. Mater.*, 2012, **24**, 3026.
- 173 S. Dalapati, E. Q. Jin, M. Addicoat, T. Heine and D. L. Jiang, *J. Am. Chem. Soc.*, 2016, **138**, 5797.
- 174 S. Rochat and T. M. Swager, *ACS Appl. Mater. Interfaces*, 2013, **5**, 4488.
- 175 S. Y. Ding, M. Dong, Y. W. Wang, Y. T. Chen, H. Z. Wang, C. Y. Su and W. Wang, *J. Am. Chem. Soc.*, 2016, **138**, 3031.
- 176 Z. P. Li, Y. W. Zhang, H. Xia, Y. Mu and X. M. Liu, *Chem. Commun.*, 2016, **52**, 6613.
- 177 G. Q. Lin, H. M. Ding, D. Q. Yuan, B. S. Wang and C. Wang, *J. Am. Chem. Soc.*, 2016, **138**, 3302.
- 178 Y. Hong, J. W. Lam and B. Z. Tang, *Chem. Soc. Rev.*, 2011, **40**, 5361.
- 179 D. Ding, K. Li, B. Liu and B. Z. Tang, *Acc. Chem. Res.*, 2013, **46**, 2441.
- 180 M. D. Ward, *Chem. Soc. Rev.*, 1997, **26**, 365.
- 181 Y. Zeng, Z. Fu, H. Chen, C. Liu, S. Liao and J. Dai, *Chem. Commun.*, 2012, **48**, 8114.
- 182 D. Tanaka, S. Horike, S. Kitagawa, M. Ohba, M. Hasegawa, Y. Ozawa and K. Toriumi, *Chem. Commun.*, 2007, 3142, DOI: 10.1039/b707947h.



- 183 W. Zhang, L. G. Qiu, Y. P. Yuan, A. J. Xie, Y. H. Shen and J. F. Zhu, *J. Hazard. Mater.*, 2012, **221**, 147.
- 184 L.-L. Wang, C.-X. Yang and X.-P. Yan, *Sci. China: Chem.*, 2018, **61**, 1470.
- 185 Y. P. Wang, Z. Y. Zhao, G. L. Li, Y. Yan and C. Hao, *J. Mol. Model.*, 2018, **24**, 153.
- 186 Y. A. Yang, Z. Y. Zhao, Y. Yan, G. L. Li and C. Hao, *New J. Chem.*, 2019, **43**, 9274.
- 187 X. D. Song, Z. Y. Zhao, D. H. Si, X. Wang, F. Y. Zhou, M. R. Zhang, Y. T. Shi and C. Hao, *J. Mol. Model.*, 2019, **25**, 248.
- 188 Y. Yuan, H. Ren, F. Sun, X. Jing, K. Cai, X. Zhao, Y. Wang, Y. Wei and G. Zhu, *J. Phys. Chem. C*, 2012, **116**, 26431.
- 189 B. Gole, A. K. Bar and P. S. Mukherjee, *Chem. Commun.*, 2011, **47**, 12137.
- 190 G. Das, B. P. Biswal, S. Kandambeth, V. Venkatesh, G. Kaur, M. Addicoat, T. Heine, S. Verma and R. Banerjee, *Chem. Sci.*, 2015, **6**, 3931.
- 191 C. L. Zhang, S. M. Zhang, Y. H. Yan, F. Xia, A. N. Huang and Y. Z. Xian, *ACS Appl. Mater. Interfaces*, 2017, **9**, 13415.
- 192 R. Gomes and A. Bhaumik, *RSC Adv.*, 2016, **6**, 28047.
- 193 D. Kaleeswaran, P. Vishnoi and R. Murugavel, *J. Mater. Chem. C*, 2015, **3**, 10040.
- 194 P. Das and S. K. Mandal, *J. Mater. Chem. A*, 2018, **6**, 16246.
- 195 D. Ray, S. Dalapati and N. Guchhait, *Spectrochim. Acta, Part A*, 2013, **115**, 219.
- 196 P. Albacete, A. Lopez-Moreno, S. Mena-Hernando, A. E. Platero-Prats, E. M. Perez and F. Zamora, *Chem. Commun.*, 2019, **55**, 1382.
- 197 P. Vishnoi, M. G. Walawalkar, S. Sen, A. Datta, G. N. Patwari and R. Murugavel, *Phys. Chem. Chem. Phys.*, 2014, **16**, 10651.
- 198 P. Vishnoi, S. Sen, G. N. Patwari and R. Murugavel, *New J. Chem.*, 2015, **39**, 886.
- 199 P. Vishnoi, M. G. Walawalkar and R. Murugavel, *Cryst. Growth Des.*, 2014, **14**, 5668.
- 200 M. W. Zhu, S. Q. Xu, X. Z. Wang, Y. Q. Chen, L. Y. Dai and X. Zhao, *Chem. Commun.*, 2018, **54**, 2308.
- 201 Q. Gao, X. Li, G. H. Ning, K. Leng, B. B. Tian, C. B. Liu, W. Tang, H. S. Xu and K. P. Loh, *Chem. Commun.*, 2018, **54**, 2349.
- 202 M. Hu, W. Kang, B. Cheng, Z. Li, Y. Zhao and L. Li, *Microchim. Acta*, 2016, **183**, 1713.
- 203 M. Hu, W. Kang, Z. Zhong, B. Cheng and W. Xing, *Ind. Eng. Chem. Res.*, 2018, **57**, 11668.
- 204 Y.-Y. Lv, J. Wu and Z.-K. Xu, *Sens. Actuators, B*, 2010, **148**, 233.
- 205 M. H. Lee, J. S. Kim and J. L. Sessler, *Chem. Soc. Rev.*, 2015, **44**, 4185.
- 206 H. L. Qian, C. Dai, C. X. Yang and X. P. Yan, *ACS Appl. Mater. Interfaces*, 2017, **9**, 24999.
- 207 W. Liu, Y. P. Cao, W. Z. Wang, D. Y. Gong, T. Cao, J. Qian, K. Iqbal, W. W. Qin and H. C. Guo, *Chem. Commun.*, 2019, **55**, 167.
- 208 L. Jarup, *Br. Med. Bull.*, 2003, **68**, 167.
- 209 J. Huff, R. M. Lunn, M. P. Waalkes, L. Tomatis and P. F. Infante, *Int. J. Occup. Environ. Health*, 2007, **13**, 202.
- 210 P. Bhatti, P. A. Stewart, A. Hutchinson, N. Rothman, M. S. Linet, P. D. Inskip and P. Rajaraman, *Cancer Epidemiol., Biomarkers Prev.*, 2009, **18**, 1841.
- 211 M. Valko, H. Morris and M. T. Cronin, *Curr. Med. Chem.*, 2005, **12**, 1161.
- 212 A. M. El-Sharkawy, O. Sahota, R. J. Maughan and D. N. Lobo, *Clin. Nutr.*, 2014, **33**, 6.
- 213 J.-D. Xiao, L.-G. Qiu, Y.-P. Yuan, X. Jiang, A.-J. Xie and Y.-H. Shen, *Inorg. Chem. Commun.*, 2013, **29**, 128.
- 214 Y. Z. Zhu, M. Qiao, W. C. Peng, Y. Li, G. L. Zhang, F. B. Zhang, Y. F. Li and X. B. Fan, *J. Mater. Chem. A*, 2017, **5**, 9272.
- 215 Z. Zhou, W. Zhong, K. Cui, Z. Zhuang, L. Li, L. Li, J. Bi and Y. Yu, *Chem. Commun.*, 2018, **54**, 9977.
- 216 E. M. Nolan and S. J. Lippard, *J. Am. Chem. Soc.*, 2003, **125**, 14270.
- 217 S. Yoon, A. E. Albers, A. P. Wong and C. J. Chang, *J. Am. Chem. Soc.*, 2005, **127**, 16030.
- 218 Y. Zhao and Z. Zhong, *J. Am. Chem. Soc.*, 2006, **128**, 9988.
- 219 E. M. Nolan and S. J. Lippard, *Chem. Rev.*, 2008, **108**, 3443.
- 220 A. B. Descalzo, R. Martinez-Manez, R. Radeaglia, K. Rurack and J. Soto, *J. Am. Chem. Soc.*, 2003, **125**, 3418.
- 221 R. P. Schwarzenbach, B. I. Escher, K. Fenner, T. B. Hofstetter, C. A. Johnson, U. von Gunten and B. Wehrli, *Science*, 2006, **313**, 1072.
- 222 E. Jin, J. Li, K. Geng, Q. Jiang, H. Xu, Q. Xu and D. Jiang, *Nat. Commun.*, 2018, **9**, 4143.
- 223 Y. Li, F. Li, H. Zhang, Z. Xie, W. Xie, H. Xu, B. Li, F. Shen, L. Ye, M. Hanif, D. Ma and Y. Ma, *Chem. Commun.*, 2007, 231, DOI: 10.1039/b612732k.
- 224 T. Wang, R. Xue, H. Chen, P. Shi, X. Lei, Y. Wei, H. Guo and W. Yang, *New J. Chem.*, 2017, **41**, 14272.
- 225 X. C. Wu, B. W. Wang, Z. Q. Yang and L. G. Chen, *J. Mater. Chem. A*, 2019, **7**, 5650.
- 226 G. Chen, H. H. Lan, S. L. Cai, B. Sun, X. L. Li, Z. H. He, S. R. Zheng, J. Fan, Y. Liu and W. G. Zhang, *ACS Appl. Mater. Interfaces*, 2019, **11**, 12830.
- 227 A. A. Aruffo, T. B. Murphy, D. K. Johnson, N. J. Rose and V. Schomaker, *Inorg. Chim. Acta*, 1982, **67**, L25.
- 228 W.-R. Cui, C.-R. Zhang, W. Jiang, R.-P. Liang and J.-D. Qiu, *ACS Appl. Nano Mater.*, 2019, **2**, 5342.
- 229 W. R. Cui, C. R. Zhang, W. Jiang, F. F. Li, R. P. Liang, J. Liu and J. D. Qiu, *Nat. Commun.*, 2020, **11**, 436.
- 230 M. Zheng, H. Tan, Z. Xie, L. Zhang, X. Jing and Z. Sun, *ACS Appl. Mater. Interfaces*, 2013, **5**, 1078.
- 231 D. Wu, A. C. Sedgwick, T. Gunnlaugsson, E. U. Akkaya, J. Yoon and T. D. James, *Chem. Soc. Rev.*, 2017, **46**, 7105.
- 232 B. Esser and T. M. Swager, *Angew. Chem., Int. Ed.*, 2010, **49**, 8872.
- 233 Q. Sun, B. Aguila, J. Perman, N. Nguyen and S. Ma, *J. Am. Chem. Soc.*, 2016, **138**, 15790.
- 234 Y. W. Zhang, X. C. Shen, X. Feng, H. Xia, Y. Mu and X. M. Liu, *Chem. Commun.*, 2016, **52**, 11088.
- 235 C. Long, L. W. He, F. Y. Ma, L. Wei, Y. X. Wang, M. A. Silver, L. H. Chen, Z. Lin, D. X. Gui, D. W. Juan, Z. F. Chai and S. A. Wang, *ACS Appl. Mater. Interfaces*, 2018, **10**, 15364.





- 236 Q. Lin, X. Zhu, Y.-P. Fu, Y.-M. Zhang and T.-B. Wei, *Dyes Pigm.*, 2015, **112**, 280.
- 237 Z. Li, N. Huang, K. H. Lee, Y. Feng, S. Tao, Q. Jiang, Y. Nagao, S. Irle and D. Jiang, *J. Am. Chem. Soc.*, 2018, **140**, 12374.
- 238 Y. Zhou, J. F. Zhang and J. Yoon, *Chem. Rev.*, 2014, **114**, 5511.
- 239 S. Weiss, *Science*, 1999, **283**, 1676.
- 240 Y. W. Peng, Y. Huang, Y. H. Zhu, B. Chen, L. Y. Wang, Z. C. Lai, Z. C. Zhang, M. T. Zhao, C. L. Tan, N. L. Yang, F. W. Shao, Y. Han and H. Zhang, *J. Am. Chem. Soc.*, 2017, **139**, 8698.
- 241 W. Li, C. X. Yang and X. P. Yan, *Chem. Commun.*, 2017, **53**, 11469.
- 242 T. H. Ni, D. A. W. Zhang, J. Wang, S. Wang, H. L. Liu and B. G. Sun, *Sens. Actuators, B*, 2018, **269**, 340.
- 243 Y. Wang, Y. Z. Wang and H. L. Liu, *Nanomaterials*, 2019, **9**, 305.
- 244 J.-M. Wang, X. Lian and B. Yan, *Inorg. Chem.*, 2019, **58**, 9956.
- 245 D. W. Zhang, H. L. Liu, W. T. Geng and Y. P. Wang, *Food Chem.*, 2019, **277**, 639.
- 246 D. W. Zhang, Y. P. Wang, W. T. Geng and H. L. Liu, *Sens. Actuators, B*, 2019, **285**, 546.
- 247 Y. Zhang, D. W. Zhang and H. L. Liu, *Polymers*, 2019, **11**, 708.
- 248 A. Mal, R. K. Mishra, V. K. Praveen, M. A. Khayum, R. Banerjee and A. Ajayaghosh, *Angew. Chem., Int. Ed.*, 2018, **57**, 8443.
- 249 J. Q. Dong, X. Li, S. B. Peh, Y. D. Yuan, Y. X. Wang, D. X. Ji, S. J. Peng, G. L. Liu, S. M. Ying, D. Q. Yuan, J. W. Jiang, S. Ramakrishna and D. Zhao, *Chem. Mater.*, 2019, **31**, 146.
- 250 X. Wu, X. Han, Q. Xu, Y. Liu, C. Yuan, S. Yang, Y. Liu, J. Jiang and Y. Cui, *J. Am. Chem. Soc.*, 2019, **141**, 7081.
- 251 P. Wang, F. Zhou, C. Zhang, S. Y. Yin, L. L. Teng, L. L. Chen, X. X. Hu, H. W. Liu, X. Yin and X. B. Zhang, *Chem. Sci.*, 2018, **9**, 8402.
- 252 E. Verheyen, J. P. Schillemans, M. van Wijk, M. A. Demeniex, W. E. Hennink and C. F. van Nostrum, *Biomaterials*, 2011, **32**, 3008.
- 253 J. E. Lofgreen, I. L. Moudrakovski and G. A. Ozin, *ACS Nano*, 2011, **5**, 2277.
- 254 L. Friedman and J. G. Miller, *Science*, 1971, **172**, 1044.
- 255 X. Han, J. Huang, C. Yuan, Y. Liu and Y. Cui, *J. Am. Chem. Soc.*, 2018, **140**, 892.
- 256 J. Gershenzon and N. Dudareva, *Nat. Chem. Biol.*, 2007, **3**, 408.
- 257 L. J. O'Connor, I. N. Mistry, S. L. Collins, L. K. Folkes, G. Brown, S. J. Conway and E. M. Hammond, *ACS Cent. Sci.*, 2017, **3**, 20.
- 258 B. J. Smith, L. R. Parent, A. C. Overholts, P. A. Beaucage, R. P. Bisbey, A. D. Chavez, N. Hwang, C. Park, A. M. Evans, N. C. Gianneschi and W. R. Dichtel, *ACS Cent. Sci.*, 2017, **3**, 58.
- 259 A. Akthakul, N. Maklakov and J. White, *Anal. Chem.*, 2010, **82**, 6487.
- 260 Y. Wang, J. T. Chen and X. P. Yan, *Anal. Chem.*, 2013, **85**, 2529.
- 261 D. Kaleeswaran and R. Murugavel, *J. Chem. Sci.*, 2018, **130**, 1.
- 262 M. R. Rao, Y. Fang, S. De Feyter and D. F. Perepichka, *J. Am. Chem. Soc.*, 2017, **139**, 2421.
- 263 Y. Y. Cai, Y. Jiang, L. P. Feng, Y. Hua, H. Liu, C. Fan, M. Y. Yin, S. Li, X. X. Lv and H. Wang, *Anal. Chim. Acta*, 2019, **1057**, 88.
- 264 Y. Li, M. Zhang, X. Guo, R. Wen, X. Li, X. Li, S. Li and L. Ma, *Nanoscale Horiz.*, 2018, **3**, 205.
- 265 H. L. Liu, Y. Zhang, D. W. Zhang, F. P. Zheng, M. Q. Huang, J. Y. Sun, X. T. Sun, H. H. Li, J. Wang and B. G. Sun, *Microchim. Acta*, 2019, **186**, 182.
- 266 U. Guth, W. Vonau and J. Zosel, *Meas. Sci. Technol.*, 2009, **20**, 042002.
- 267 E. Barsoukov and J. R. Macdonald, *Impedance Spectroscopy: Theory, Experiment, and Applications*, Wiley, 2018.
- 268 M. E. Orazem and B. Tribollet, *Electrochemical Impedance Spectroscopy*, Wiley, 2017.
- 269 A. Lasia, *Electrochemical Impedance Spectroscopy and its Applications*, Springer, New York, 2014.
- 270 D. Antuña-Jiménez, G. Díaz-Díaz, M. C. Blanco-López, M. J. Lobo-Castañón, A. J. Miranda-Ordieres and P. Tuñón-Blanco, *Molecularly Imprinted Sensors*, 2012, pp. 1–34, DOI: 10.1016/b978-0-444-56331-6.00001-3.
- 271 G. Shen, P.-C. Chen, K. Ryu and C. Zhou, *J. Mater. Chem.*, 2009, **19**, 828.
- 272 P. Y. Wang, M. M. Kang, S. M. Sun, Q. Liu, Z. H. Zhang and S. M. Fang, *Chin. J. Chem.*, 2014, **32**, 838.
- 273 H. Singh, V. K. Tomer, N. Jena, I. Bala, N. Sharma, D. Nepak, A. De Sarkar, K. Kailasam and S. K. Pal, *J. Mater. Chem. A*, 2017, **5**, 21820.
- 274 T. Z. Liu, J. R. Xia, Y. Li, W. K. Chen, S. Zhang, Y. Liu, L. Zheng and Y. H. Yang, *Chem. J. Chin. Univ.*, 2015, **36**, 1880.
- 275 Z. Cao, F. Duan, X. Huang, Y. Liu, N. Zhou, L. Xia, Z. Zhang and M. Du, *Anal. Chim. Acta*, 2019, **1082**, 176.
- 276 Y. Ma, M. Lu, Y. Deng, R. Bai, X. Zhang, D. Li, K. Zhang, R. Hu and Y. Yang, *J. Biomed. Nanotechnol.*, 2018, **14**, 1169.
- 277 T. Zhang, N. Ma, A. Ali, Q. Wei, D. Wu and X. Ren, *Biosens. Bioelectron.*, 2018, **119**, 176.
- 278 X. Yan, Y. P. Song, J. M. Liu, N. Zhou, C. L. Zhang, L. H. He, Z. H. Zhang and Z. Y. Liu, *Biosens. Bioelectron.*, 2019, **126**, 734.
- 279 X. K. Liu, M. Y. Hu, M. H. Wang, Y. P. Song, N. Zhou, L. H. He and Z. H. Zhang, *Biosens. Bioelectron.*, 2019, **123**, 59.
- 280 M. H. Wang, M. Y. Hu, J. M. Liu, C. P. Guo, D. L. Peng, Q. J. Jia, L. H. He, Z. H. Zhang and M. Du, *Biosens. Bioelectron.*, 2019, **132**, 8.
- 281 T. Zhang, Y. L. Chen, W. Huang, Y. Wang and X. Y. Hu, *Sens. Actuators, B*, 2018, **276**, 362.
- 282 Y. F. Sun, L. H. Xu, G. I. N. Waterhouse, M. L. Wang, X. G. Qiao and Z. X. Xu, *Sens. Actuators, B*, 2019, **281**, 107.
- 283 M. Xu, L. Wang, Y. Xie, Y. Song and L. Wang, *Sens. Actuators, B*, 2019, **281**, 1009.



- 284 Y. Deng, X. T. Du, Y. C. Ma, K. L. Zhang, X. Zhang, D. L. Li, R. Y. Bai, R. Hu and Y. H. Yang, *Nanosci. Nanotechnol. Lett.*, 2018, **10**, 520.
- 285 X. Zhang, K. N. Chi, D. L. Li, Y. Deng, Y. C. Ma, Q. Q. Xu, R. Hu and Y. H. Yang, *Biosens. Bioelectron.*, 2019, **129**, 64.
- 286 N. Zhou, Y. S. Ma, B. Hu, L. H. He, S. J. Wang, Z. H. Zhang and S. Y. Lu, *Biosens. Bioelectron.*, 2019, **127**, 92.
- 287 R. Y. Wang, W. H. Ji, L. Q. Huang, L. P. Guo and X. Wang, *Anal. Lett.*, 2019, **52**, 1757.
- 288 Y. Yue, P. Cai, X. Xu, H. Li, H. Chen, H. C. Zhou and N. Huang, *Angew. Chem., Int. Ed.*, 2021, **60**, 10806.
- 289 A. A. Ansari, A. Kaushik, P. R. Solanki and B. D. Malhotra, *Bioelectrochemistry*, 2010, **77**, 75.
- 290 Z. Zhang, S. Liu, Y. Shi, Y. Zhang, D. Peacock, F. Yan, P. Wang, L. He, X. Feng and S. Fang, *J. Mater. Chem. B*, 2014, **2**, 1530.
- 291 L. Bai, S. Z. Phua, W. Q. Lim, A. Jana, Z. Luo, H. P. Tham, L. Zhao, Q. Gao and Y. Zhao, *Chem. Commun.*, 2016, **52**, 4128.
- 292 X. Wu, X. Han, Y. Liu, Y. Liu and Y. Cui, *J. Am. Chem. Soc.*, 2018, **140**, 16124.
- 293 Y. Suzuki, M. Endo and H. Sugiyama, *Nat. Commun.*, 2015, **6**, 8052.
- 294 J. Teixeira, A. Gaspar, E. M. Garrido, J. Garrido and F. Borges, *BioMed Res. Int.*, 2013, **2013**, 251754.
- 295 T. W. Crozier, A. Stalmach, M. E. Lean and A. Crozier, *Food Funct.*, 2012, **3**, 30.
- 296 P. Wang, Q. Wu, L. Han, S. Wang, S. Fang, Z. Zhang and S. Sun, *RSC Adv.*, 2015, **5**, 27290.
- 297 F. Xu, S. Jin, H. Zhong, D. Wu, X. Yang, X. Chen, H. Wei, R. Fu and D. Jiang, *Sci. Rep.*, 2015, **5**, 8225.
- 298 B. Sun, J. Liu, A. Cao, W. Song and D. Wang, *Chem. Commun.*, 2017, **53**, 6303.
- 299 T. Zhang, C. W. Gao, W. Huang, Y. L. Chen, Y. Wang and J. M. Wang, *Talanta*, 2018, **188**, 578.
- 300 N. Agmon, *Chem. Phys. Lett.*, 1995, **244**, 456.
- 301 C. R. DeBlase, K. E. Silberstein, T. T. Truong, H. D. Abruna and W. R. Dichtel, *J. Am. Chem. Soc.*, 2013, **135**, 16821.
- 302 C. R. DeBlase, K. Hernandez-Burgos, K. E. Silberstein, G. G. Rodriguez-Calero, R. P. Bisbey, H. D. Abruna and W. R. Dichtel, *ACS Nano*, 2015, **9**, 3178.
- 303 D.-H. Yang, Z.-Q. Yao, D. Wu, Y.-H. Zhang, Z. Zhou and X.-H. Bu, *J. Mater. Chem. A*, 2016, **4**, 18621.
- 304 S. Chandra, D. Roy Chowdhury, M. Addicoat, T. Heine, A. Paul and R. Banerjee, *Chem. Mater.*, 2017, **29**, 2074.
- 305 Y. Zhang, S. N. Riduan and J. Wang, *Chem. – Eur. J.*, 2017, **23**, 16419.
- 306 E. Vitaku, C. N. Gannett, K. L. Carpenter, L. Shen, H. D. Abruna and W. R. Dichtel, *J. Am. Chem. Soc.*, 2020, **142**, 16.
- 307 H. Ding, Y. Li, H. Hu, Y. Sun, J. Wang, C. Wang, C. Wang, G. Zhang, B. Wang, W. Xu and D. Zhang, *Chem. – Eur. J.*, 2014, **20**, 14614.
- 308 E. Jin, M. Asada, Q. Xu, S. Dalapati, M. A. Addicoat, M. A. Brady, H. Xu, T. Nakamura, T. Heine, Q. Chen and D. Jiang, *Science*, 2017, **357**, 673.
- 309 S. Kim and H. C. Choi, *Commun. Chem.*, 2019, **2**, 60.
- 310 M. Wang, M. Ballabio, M. Wang, H. H. Lin, B. P. Biswal, X. Han, S. Paasch, E. Brunner, P. Liu, M. Chen, M. Bonn, T. Heine, S. Zhou, E. Canovas, R. Dong and X. Feng, *J. Am. Chem. Soc.*, 2019, **141**, 16810.
- 311 H. Yang, S. Zhang, L. Han, Z. Zhang, Z. Xue, J. Gao, Y. Li, C. Huang, Y. Yi, H. Liu and Y. Li, *ACS Appl. Mater. Interfaces*, 2016, **8**, 5366.
- 312 T. M. Swager, *Macromolecules*, 2017, **50**, 4867.
- 313 M. Kertesz, C. H. Choi and S. Yang, *Chem. Rev.*, 2005, **105**, 3448.
- 314 J. Ferraris, D. O. Cowan, V. Walatka and J. H. Perlstein, *J. Am. Chem. Soc.*, 1973, **95**, 948.
- 315 J. L. Petersen, C. S. Schramm, D. R. Stojakovic, B. M. Hoffman and T. J. Marks, *J. Am. Chem. Soc.*, 1977, **99**, 286.
- 316 N. S. Hush, *Ann. N. Y. Acad. Sci.*, 2003, **1006**, 1.
- 317 L. Sun, M. G. Campbell and M. Dincă, *Angew. Chem., Int. Ed.*, 2016, **55**, 3566.
- 318 G. Givaja, P. Amo-Ochoa, C. J. Gomez-Garcia and F. Zamora, *Chem. Soc. Rev.*, 2012, **41**, 115.
- 319 M. Ko, L. Mendecki and K. A. Mirica, *Chem. Commun.*, 2018, **54**, 7873.
- 320 S.-L. Cai, Y.-B. Zhang, A. B. Pun, B. He, J. Yang, F. M. Toma, I. D. Sharp, O. M. Yaghi, J. Fan, S.-R. Zheng, W.-G. Zhang and Y. Liu, *Chem. Sci.*, 2014, **5**, 4693.
- 321 L. Chen, K. Furukawa, J. Gao, A. Nagai, T. Nakamura, Y. Dong and D. Jiang, *J. Am. Chem. Soc.*, 2014, **136**, 9806.
- 322 V. Lakshmi, C. H. Liu, M. Rajeswara Rao, Y. Chen, Y. Fang, A. Dadvand, E. Hamzehpoor, Y. Sakai-Otsuka, R. S. Stein and D. F. Perepichka, *J. Am. Chem. Soc.*, 2020, **142**, 2155.
- 323 L. Wang, C. Zeng, H. Xu, P. Yin, D. Chen, J. Deng, M. Li, N. Zheng, C. Gu and Y. Ma, *Chem. Sci.*, 2019, **10**, 1023.
- 324 C. Zhu, G. Yang, H. Li, D. Du and Y. Lin, *Anal. Chem.*, 2015, **87**, 230.
- 325 J. Yoo, S. J. Cho, G. Y. Jung, S. H. Kim, K. H. Choi, J. H. Kim, C. K. Lee, S. K. Kwak and S. Y. Lee, *Nano Lett.*, 2016, **16**, 3292.
- 326 Y. Guo, K. Ruan, X. Yang, T. Ma, J. Kong, N. Wu, J. Zhang, J. Gu and Z. Guo, *J. Mater. Chem. C*, 2019, **7**, 7035.
- 327 Y. Gu, J. P. Wang, H. P. Shi, M. F. Pan, B. Liu, G. Z. Fang and S. Wang, *Biosens. Bioelectron.*, 2019, **128**, 129.
- 328 D. DeVault, *J. Am. Chem. Soc.*, 1943, **65**, 532.
- 329 O. Coskun, *North. Clin. Istanbul.*, 2016, **3**, 156.
- 330 S. Mitra, *Sample Preparation Techniques in Analytical Chemistry*, John Wiley & Sons, Inc., 2003.
- 331 M.-C. Hennion, *J. Chromatogr. A*, 1999, **856**, 3.
- 332 A. Chisvert, S. Cárdenas and R. Lucena, *Trends Anal. Chem.*, 2019, **112**, 226.
- 333 M. Šafaříková and I. Šafařík, *J. Magn. Magn. Mater.*, 1999, **194**, 108.
- 334 C. L. Arthur and J. Pawliszyn, *Anal. Chem.*, 2002, **62**, 2145.
- 335 I. Vasconcelos and C. Fernandes, *Trends Anal. Chem.*, 2017, **89**, 41.



- 336 C.-H. Xu, G.-S. Chen, Z.-H. Xiong, Y.-X. Fan, X.-C. Wang and Y. Liu, *Trends Anal. Chem.*, 2016, **80**, 12.
- 337 F. Augusto, L. W. Hantao, N. G. S. Mogollón and S. C. G. N. Braga, *Trends Anal. Chem.*, 2013, **43**, 14.
- 338 C. W. Huck and G. K. Bonn, *J. Chromatogr. A*, 2000, **885**, 51.
- 339 M. Polo, M. Llompart, C. Garcia-Jares and R. Cela, *J. Chromatogr. A*, 2005, **1072**, 63.
- 340 T. Nema, E. C. Chan and P. C. Ho, *Talanta*, 2010, **82**, 488.
- 341 H. Yu, T. D. Ho and J. L. Anderson, *Trends Anal. Chem.*, 2013, **45**, 219.
- 342 M. M. Sanagi, S. Salleh, W. A. W. Ibrahim, A. A. Naim, D. Hermawan, M. Miskam, I. Hussain and H. Y. Aboul-Enein, *J. Food Compos. Anal.*, 2013, **32**, 155.
- 343 L. M. Ravelo-Perez, A. V. Herrera-Herrera, J. Hernandez-Borges and M. A. Rodriguez-Delgado, *J. Chromatogr. A*, 2010, **1217**, 2618.
- 344 C. Herrero-Latorre, J. Barciela-Garcia, S. Garcia-Martin and R. M. Pena-Crecente, *Anal. Chim. Acta*, 2018, **1002**, 1.
- 345 M. E. I. Badawy, M. A. M. El-Nouby and A. E. M. Marei, *Int. J. Anal. Chem.*, 2018, **2018**, 3640691.
- 346 J. Ma, Z. Yao, L. Hou, W. Lu, Q. Yang, J. Li and L. Chen, *Talanta*, 2016, **161**, 686.
- 347 F. Maya, C. Palomino Cabello, R. M. Frizzarin, J. M. Estela, G. Turnes Palomino and V. Cerdà, *Trends Anal. Chem.*, 2017, **90**, 142.
- 348 A. I. Cooper, *Adv. Mater.*, 2009, **21**, 1291.
- 349 S. Xu, Y. Luo and B. Tan, *Macromol. Rapid Commun.*, 2013, **34**, 471.
- 350 Z. Wang, S. Zhang, Y. Chen, Z. Zhang and S. Ma, *Chem. Soc. Rev.*, 2020, **49**, 708.
- 351 C. J. Zhang, G. K. Li and Z. M. Zhang, *J. Chromatogr. A*, 2015, **1419**, 1.
- 352 H. Q. Wang, Z. Li, W. Feng and Q. Jia, *New J. Chem.*, 2017, **41**, 13043.
- 353 R. Wang and Z. L. Chen, *Microchim. Acta*, 2017, **184**, 3867.
- 354 Z. J. Yan, M. He, B. B. Chen, B. Gui, C. Wang and B. Hu, *J. Chromatogr. A*, 2017, **1525**, 32.
- 355 S. H. Zhang, Q. Yang, Z. Li, W. C. Wang, C. Wang and Z. Wang, *Anal. Bioanal. Chem.*, 2017, **409**, 3429.
- 356 L. Chen, Y. T. He, Z. X. Lei, C. L. Gao, Q. Xie, P. Tong and Z. Lin, *Talanta*, 2018, **181**, 296.
- 357 D. D. Jiang, T. T. Hu, H. J. Zheng, G. X. Xu and Q. Jia, *Chem. – Eur. J.*, 2018, **24**, 10390.
- 358 N. Li, D. Wu, N. Hu, G. S. Fan, X. T. Li, J. Sun, X. F. Chen, Y. R. Suo, G. L. Li and Y. N. Wu, *J. Agric. Food Chem.*, 2018, **66**, 3572.
- 359 N. Li, D. Wu, J. C. Liu, N. Hu, X. X. Shi, C. J. Dai, Z. W. Sun, Y. R. Suo, G. L. Li and Y. N. Wu, *Microchem. J.*, 2018, **143**, 350.
- 360 J. Q. Ma, J. Y. Ren, L. L. Wang, X. Wang, J. M. Lin and R. S. Zhao, *J. Sep. Sci.*, 2018, **41**, 3724.
- 361 J. Y. Ren, X. L. Wang, X. L. Li, M. L. Wang, R. S. Zhao and J. M. Lin, *Anal. Bioanal. Chem.*, 2018, **410**, 1657.
- 362 A. Shahvar, R. Soltani, M. Saraji, M. Dinari and S. Alijani, *J. Chromatogr. A*, 2018, **1565**, 48.
- 363 X. X. Shi, N. Li, D. Wu, N. Hu, J. Sun, X. X. Zhou, Y. R. Suo, G. L. Li and Y. N. Wu, *Anal. Methods*, 2018, **10**, 5014.
- 364 Q. Q. Wang, H. H. Wu, F. Y. Lv, Y. T. Cao, Y. Zhou and N. Gan, *J. Chromatogr. A*, 2018, **1572**, 1.
- 365 L. Xia, X. M. Chen, X. H. Xiao and G. K. Li, *J. Sep. Sci.*, 2018, **41**, 3733.
- 366 Z. H. Deng, X. Wang, X. L. Wang, C. L. Gao, L. Dong, M. L. Wang and R. S. Zhao, *Microchim. Acta*, 2019, **186**, 108.
- 367 W. Gao, Y. Tian, H. Liu, Y. Q. Cai, A. F. Liu, Y. L. Yu, Z. S. Zhao and G. B. Jiang, *Anal. Chem.*, 2019, **91**, 772.
- 368 K. Hu, Y. X. Lv, F. G. Ye, T. Chen and S. L. Zhao, *Anal. Chem.*, 2019, **91**, 6353.
- 369 L. Liu, W. K. Meng, L. Li, G. J. Xu, X. Wang, L. Z. Chen, M. L. Wang, J. M. Lin and R. S. Zhao, *Chem. Eng. J.*, 2019, **369**, 920.
- 370 L. Liu, W. K. Meng, Y. S. Zhou, X. Wang, G. J. Xu, M. L. Wang, J. M. Lin and R. S. Zhao, *Chem. Eng. J.*, 2019, **356**, 926.
- 371 Y. J. Lu, B. C. Wang, C. L. Wang, Y. H. Yan, D. P. Wu, H. Z. Liang and K. Q. Tang, *Chromatographia*, 2019, **82**, 1089.
- 372 T. T. Ma, X. F. Shen, C. Yang, H. L. Qian, Y. H. Pang and X. P. Yan, *Talanta*, 2019, **201**, 413.
- 373 S. H. Wang, H. Y. Niu, D. Cao and Y. Q. Cai, *Talanta*, 2019, **194**, 522.
- 374 F. F. Wu, Q. Y. Chen, X. J. Ma, T. T. Li, L. F. Wang, J. Hong, Y. H. Sheng, M. L. Ye and Y. Zhu, *Anal. Methods*, 2019, **11**, 3381.
- 375 Y. H. Yan, Y. J. Lu, B. C. Wang, Y. Q. Gao, L. L. Zhao, H. Z. Liang and D. P. Wu, *ACS Appl. Mater. Interfaces*, 2018, **10**, 26539.
- 376 T. Wu, X. H. Zang, M. T. Wang, Q. Y. Chang, C. Wang, Q. H. Wu and Z. Wang, *J. Agric. Food Chem.*, 2018, **66**, 11158.
- 377 M. X. Wu, G. Chen, P. Liu, W. H. Zhou and Q. Jia, *J. Chromatogr. A*, 2016, **1456**, 34.
- 378 W. H. Ji, R. H. Sun, Y. L. Geng, W. Liu and X. Wang, *Anal. Chim. Acta*, 2018, **1001**, 179.
- 379 Y. H. Song, R. Y. Ma, L. Hao, X. M. Yang, C. Wang, Q. H. Wu and Z. Wang, *J. Chromatogr. A*, 2018, **1572**, 20.
- 380 M. Wang, X. Zhou, X. Zang, Y. Pang, Q. Chang, C. Wang and Z. Wang, *J. Sep. Sci.*, 2018, **41**, 4038.
- 381 X. L. Wang, R. Y. Ma, L. Hao, Q. H. Wu, C. Wang and Z. Wang, *J. Chromatogr. A*, 2018, **1551**, 1.
- 382 R. Y. Liang, Y. Peng, Y. L. Hu and G. K. Li, *J. Sep. Sci.*, 2019, **42**, 1432.
- 383 J. M. Liu, X. Z. Wang, C. Y. Zhao, J. L. Hao, G. Z. Fang and S. Wang, *J. Hazard. Mater.*, 2018, **344**, 220.
- 384 Y. L. Chen and Z. L. Chen, *Talanta*, 2017, **165**, 188.
- 385 H. P. Wang, F. L. Jiao, F. Y. Gao, Y. Y. Lv, Q. Wu, Y. Zhao, Y. H. Shen, Y. J. Zhang and X. H. Qian, *Talanta*, 2017, **166**, 133.





- 386 X. M. Wang, G. J. Xu, X. L. Wang, X. Wang, M. L. Wang, R. S. Zhao and J. M. Lin, *Chin. J. Anal. Chem.*, 2018, **46**, 1990.
- 387 C. H. Gao, J. Bai, Y. T. He, Q. Zheng, W. D. Ma, Z. X. Lei, M. Y. Zhang, J. Wu, F. F. Fu and Z. Lin, *ACS Appl. Mater. Interfaces*, 2019, **11**, 13735.
- 388 W. X. Li, N. Chen, Y. Zhu, D. Shou, M. Y. Zhi and X. Q. Zeng, *Microchim. Acta*, 2019, **186**, 76.
- 389 J. M. Liu, S. W. Lv, X. Y. Yuan, H. L. Liu and S. Wang, *RSC Adv.*, 2019, **9**, 14247.
- 390 Z. M. Yan, B. Q. Hu, Q. L. Li, S. X. Zhang, J. Pang and C. H. Wu, *J. Chromatogr. A*, 2019, **1584**, 33.
- 391 J. X. Wang, J. Li, M. X. Gao and X. M. Zhang, *Nanoscale*, 2017, **9**, 10750.
- 392 R. Zhai, X. Gong, J. Xie, Y. Yuan, F. Xu, Y. Jiang, Z. Huang, X. Dai, Y. Zhang, X. Qian and X. Fang, *Talanta*, 2019, **191**, 553.
- 393 J. Li, L. Yang, S. Luo, B. Chen, J. Li, H. Lin, Q. Cai and S. Yao, *Anal. Chem.*, 2010, **82**, 7357.
- 394 X. Wang, S. L. Morris-Natschke and K. H. Lee, *Med. Res. Rev.*, 2007, **27**, 133.
- 395 C. R. Pearson, *Anthropogenic Compounds*, 1982, ch. 4, pp. 89–116, DOI: 10.1007/978-3-540-47028-1\_4.
- 396 P. Liljelind, G. Soderstrom, B. Hedman, S. Karlsson, L. Lundin and S. Marklund, *Environ. Sci. Technol.*, 2003, **37**, 3680.
- 397 P. Perego, L. Gatti and G. L. Beretta, *Nat. Rev. Cancer*, 2010, **10**, 523.
- 398 K. Ohtsubo and J. D. Marth, *Cell*, 2006, **126**, 855.
- 399 N. Li, J. Du, D. Wu, J. Liu, N. Li, Z. Sun, G. Li and Y. Wu, *Trends Anal. Chem.*, 2018, **108**, 154.
- 400 J. Wang, J. Li, M. Gao and X. Zhang, *Trends Anal. Chem.*, 2018, **108**, 98.
- 401 S. Zhang, Q. Yang, C. Wang, X. Luo, J. Kim, Z. Wang and Y. Yamauchi, *Adv. Sci.*, 2018, **5**, 1801116.
- 402 L. X. Chen, Q. Wu, J. Gao, H. Li, S. Q. Dong, X. F. Shi and L. Zhao, *Trends Anal. Chem.*, 2019, **113**, 182.
- 403 X. Xu, H. Li, D. Hasan, R. S. Ruoff, A. X. Wang and D. L. Fan, *Adv. Funct. Mater.*, 2013, **23**, 4332.
- 404 E. J. Blackie, E. C. Le Ru and P. G. Etchegoin, *J. Am. Chem. Soc.*, 2009, **131**, 14466.
- 405 E. C. Le, Ru, E. Blackie, M. Meyer and P. G. Etchegoin, *J. Phys. Chem. C*, 2007, **111**, 13794.
- 406 S. Schlucker, *Angew. Chem., Int. Ed.*, 2014, **53**, 4756.
- 407 Y. Yuan, N. Panwar, S. H. K. Yap, Q. Wu, S. Zeng, J. Xu, S. C. Tjin, J. Song, J. Qu and K.-T. Yong, *Coord. Chem. Rev.*, 2017, **337**, 1.
- 408 J. He, F. J. Xu, Z. Chen, X. D. Hou, Q. Liu and Z. Long, *Chem. Commun.*, 2017, **53**, 11044.
- 409 A. Sangsuwan, B. Narupai, P. Sae-ung, S. Rodtarnai, N. Rodthongkum and V. P. Hoven, *Anal. Chem.*, 2015, **87**, 10738.
- 410 Z. Guo, Q. Zhang, H. Zou, B. Guo and J. Ni, *Anal. Chem.*, 2002, **74**, 1637.
- 411 X. Li, J. Tan, J. Yu, J. Feng, A. Pan, S. Zheng and J. Wu, *Anal. Chim. Acta*, 2014, **849**, 27.
- 412 A. Nordstrom, J. V. Apon, W. Uritboonthai, E. P. Go and G. Siuzdak, *Anal. Chem.*, 2006, **78**, 272.
- 413 C. Lopez de Laorden, A. Belouqui, L. Yate, J. Calvo, M. Puigvila, J. Llop and N. C. Reichardt, *Anal. Chem.*, 2015, **87**, 431.
- 414 M. Lu, Y. Lai, G. Chen and Z. Cai, *Anal. Chem.*, 2011, **83**, 3161.
- 415 D. Feng and Y. Xia, *Anal. Chim. Acta*, 2018, **1014**, 58.
- 416 B. P. Biswal, S. Chandra, S. Kandambeth, B. Lukose, T. Heine and R. Banerjee, *J. Am. Chem. Soc.*, 2013, **135**, 5328.
- 417 Z. H. He, S. D. Gong, S. L. Cai, Y. L. Yan, G. Chen, X. L. Li, S. R. Zheng, J. Fan and W. G. Zhang, *Cryst. Growth Des.*, 2019, **19**, 3543.
- 418 G. Sauerbrey, *Z. Phys.*, 1959, **155**, 206.
- 419 S. K. Vashist and P. Vashist, *J. Sens.*, 2011, **2011**, 1.
- 420 F. Feng, J. Zheng, P. Qin, T. Han and D. Zhao, *Talanta*, 2017, **167**, 94.
- 421 Y. Gu, Y. N. Wang, X. M. Wu, M. F. Pan, N. Hu, J. P. Wang and S. Wang, *Sens. Actuators, B*, 2019, **291**, 293.
- 422 S. Zhang, Q. Yang, X. Xu, X. Liu, Q. Li, J. Guo, N. L. Torad, S. M. Alshehri, T. Ahamad, M. S. A. Hossain, Y. V. Kaneti and Y. Yamauchi, *Nanoscale*, 2020, **12**, 15611.
- 423 L.-M. Yang, E. Ganz, S. Wang, X.-J. Li and T. Frauenheim, *J. Mater. Chem. C*, 2015, **3**, 2244.
- 424 M. Hussain, X. Song, S. Shah and C. Hao, *Spectrochim. Acta, Part A*, 2019, **224**, 117432.
- 425 X. Lian, Y. Fang, E. Joseph, Q. Wang, J. Li, S. Banerjee, C. Lollar, X. Wang and H. C. Zhou, *Chem. Soc. Rev.*, 2017, **46**, 3386.
- 426 Y. Pan, H. Li, J. Farmakes, F. Xiao, B. Chen, S. Ma and Z. Yang, *J. Am. Chem. Soc.*, 2018, **140**, 16032.
- 427 M. Dogru, A. Sonnauer, A. Gavryushin, P. Knochel and T. Bein, *Chem. Commun.*, 2011, **47**, 1707.
- 428 L. M. Lanni, R. W. Tilford, M. Bharathy and J. J. Lavigne, *J. Am. Chem. Soc.*, 2011, **133**, 13975.
- 429 Q. Fang, Z. Zhuang, S. Gu, R. B. Kaspar, J. Zheng, J. Wang, S. Qiu and Y. Yan, *Nat. Commun.*, 2014, **5**, 4503.
- 430 H. Yang, Y. Du, S. Wan, G. D. Trahan, Y. Jin and W. Zhang, *Chem. Sci.*, 2015, **6**, 4049.
- 431 S. Kandambeth, V. Venkatesh, D. B. Shinde, S. Kumari, A. Halder, S. Verma and R. Banerjee, *Nat. Commun.*, 2015, **6**, 6786.
- 432 Q. Sun, C. W. Fu, B. Aguila, J. Perman, S. Wang, H. Y. Huang, F. S. Xiao and S. Ma, *J. Am. Chem. Soc.*, 2018, **140**, 984.
- 433 Q. Sun, B. Aguila, P. C. Lan and S. Ma, *Adv. Mater.*, 2019, **31**, e1900008.
- 434 S. Jin, K. Furukawa, M. Addicoat, L. Chen, S. Takahashi, S. Irle, T. Nakamura and D. Jiang, *Chem. Sci.*, 2013, **4**, 4505.
- 435 M. S. Yao, X. J. Lv, Z. H. Fu, W. H. Li, W. H. Deng, G. D. Wu and G. Xu, *Angew. Chem., Int. Ed.*, 2017, **56**, 16510.
- 436 J. Wu, J. Chen, C. Wang, Y. Zhou, K. Ba, H. Xu, W. Bao, X. Xu, A. Carlsson, S. Lazar, A. Meingast, Z. Sun and H. Deng, *Adv. Sci.*, 2020, **7**, 1903003.
- 437 J. F. Olorunyomi, S. T. Geh, R. A. Caruso and C. M. Doherty, *Mater. Horizons*, 2021, **8**, 2387.



- 438 K. Liu, H. Qi, R. Dong, R. Shivhare, M. Addicoat, T. Zhang, H. Sahabudeen, T. Heine, S. Mannsfeld, U. Kaiser, Z. Zheng and X. Feng, *Nat. Chem.*, 2019, **11**, 994.
- 439 W. Liu, X. Li, C. Wang, H. Pan, W. Liu, K. Wang, Q. Zeng, R. Wang and J. Jiang, *J. Am. Chem. Soc.*, 2019, **141**, 17431.
- 440 Q. Sun, B. Aguila, J. A. Perman, T. Butts, F.-S. Xiao and S. Ma, *Chem*, 2018, **4**, 1726.
- 441 M. Zhang, L. Li, Q. Lin, M. Tang, Y. Wu and C. Ke, *J. Am. Chem. Soc.*, 2019, **141**, 5154.
- 442 T. Zhang, H. Qi, Z. Liao, Y. D. Horev, L. A. Panes-Ruiz, P. S. Petkov, Z. Zhang, R. Shivhare, P. Zhang, K. Liu, V. Bezugly, S. Liu, Z. Zheng, S. Mannsfeld, T. Heine, G. Cuniberti, H. Haick, E. Zschech, U. Kaiser, R. Dong and X. Feng, *Nat. Commun.*, 2019, **10**, 4225.
- 443 E. Tylanakis, E. Klontzas and G. E. Froudakis, *Nanoscale*, 2011, **3**, 856.
- 444 M. Tong, Y. Lan, Z. Qin and C. Zhong, *J. Phys. Chem. C*, 2018, **122**, 13009.

